National Library of Canada
Bibliothèque nationale du Canada

Canadian Theses Service
Service des thèses canadiennes

Ottawa, Canada
K1A 0N4

## NOTICE

The quality of this microform is heavily dependent upon the quality of the original thesis submitted for microfilming. Every effort has been made to ensure the highest quality of reproduction possible.

If pages are missing, contact the university which granted the degree.

Some pages may have indistinct print, especially if the original pages were typed with a poor typewriter ribbon or if the university sent us an inferior photocopy.

Reproduction in full or in part of this microform is governed by the Canadian Copyright Act, R.S.C. 1970, c. C-30, and subsequent amendments.

## AVIS

La qualité de cette microforme dépend grandement de la qualité de la thèse soumise au microfilmage. Nous avons tout fait pour assurer une qualité supérieure de reproduction.

S'il manque des pages, veuillez communiquer avec l'université qui a conféré le grade.

La qualité d'impression de certaines pages peut laisser à désirer, surtout si les pages originales ont été dactylographiées à l'aide d'un ruban usé ou si l'université nous a fait parvenir une photocopie de qualité inférieure.

La reproduction, même partielle, de cette microforme est soumise à la Loi canadienne sur le droit d'auteur, SRC 1970, c. C-30, et ses amendements subséquents.

NL-339 (r. 88/04) c

Canada

UNIVERSITY OF ALBERTA

# $\vec{p}p \rightarrow d\pi^+$ Analyzing Powers near Threshold

BY

Jin Li

A thesis

submitted to the Faculty of Graduate Studies and Research in partial fulfillment of the requirements for the degree of Master of Science

in

Nuclear Physics

Department of Physics

Edmonton, Alberta

Fall, 1990

National Library of Canada
Bibliothèque nationale du Canada

Canadian Theses Service
Service des thèses canadiennes

Ottawa, Canada
K1A 0N4

The author has granted an irrevocable non-exclusive licence allowing the National Library of Canada to reproduce, loan, distribute or sell copies of his/her thesis by any means and in any form or format, making this thesis available to interested persons.

L'auteur a accordé une licence irrévocable et non exclusive permettant à la Bibliothèque nationale du Canada de reproduire, prêter, distribuer ou vendre des copies de sa thèse de quelque manière et sous quelque forme que ce soit pour mettre des exemplaires de cette thèse à la disposition des personnes intéressées.

The author retains ownership of the copyright in his/her thesis. Neither the thesis nor substantial extracts from it may be printed or otherwise reproduced without his/her permission.

L'auteur conserve la propriété du droit d'auteur qui protège sa thèse. Ni la thèse ni des extraits substantiels de celle-ci ne doivent être imprimés ou autrement reproduits sans son autorisation.

ISBN 0-315-64952-5

UNIVERSITY OF ALBERTA

RELEASE FORM

NAME OF AUTHOR: Jin Li

TITLE OF THESIS: $\vec{p}\vec{p} \rightarrow d\pi^+$ Analyzing Powers Near Threshold

DEGREE: Master of Science

YEAR THIS DEGREE GRANTED: 1990

Permission is hereby granted to the UNIVERSITY OF ALBERTA LIBRARY to reproduce single copies of this thesis and to lend or sell such copies for private, scholarly or scientific research purposes only.

The author reserves other publication rights, and neither the thesis nor extensive extracts from it may be printed or otherwise reproduced without the author's written permission.

Li J.

(Student's signature)

Nuclear Research Center
Department of Physics
University of Alberta
Edmonton, Alberta, Canada
T6G 2N5

Date: Sept. 20, 90

THE UNIVERSITY OF ALBERTA

FACULTY OF GRADUATE STUDIES AND RESEARCH

The undersigned certify that they have read, and recommend to the Faculty of Graduate Studies and Research for acceptance, a thesis entitled $\vec{p}p \rightarrow d\pi^+$ **Analyzing Powers Near Threshold** submitted by **Jin Li** in partial fulfilment of the requirements for the degree of Master of Science in Nuclear Physics.

L.G. Greeniaus

Supervisor Dr. L.G. Greeniaus

G. Roy

Dr. G. Roy

Hel S. Sherif

Dr. H.S. Sherif

External Examiner Dr. L. Sigurdson

Date: 17 Sept 90

# Abstract

The reaction $\vec{p}p \rightarrow d\pi^+$ analyzing powers at 3 MeV and 7 MeV above threshold (287.52 MeV) have been measured with the TRIUMF medium resolution spectrometer. The partial-wave amplitudes $a_0$, $a_1$, and $a_2$, which dominate pion production near threshold in the reaction $\vec{p}p \rightarrow d\pi^+$, have been determined by combining these data with previous cross sections measurements (TRIUMF, E466).

As expected, it is found that s-wave pion production ($a_1$ amplitude) dominates the reaction very close to threshold, p-wave pion production becomes strong even at a few MeV above threshold, the $a_2$ amplitude dominates p-wave pion production, and the $a_0$ amplitudes is negligible.

It is found that the results of the analyzing power measurements and the previous cross sections measurements are consistent and that application of Watson's theorem is justified.

# Acknowledgement

I wish to express my sincere appreciations to my supervisor, Dr. Gordon Greeniaus, for his patience, understanding and encouragement. His commendable guidance on the course of my work on this thesis is gratefully acknowledged. The financial assistance received from his research grant is also gratefully acknowledged.

I would also like to express my appreciation to Dr. Elie Korkmaz for his enormous guidance and help throughout all phases of my work of this thesis project. His guidance, suggestions and valuable criticism on writing this thesis are much appreciated.

I would like to thank Dr. Dave Hutcheon, Dr. Cathy Choi, Dr. Nate Rodning and Dr. Dave Mack for their helps and answering my questions. My thanks go to the members of my supervisory committee, Dr. Gerald Roy and Dr. Helmy Sherif.

I would like to thank my fellow graduate students Evan Hackett, Paul McNeely, Mike Moyce, and Philip Langill for sharing their knowledge and friendship.

I would like to thank Dr. Peter Green and Jim MacKinnon for their helps in the availability of the VAX cluster for data analysis.

Finally, I wish to express my gratitude to anyone else who gave his/her help to me.

TABLE OF CONTENTS


| CHAPTER | | | PAGE |
|---|---|---|---|
| CHAPTER ONE | INTRODUCTION | | |
| 1.1 | Pion Production and Absorption | | 1 |
| 1.2 | The Pion-Deuteron System | | 2 |
| 1.2.1 | Kinematics Features | | 2 |
| 1.2.2 | Selection Rules | | 3 |
| 1.3 | Experimental Review | | 4 |
| 1.4 | Experiment 552 | | 4 |
| CHAPTER TWO | THEORETICAL REVIEW | | |
| 2.1 | Theoretical Models | | 11 |
| 2.2 | Three body Theory | | 12 |
| 2.2.1 | Outline of Three-body Theory | | 12 |
| 2.2.2 | Equations for the coupled $NN \rightarrow \pi NN$ System | | 15 |
| 2.2.3 | Numerical Result | | 16 |
| 2.3 | Rescattering Model | | 20 |
| 2.4 | Models-independent partial wave method | | 22 |
| CHAPTER THREE | EXPERIMENTAL DETAILS | | |
| 3.1 | The TRIUMF Cyclotron | | 26 |
| 3.2 | The Beamline | | 26 |
| 3.2.1 | The Beamline for E466 | | 26 |
| 3.2.2 | The Beamline for E552 | | 29 |
| 3.3 | Target | | 32 |

3.4 Detection Apparatus..... 32
3.4.1 The Medium Resolution Spectrometer (MRS)..... 32
3.4.2 Pion Monitor..... 34
3.5 In-Beam Polarimeter..... 34
3.6 Data Collection..... 38
3.7 Event trigger and Data Stream..... 39

CHAPTER FOUR DATA ANALYSIS

4.1 The LISA Data Analysis Program..... 44
4.2 Definition of Measured Observables..... 44
4.3 Event Selection..... 47
4.4 Determination of the Particle Track..... 49
4.4.1 The Scattering Angle..... 49
4.4.2 The Azimuthal Angle..... 50
4.5 Determination of Momentum..... 50
4.6 Determination of Beam Energies..... 55
4.7 General Formalism of Data Analysis..... 55
4.7.1 Formalism of Data Analysis for E466..... 55
4.7.2 Formalism of Data Analysis for E552..... 57
4.8 Result..... 62
4.8.1 The Results of Experiment 466..... 63
4.8.2 The Results of Experiment 552..... 63

CHAPTER FIVE DISCUSSION AND CONCLUSION

5.1 Partial Wave Amplitudes..... 71
5.1.1 Partial Wave Phase Shift..... 71
5.1.2 $pp \rightarrow d\pi^+$ Cross Sections Extracted from E466..... 73

5.1.3 Partial Wave Amplitudes..... 73
5.2 Conclusion..... 77

REFERENCES..... 79

APPENDIX I. VAVILOV DISTRIBUTION..... 82
I.1 Energy Loss Calculation for Heavy Charged Particles..... 82
I.2 Vavilov Distribution..... 83
I.3 Application of Vavilov Distribution to Experiment 552..... 85
References..... 87
APPENDIX II. CSB EFFECT IN THE E466..... 88
II.1 Charge Symmetry and Charge Symmetry Breaking..... 88
II.2 CSB Effect in $np \rightarrow d\pi^0$ Reaction..... 90
References..... 94

LIST OF TABLES


| TABLE | | PAGE |
|---|---|---|
| 1.1 | The partial waves contributing to the reaction $pp \rightarrow d\pi^+$ | 5 |
| 1.2 | Table of reference No. for $NN \leftrightarrow d\pi$ measurements | 6 |
| 3.1 | Analyzing power of polyethylene | 38 |
| 3.2 | The values of the ECL parameters | 42 |
| 3.3 | The description of the event structure | 43 |
| 4.1 | The values of the correction factor in E552 | 60 |
| 4.2 | Measured values of $np \rightarrow d\pi^0$ total cross sections, ratios of Legendre coefficients and p-wave to s-wave strength as a function of beam energy | 65 |
| 4.3 | Experimental values of $\alpha$ and $\beta$ | 65 |
| 4.4 | $pp \rightarrow d\pi^+$ analyzing power angular distributions | 69 |
| 5.1 | The partial-wave phase shifts for NN and $\pi$d scattering near the pion production threshold | 72 |
| 5.2 | The Legendre-polynomial coefficients $A_0$ and $A_2$, and constant C for the reaction $pp \rightarrow d\pi^+$ | 72 |
| 5.3 | The magnitudes of the partial-wave amplitudes | 74 |
| II.1 | The values of the angle-average asymmetry in E466 | 93 |

LIST OF FIGURES


| FIGURE | | PAGE |
|---|---|---|
| 1.1 | The $d\pi \rightarrow NN$ total cross section calculated by VBB | 8 |
| 2.1 | Pion absorption diagrams | 12 |
| 2.2 | Feynman diagrams of theoretical models | 13 |
| 2.3 | Diagrams of cross sections and analyzing power | 18 |
| 2.4 | $pp \rightarrow d\pi^+$ Polarization observables at 567 MeV | 19 |
| 2.5 | Total cross section, differential cross sections, $A_2$ and $A_4$ | 21 |
| 2.6 | Bugg's results for partial wave amplitudes | 24 |
| 2.7 | Angular dependences of spin-dependent observables for the $pp \rightarrow d\pi^+$ reaction at $T_p$ = 578 MeV | 25 |
| 3.1 | General layout of the TRIUMF facility | 27 |
| 3.2 | Schematic view of the CHARGEX neutron-beam facility, liquid hydrogen $LH_2$ target | 28 |
| 3.3 | The proton beam transport system | 30 |
| 3.4 | The liquid hydrogen target | 31 |
| 3.5 | The Medium Resolution Spectrometer | 33 |
| 3.6 | Correlation between laboratory reaction angle and deuteron momentum | 34 |
| 3.7 | The layout of the detection apparatus | 36 |
| 3.8 | Schematic diagram of the in-beam polarimeter | 37 |
| 3.9 | Schematic of the MRS trigger | 41 |
| 4.1 | Definition of azimuthal angle | 46 |
| 4.2 | The Spectrum of Particle Identification (SPID) | 48 |
| 4.3 | Calculation of scattering angle | 49 |
| 4.4 | Calculation of azimuthal angle | 51 |
| 4.5 | The geometry of the MRS Focal Plane | 51 |

FIGURE PAGE

4.6 Correlation between laboratory reaction angle and momentum for deuteron at nominal proton-beam energies of 290.7 MeV and 294.9 MeV... 53

4.7 Correlation between lab reaction angle and momenta for the protons and deuterons in E466..... 54

4.8 The beam energy distribution for a 290.7 MeV proton beam..... 56

4.9 The beam energy distribution for a 294.9 MeV proton beam..... 56

4.10 Total $np \rightarrow d\pi^0$ cross sections as a function of pion c.m. momentum $\eta$..... 66

4.11 Ratio of legendre-polynomial coefficients, $A_2 / A_0$, as a function of pion c.m. momentum $\eta$..... 67

4.12 The spectrum of c.m. scattering angle vs azimuthal angle of deuteron for the spin up state and the spin down state..... 68

4.13 Analyzing powers for the reaction $pp \rightarrow d\pi^+$ as a function of pion c.m. angle for 290.7 and 294.9 MeV beams..... 70

5.1 The amplitudes $a_1$ and $a_2$..... 75

5.2 Comparison of analyzing powers from E466 and E552..... 76

5.3 Analyzing power for the reaction $pp \rightarrow d\pi^+$ at pion c.m. reaction angle equal to 90° as a function of beam energy..... 78

I.1 The energy loss distribution of 140 MeV deuterons traversing a $LH_2$ target of thickness 0.75 cm in E552..... 86

II.1 Illustration of charge symmetry constraints on $np \rightarrow d\pi^0$ reaction in center-of-mass system..... 90

II.2 The forward-backward asymmetry in $d\sigma/d\Omega$ for $np \rightarrow d\pi^0$ as a percentage of $d\sigma/d\Omega$ at three c.m. angles (0°, 45° and 60°) as a function of neutron laboratory energy..... 92

# List of Symbols, Nomenclature or Abbreviations

| | |
|---|---|
| $a_0$, $a_1$, and $a_2$ | Partial-wave amplitudes |
| $a_{\pi d}$ | $\pi$d scattering length |
| $A_0$, $A_1$, and $A_2$ | Legendre polynomials coefficients |
| $A_y$, $A_{zz}$, and $A_{zx}$ | Analyzing powers |
| ADC | Analog to Digital Converter |
| bpi | bytes in inch |
| $C(\theta)$, C | Fitting constant (see sec. 5.1.2) |
| CHARGEX | Charge Exchange |
| DIP | Dipole scintillator inside the MRS dipole magnet |
| ECL | Emitter-Coupled Logical |
| F | Flux |
| FEC | Front End Chamber |
| FES | Front End Scintillator |
| IBP | In-Beam Polarimeter |
| ID | Internal Diameter |
| $\mathfrak{L}$ | The orbital angular momentum in NN channel |
| L | The orbital angular momentum in $\pi$d channel |
| $L_N$ | The orbital angular momentum for the spectator nucleon in the deuteron |
| $L_\pi$ | The orbital angular momentum in $\pi$N channel |
| $LH_2$ | Liquid Hydrogen |
| LISA | Data analysis computer program |
| LT | Computer live time |
| MRS | Medium Resolution Spectrometer |
| n | Counts |

| | |
|---|---|
| NN | Nucleon-Nucleon (a two-nucleon state) |
| NΔ | Nucleon-Delta (a state with one nucleon and one delta) |
| $P_b$, $P^{\uparrow}$ and $P^{\downarrow}$ | Averaged, spin up, and spin down beam polarization respectively |
| $P_1(\cos\theta)$, $P_2(\cos\theta)$ | Legendre polynomials |
| QUAD | Quadrupole magnet |
| S1 | A scintillator at the exit of the MRS |
| S2 | A scintillator at the exit of the MRS which is behind S1 |
| SAID | Scattering Analysis Interactive Dial-in program |
| SETR | External trigger scintillator |
| SITR | Internal trigger scintillator |
| SIRC | Internal recoil scintillator |
| SLT | Slit scintillators at the entrance of the MRS |
| SPID | Spectrum for Particle IDentification |
| TDC | Time to Digital Converter |
| TOF | Time-of-Flight |
| TRIUMF | TRI-University Meson Facility |
| $T_p$ | Beam laboratory kinetic energy |
| $T_{tgt}$ | Thickness of target in nuclei per unit area |
| X0 | The second plane in FECs to measure vertical position |
| X1 | x-coordinate in the first VDC |
| X2 | x-coordinate in the second VDC |
| XF | Focal plane position |
| XM | The first plane in FECs to measure vertical position |
| Y0 | The second plane in FECs to measure horizontal position |
| YM | The first plane in FECs to measure horizontal position |
| VDC | Vertical Drift Chamber |
| VDACS | Data Acquisition and Analysis System |

| | |
|---|---|
| $\alpha$, $\beta$ | Fitting constants in $\sigma_{tot} = \alpha\eta + \beta\eta^3$ |
| $\gamma$ | Correction factor for Eq. (4.31) to the spin up/down differences in beam flux and computer live time |
| $\delta$ | Tilt of the focal plane with respect to the VDCs |
| $\delta_i$ | Partial-wave phase shift (i = 0, 1, 2) |
| $\Delta$ | The Delta resonance (a nucleon resonance at 1232 MeV) |
| $\varepsilon$ | Asymmetry |
| $\eta$ | Pion momentum in center-of-mass system in unit of pion rest mass |
| $\theta$ | Scattering angle |
| $\theta_x$ | Scattering angle in the vertical direction |
| $\theta_y$ | Scattering angle in the horizontal direction |
| $\theta_{MRS}$ | The angle to which MRS was moved to cover as much of the cone of the deuteron angles as possible |
| $\sigma$ | Cross section |
| $d\sigma/d\Omega$ | Differential cross section |
| $\Omega$ | Solid angle |
| $\phi$ | Azimuthal angle |
| $\Phi(\phi)$ | Acceptance of the detection apparatus |

# Chapter 1 Introduction

## 1.1 Pion Production and Absorption

The study of short-ranged phenomena in nuclei was the original goal of intermediate energy physics. In recent years, the description of hadronic interactions has begun to include explicit quark degrees of freedom. For example, the softening of the quark momentum distribution observed in deep inelastic lepton[1] scattering has been interpreted as a modification of quark confinement in the nuclear medium, and such explanations as a larger bag size or tunneling have been suggested[2]. The hard core of the nucleon-nucleon interaction has been interpreted in terms of explicit six-quark bag states[3]. Thus, the original interest in hadronic interactions at short distances now focuses upon their relationship with the confinement mechanism. Since the pion is intimately involved in some models of confinement, pion interactions may be a particularly direct probe of this mechanism.

Pion absorption reactions result in a large energy and momentum transfer to two or more nucleons in the nucleus, and thus can involve short relative distances. Although reactions such as inelastic electron scattering may be used to study the nuclear single particle wave function, the pion absorption process depends directly upon the wave function of the absorbing structure. In addition, the reaction itself may involve short range mechanisms. When results of kinematically complete experiments are compared with those from electron scattering, the effects of reaction mechanism and nuclear structure can be clearly separated.

Pion absorption is a fundamental hadronic phenomenon. The simplest possibility, the process $\pi N \rightarrow N$ is kinematically forbidden on a free nucleon since energy and momentum cannot be conserved. Hence the next simplest case involves the absorption on two nucleons, $\pi NN \rightarrow NN$. The particular case, $d\pi^+ \rightarrow pp$, is the simplest to study experimentally because of the two-body final state.

The understanding of the pion-deuteron interaction is important for two reasons. First, the πd system is of intrinsic interest in its own right. It is one of the best cases, both experimentally and theoretically, for investigations of the three-body problem. On the other hand, the fact that the πd system can be treated by three-body techniques is by itself not fundamental to pion-nuclear physics. Second, the structure of the deuteron is well understood; this makes the πd system an ideal testing ground of the mechanisms of pion-nuclear interactions under controlled conditions.

## 1.2 The Pion-Deuteron System

### 1.2.1 Kinematical Features

Consider the kinematics of the process

$$\pi d \rightarrow NN$$

with the deuteron at rest. The incoming pion momentum $\vec{q}$ and energy $\omega = (\vec{q}^2 + m_\pi^2)^{1/2}$ are shared between the final nucleons. If they have momenta $\vec{p}_1$ and $\vec{p}_2$ with the corresponding kinetic energies $T_1$ and $T_2$ we have

$$\omega \approx T_1 + T_2 \qquad (1.1a)$$

$$\vec{q} = \vec{p}_1 + \vec{p}_2 \; . \qquad (1.1b)$$

The small deuteron binding energy has been neglected. After absorption of a pion at rest ($\omega = m_\pi$, $\vec{q} = 0$),

$$\vec{p}_1 = -\vec{p}_2 \qquad (1.2a)$$

$$T_1 = T_2 = \frac{1}{2} m_\pi \; . \qquad (1.2b)$$

Hence the relative momentum $\vec{p}_{rel} = \frac{1}{2}(\vec{p}_1 - \vec{p}_2)$ is approximately

$$|\vec{p}_{rel}| = p_1 = p_2 = (M_n m_\pi)^{1/2} \approx 360 \text{ MeV/c} \qquad (1.3)$$

This is a large momentum compared to the typical momentum scale of a nucleon in the deuteron. Although the absorption process is allowed, there is a considerable mismatch between the required relative momentum and the momenta readily available in the deuteron. This mismatch is a characteristic feature of pion absorption both in the deuteron and in complex nuclei. The requirement of large momentum exchange between the two nucleons makes pion absorption sensitive to the dynamics of the πNN system at relatively short distance.

The pion absorption and production processes are related to each other by the principle of detailed balance, for example

$$\sigma(\pi^+ d \rightarrow pp) = \frac{2}{3}\frac{p^2}{q^2}\sigma(pp \rightarrow \pi^+ d), \qquad (1.4)$$

where q is the pion momentum and p the nucleon momentum in the center-of-mass system and σ denotes cross section.

### 1.2.2 Selection Rules

From isospin conservation it follows that the nucleon pair in the reaction $NN \leftrightarrow \pi d$ has isospin I=1. Consequently, both the total and differential cross-sections for production of charged and neutral pions are related by

$$\sigma(pp \rightarrow \pi^+ d) = 2\,\sigma(pn \rightarrow \pi^0 d). \qquad (1.5)$$

The notation used here for orbital angular momenta is, schematically,

$$NN(\mathfrak{L}) \rightarrow \pi d(L) \equiv \pi N(L_\pi) + N(L_N),$$

i.e., the orbital angular momentum is $\vec{L}$ in the NN channel, L in πd and the spectator nucleon in the deuteron has orbital angular momentum $L_N$ in the overall center-of-mass frame. Table 1.1 gives the partial waves considered here, and the notation of Mandl and Regge[4] as extended by Blankleider and Afnan[5]. Close to threshold the process is dominated by the s-wave πd interaction (L=0). The NN pair has therefore total angular momentum J=1, negative parity, and isospin I=1. This specifies uniquely that the nucleons are in a $^3P_1$ state. With increasing energy the p-wave πd interaction (L=1) becomes important. The two nucleons have I=1 as before, but the parity is now positive with the possible total angular momentum states J=0,1 and 2. The nucleons must then be in a spin-singlet state, and only the $^1S_0$ and $^1D_2$ states are possible. The s- and p-wave contributions dominate up to the region of excitation of the Δ-resonance in the intermediate πN channel.

## 1.3 Experimental Review

A general review of the experimental situation up to 1984 for pion production and absorption in nucleon-nucleon collisions was presented by G. Jones[6,7] and Hiroshige *et al.*[8] In 1988, Hutcheon *et al.*[9] carried out precise measurements of $np \rightarrow d\pi^0$ cross sections from threshold to 10 MeV above threshold (Experiment 466 at TRIUMF). These measurements are described in chapters. 3 and 4. Table 1.2 lists a review of $NN \leftrightarrow d\pi$ measurements for equivalent initial proton kinetic energy up to 100 MeV above threshold.

## 1.4 Experiment 552 at TRIUMF

A special feature of the reaction $NN \rightarrow d\pi$ near threshold is the suppression of the normally-dominant NΔ intermediate state in favor of πN s-wave rescattering. For a wide range of beam energies from 350 to 750 MeV the short-range interaction is dominated by the process of emission of a pion by one nucleon, its absorption by the other nucleon to form an intermediate N-Δ state, and the emission of a pion upon decay of the Δ. The $P_{33}$ πN scattering (Δ resonance) is of long range, and in fact the dominant partial wave amplitude has the initial nucleons in a relative D state (refer to table 1.1). Paradoxically, as

**Table** 1.1 The partial waves, up to h-wave pions, contributing to the reaction $pp \rightarrow d\pi^+$. The last two columns show the dominant $\pi N$ contributions.

| Amplitude designed | $J^\pi$ | Pion wave | L ($\pi$d) | $\mathfrak{T}$ (pp) | S (pp) | $^{2S+1}(\mathfrak{T})_J$ (pp) | $(L_\pi)_{2T',2J'}$ ($\pi$N) | $L_N$ (N) |
|---|---|---|---|---|---|---|---|---|
| $a_0$ | $0^+$ | p | 1 | 0 | 0 | $^1S_0$ | $P_{11}$ | 0 |
| | | | | | | | $P_{33}$ | 2 |
| $a_1$ | $1^-$ | s | 0 | 1 | 1 | $^3P_1$ | $S_{11}$ | 0 |
| | | | | | | | $S_{31}$ | 0 |
| | | | | | | | $P_{33}$ | 1 |
| $a_2$ | $2^+$ | p | 1 | 2 | 0 | $^1D_2$ | $P_{33}$ | 0 |
| $a_3$ | $1^-$ | d | 2 | 1 | 1 | $^3P_1$ | | |
| $a_4$ | $2^-$ | d | 2 | 1 | 1 | $^3P_2$ | $P_{33}$ | 1 |
| $a_5$ | $2^-$ | d | 2 | 3 | 1 | $^3F_2$ | $P_{33}$ | 1 |
| $a_6$ | $3^-$ | d | 2 | 3 | 1 | $^3F_3$ | $P_{33}$ | 1 |
| $a_7$ | $2^+$ | f | 3 | 2 | 0 | $^1D_2$ | | |
| $a_8$ | $4^+$ | f | 3 | 4 | 0 | $^1G_4$ | | |
| $a_9$ | $3^-$ | g | 4 | 3 | 1 | $^3F_2$ | | |
| $a_{10}$ | $4^-$ | g | 4 | 3 | 1 | $^3F_4$ | | |
| $a_{11}$ | $4^-$ | g | 4 | 5 | 1 | $^3H_4$ | | |
| $a_{12}$ | $5^-$ | g | 4 | 5 | 1 | $^3H_5$ | | |
| $a_{13}$ | $4^+$ | h | 5 | 4 | 0 | $^1G_4$ | | |
| $a_{14}$ | $6^+$ | h | 5 | 6 | 0 | $^1I_6$ | | |

T' and J' are the total isospin and angular momentum of $\pi$N system, respectively.

**Table** 1.2 Table of Reference No. for NN ↔ dπ Measurements.

Symbols used for the different isospin channels and reaction direction are * ($np \rightarrow d\pi^0$), + ( $d\pi^0 \rightarrow np$), # ( $d\pi^+ \rightarrow pp$), and no symbol ($pp \rightarrow d\pi^+$). $T_p$ is the equivalent energy for $pp \rightarrow d\pi^+$.

| $T_p$ (MeV) | Types of Measurement | | |
|---|---|---|---|
| | $\sigma_T$ | $\frac{d\sigma}{d\Omega}$ | $A_{y0}$ |
| 287.6 -- 303 | 9* | 9* | |
| 291 -- 324 | 10+ | | |
| 305 | | | 11 |
| 310 | | | 11 |
| 320 | | 11 | 11 |
| 325 | 12 | 16* | |
| 330 | | 11 | 11 |
| 332 | 15 | 13#, 15 | |
| 338 | 15 | 15 | |
| 350 | | 11 | 11 |
| 363 | 18# | 18# | |
| 375 | | 11, 16* | 11, 14 |
| 378 | | 13# | 14 |
| 383 | | 17# | |
| 400 | | 11 | 11 |

the beam energy is lowered towards threshold the long-range Δ mechanism is suppressed by the centrifugal barrier for low-energy pions, and a window of sensitivity to the short-range N-N interaction opens up. In pion-nucleon models the reaction mechanism near threshold is the s-wave rescattering of a pion by the second nucleon, rather than Δ-formation. Alternatively, one might model the intermediate state by a 6-quark cluster.

The $pp \rightarrow d\pi^+$ reaction can also be discussed in terms of partial-wave amplitudes (see table 1.1). Well above threshold the transition amplitude $a_2$, the conduit for the NΔ ($L_N$=0) intermediate state, is dominant. As the beam energy drops towards threshold, $a_2$ diminishes due to the centrifugal barrier of the p-wave pion. Amplitude $a_1$ is small because of near-complete cancellation of the $S_{11}$ and $S_{31}$ terms, but near threshold becomes relatively large because it is the only amplitude with s-wave pions. The amplitude $a_0$ is even smaller than $a_2$ because the $P_{11}$ ($L_N$=0) and $P_{33}$ ($L_N$=2) contributions are themselves small and interfere destructively[19].

This qualitative description of the $NN \rightarrow d\pi$ reaction is confirmed in pion-nucleon model calculations, which show the fall-off of $P_{33}$ scattering relative to πN S-wave scattering as the energy approaches the threshold limit. Figure 1.1 is a calculation by Vogelsang, Bakker and Boersma[20] of total cross section as a function of η, the pion center-of-mass momentum in units of the pion rest mass.

Measurement of the differential cross section permits a fairly good separation of the contributions of s-wave (L=0) and of p-wave (L=1) pion production. The separation is not exact, however, nor can the Δ and non-Δ parts of the p-wave production be distinguished from one another. These features of the reaction can be seen using two further pieces of information, one of which is knowledge of the analyzing power $A_y$ and the other a constraint imposed by elastic scattering NN and dπ phase shifts.

Assuming that only s- and p-wave pion production need to be considered near threshold, the three partial-wave amplitudes $a_0$, $a_1$ and $a_2$ will contribute. The spin-independent differential cross section can be expressed in terms of partial-wave amplitudes and Legendre polynomials $P_L$ as[21]

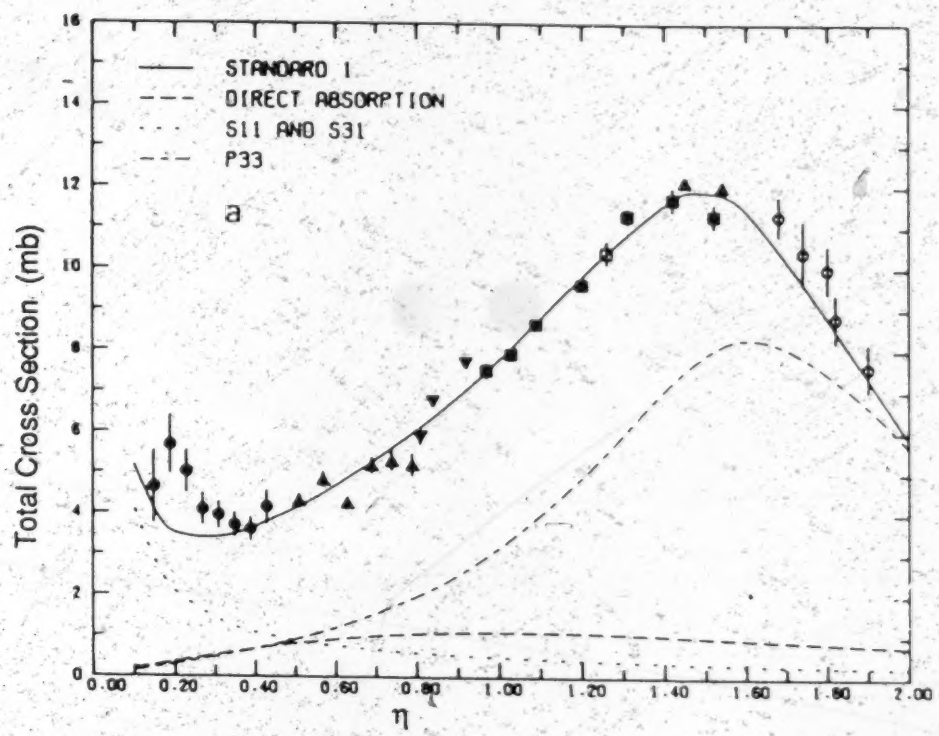


Fig. 1.1 The $\pi d \rightarrow NN$ Total Cross Section Calculated by VBB (Ref. 25). The solid line represents the complete result of the Standard-1 calculation (see sec. 2.3). The dashed, dotted, and dot-dashed curves represent the results for the direct absorption, the $S_{11}$ and $S_{31}$ rescattering, and the $P_{33}$ rescattering (see fig. 2.1), respectively.

$$4\pi\left(\frac{d\sigma}{d\Omega}\right)_0 = \frac{1}{4}\left[|a_0|^2 + |a_1|^2 + |a_2|^2\right] + \left[\frac{1}{4}|a_2|^2 - \frac{1}{\sqrt{2}}\,\mathrm{Re}(a_0 a_2^*)\right] P_2(\cos\theta)\,. \quad (1.6)$$

The spin-dependent differential cross section (spin-independent cross section multiplied by analyzing power $A_y$ ) is given by

$$4\pi\left(\frac{d\sigma}{d\Omega}\right)_0 A_y = \left[\frac{1}{4}\,\mathrm{Im}(a_1 a_2^*) - \frac{1}{2\sqrt{2}}\,\mathrm{Im}(a_0 a_1^*)\right] P_1^1(\theta)\,. \quad (1.7)$$

Defining $r_0 = |a_0| / |a_1|$ , $r_2 = |a_2| / |a_1|$ , and the phase of amplitude i as $\delta_i$ ,

$$4\pi\left(\frac{d\sigma}{d\Omega}\right)_0 A_y = |a_1|^2\left[\frac{1}{4} r_2 \sin(\delta_1 - \delta_2) - \frac{1}{2\sqrt{2}} r_0 \sin(\delta_0 - \delta_1)\right] P_1^1(\theta)\,, \quad (1.8)$$

where the associated Legendre function $P_1^1(\theta) = \sin\theta$ and $(d\sigma/d\Omega)_0$ is the spin-independent differential cross section.

In Experiment 466 at TRIUMF[9], the total cross sections and cross section angular distributions for the $np \rightarrow d\pi^0$ reaction at a number of beam energies from 1 to 16 MeV above threshold (threshold = 275.07 MeV) were measured. The extracted $A_0$ (total cross section) and $A_2$ coefficients of the differential cross section

$$4\pi\left(\frac{d\sigma}{d\Omega}\right)_0 = A_0 + A_2 P_2(\cos\theta) \quad (1.9)$$

can be used to determine the magnitudes of amplitudes $a_1$ and $a_2$ only to the extent that $a_0$ is negligible. It was thus interesting to complement the cross section data by measuring the near-threshold analyzing powers. As seen from the spin-dependent cross section expression (1.8), a combination of cross section and analyzing power data should provide more accurate determination of all three amplitudes. The analyzing power $A_y$ depends upon the interference between an s-wave pion production amplitude ($a_1$) and two p-wave

amplitudes ($a_0$ and $a_2$) and combined with Watson's Theorem[22], which states that the phase of a partial wave amplitude in $NN \rightarrow d\pi$ is the sum of phase shifts for the same partial waves in NN and in $\pi d$ elastic scattering, allows the magnitudes of the smaller p-wave amplitudes to be determined.

This thesis reports the results of recent experiment 552 at TRIUMF, a measurement of the polarization analyzing powers for the reaction $\vec{p}p \rightarrow d\pi^+$ at 3 and 7 MeV above threshold (287.51 MeV). Ideally, the analyzing powers would be measured for the reaction $np \rightarrow d\pi^0$, as for previous near-threshold cross sections measurements. We have considered such a measurement, but found two serious problems concerning the polarization of the neutron beam: (1) for any practical neutron production reaction the polarization is about -1/3 that of the primary proton beam, requiring 9-fold greater statistical accuracy to get the same errors in $A_y$, and (2) there is no direct measurement to better than 15-20% of the polarization transfer coefficient in probable production reactions. This error would propagate through as a systematic uncertainty in $A_y$. The experiment was performed by a collaboration between TRIUMF and the University of Alberta. The experimental details and results of E552, as well as E466, are discussed in chapter 3 and 4, respectively. Chapter 5 gives the partial wave amplitudes for the reaction $pp \rightarrow d\pi^+$. A brief review of current theoretical work in this area will be given in chapter 2. It is also interesting to investigate the effect of charge symmetry breaking in $np \rightarrow d\pi^0$ reaction using the data of experiment 466, which is discussed briefly in appendix II.

# Chapter 2 Theoretical Review

## 2.1 Theoretical models

The theoretical approaches currently applied to the NN $\leftrightarrow$ d$\pi$ reaction can be roughly divided into three main categories[6,23].

The first, based on perturbation theory[20,24,25] and illustrated diagrammatically in figure. 2.1, is described in sec. 2.3.

The second is a coupled-channels model[26,27] illustrated diagrammatically in Fig. 2.2b. Such coupling of the NN and N$\Delta$ channels includes exchange implicitly and provides a full summation over pion multiple scattering. This approach, however, is non-relativistic and involves static channel-coupling potentials. For the first time, however, theory was able to provide predictions[27] which compared well with experimental measurements not only of the differential and total cross-sections, but also of a variety of polarization observables. This model was the first to include up to f-wave angular momentum channels for the pions (f-wave arising from the $^1G_4$ pp state which couples to the D-wave N-$\Delta$ intermediate state). This theoretical approach was a forerunner of the current $\Delta$-hole models used in considerations of pion interactions with nuclei.

The third approach, based on the application of Faddeev techniques[5,28,29,30], enabled exact summation over all multiple scatterings of the pion. This technique is illustrated diagrammatically in Fig. 2.2c. A major result of this technique was the achievement of exact two-body and three-body unitarity. In this way, NN scattering, the NN $\rightarrow$ $\pi$d reaction, NN $\rightarrow$ N$\Delta$ coupling and $\pi$d elastic scattering are all related within a single framework. This is illustrated diagrammatically in Figs. 2.2d-f.

A basic drawback in all the above theories is that they are non-relativistic. This, of course, makes them somewhat questionable, particularly at higher energies where dibaryonic resonances have been suggested. To remedy this situation, Grein *et al.*[31] have recently embarked on a totally relativistic study of the pp $\rightarrow$ d$\pi$ reaction, but their results

indicate that relativistic effects are not sufficient to account for the disagreement between theory and experiment and that further physics input is needed[32,33].

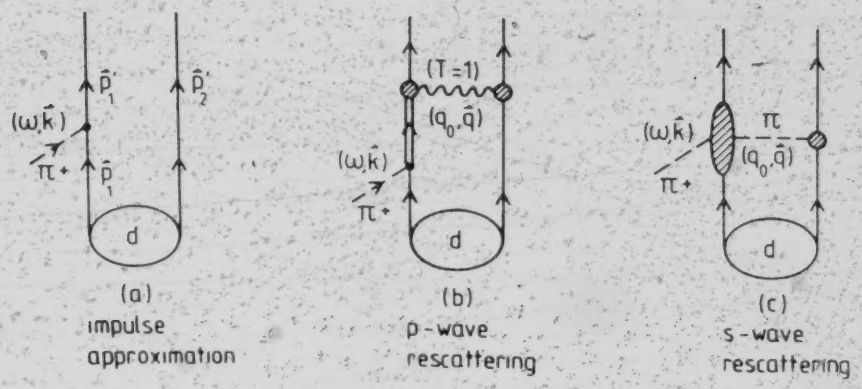


Fig. 2.1 Pion absorption diagrams. The wavy line in diagram (b) represents one pion exchange plus $2\pi$ exchange; the circular shaded areas in diagrams (b) and (c) represent the extended structures of the $\pi NN$ and $\pi N\Delta$ vertices; the elliptical shaded area in diagram (c) represents the effective $\pi\pi NN$ s-wave vertex.

## 2.2 Three-body Approach

### 2.2.1 Outline of three-body theory

In his development of three-body scattering equations, Faddeev's starting point was potential interactions between pairs of particles. An essential step was the elimination of the two-body potentials in favour of the corresponding scattering amplitudes (t-matrices) so that similar equations occur even in cases where underlying potentials cannot be defined.

In the application of three-body theory to the $\pi NN$ system, the basic physical assumption is to restrict the framework to a form such that intermediate states contain no more than one pion. States with two and more pions are regarded to be implicit in the elementary two-body amplitudes, e.g. by the presence of two-pion exchange in the NN-potential.

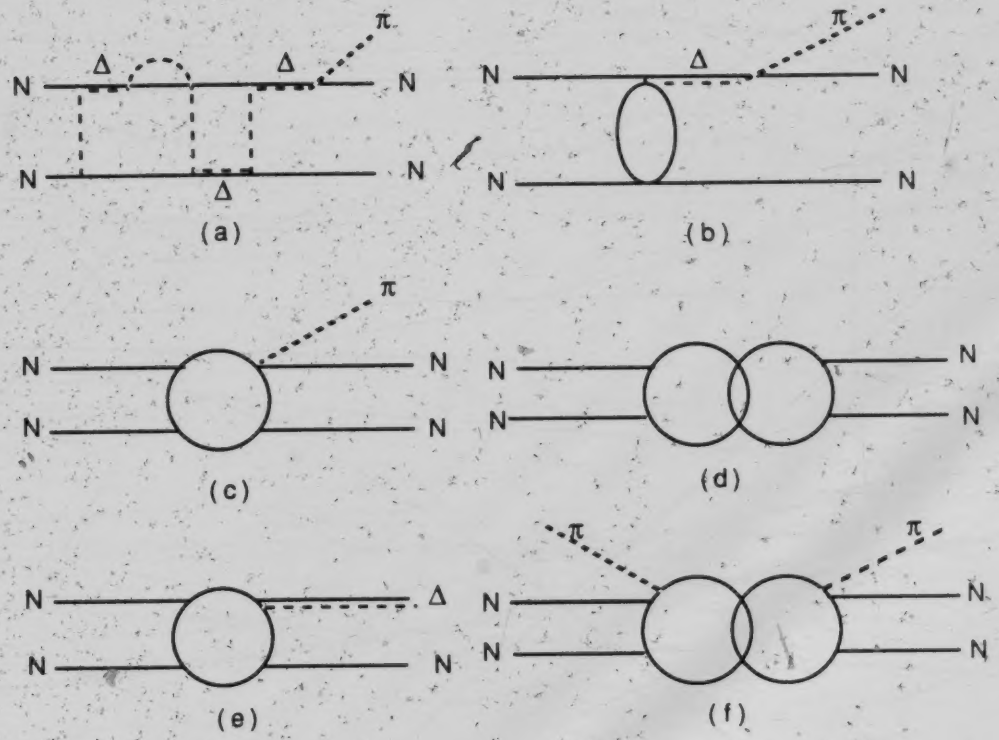


Fig 2.2 (a) Typical example of pion multiple scattering graph.

(b) Graph illustrating coupled-channels approach. The elliptical blob represents the NN-NΔ coupling.

(c) Three-body unitary approach. The circle represents exact summation over all pion rescattering.

(d,e,f) Schematic representations of the application of the 3-body unitary approach to N-N scattering, NN → NΔ coupling, and πd elastic scattering.

So as to clearly see the essential structure of the three-body equations, consider first the $\pi NN$ system in the absence of the emission and absorption process $\pi N \leftrightarrow N$. The two-body interactions therefore describe only the elastic NN and $\pi N$ scattering.

The relevant channels ($\alpha$) with $\alpha = 1, 2, 3$ are $(1) \equiv (\pi N_1)$, $(2) \equiv (\pi N_2)$, $(3) \equiv (N_1 N_2)$, where $N_1$ and $N_2$ refer to the two nucleons. Suppose that in each channel one has a two-body interaction potential $v(\alpha)$. The first step is then to introduce t-matrices in each channel by the equation

$$t(\alpha) = v(\alpha) + v(\alpha)\, G_0\, t(\alpha)\,, \tag{2.1}$$

where $G_0$ is the Green's function of the non-interacting three-body system. This means that $G_0(E) = (E - H_0)^{-1}$, where $H_0$ is the sum of the kinetic energies of all three particles. Hence eq. (2.1) is a two-body scattering equation, but with the third (spectator) particle contributing to the three-body kinematics of the process by its energy in the Green's function $G_0$.

The full three-body T-matrix becomes a sum of the repeated scattering in the different channels

$$T = \sum_{\alpha} t(\alpha) + \sum_{\beta \neq \alpha} t(\alpha)\, G_0\, t(\beta)\,. \tag{2.2}$$

This expansion can be rewritten as an integral equation by introducing the quantities $T(\alpha)$ defined by

$$T = \sum_{\alpha} T(\alpha) \tag{2.3a}$$

$$T(\alpha) = t(\alpha) + t(\alpha)\, G_0 \sum_{\beta \neq \alpha} T(\beta)\,. \tag{2.3b}$$

The structure of eq. (2.3) is physically evident. The $T(\alpha)$ receive contributions from two sources: first, from the elastic amplitudes $t(\alpha)$ in a given channel $(\alpha)$, and second, from the coupling to all other channels with $(\beta) \neq (\alpha)$.

The coupled integral equations (2.3), together with (2.1), are known as the Faddeev equations.

The $\pi$NN system can be regarded as a special example of a three-body problem with strong interacting particles. It is clear that for an adequate description of NN scattering above the pion production threshold one needs to include the coupling to the $\pi$NN channels. In the application of three-body theory to the $\pi$NN system, the basic physical assumption is to restrict the framework to a form such that intermediate states contain no more than one pion, and it is introduced by incorporating the $\pi N \leftrightarrow N$ coupling vertex into the above set of equations. This procedure explicitly generates the one-pion exchange interaction in the NN channel as well as the $P_{11}$ nucleon pole term in the $\pi$N sector. As a consequence, these terms have to be removed from the input NN potential and $\pi$N scattering amplitude.

### 2.2.2 Equations for the Coupled $NN \rightarrow \pi NN$ System

The first work in this area was a pure three-body description of the system by Afnan and Thomas[28]. In their model, the so-called bound state model (BSM), they allowed for coupling to the N-N channel by constructing a bound state in the $\pi$-N $P_{11}$ channel and then identifying this bound state with a nucleon. Effectively this means that the pion is never really destroyed and the three-body description of $\pi NN \leftrightarrow NN$ follows. Afnan and Thomas solved the Alt-Grassberger-Sandhas (AGS) equations[34] (practical form of Faddeev-like equations) at low energies and obtained successfully the coupled amplitudes for $\pi d \rightarrow \pi d$, $\pi d \leftrightarrow NN$ and $NN \rightarrow NN$ with one set of integral equations. However, there were serious theoretical problems arising from the fact that treating one of the nucleons as a $\pi$-N bound state implied that only one of the nucleons could emit a pion and the resultant model excluded a whole class of diagrams.

Blankleider and Afnan[5] overcame the difficulty of the BSM, and derived a set of coupled integral equations for the antisymmetrized physical amplitudes, called the πNN equations. The main features of these equations are that they satisfy two- and three-body unitarity — dressings of both nucleon propagators and πNN vertices are explicitly included, and they contain terms that may be identified with heavy meson exchanges. The equations, similar to the Faddeev equations, are written in matrix form as

$$\begin{bmatrix} X_{dN} \\ X_{\Delta N} \\ X_{NN} \end{bmatrix} = \begin{bmatrix} Z_{dN} \\ Z_{\Delta N} \\ Z_{NN} \end{bmatrix} + [K] \begin{bmatrix} X_{dN} \\ X_{\Delta N} \\ X_{NN} \end{bmatrix} \tag{2.4}$$

for the NN → πd and NN → NN reactions, where the kernel is given by

$$[K] = \begin{bmatrix} 0 & Z_{d\Delta}R_{\Delta} & Z_{dN}R_N \\ Z_{\Delta d}R_d & Z_{\Delta\Delta}R_{\Delta} & Z_{\Delta N}R_N \\ Z_{Nd}R_d & Z_{N\Delta}R_{\Delta} & Z_{NN}R_N \end{bmatrix} . \tag{2.5}$$

In the above expressions X are the three-body physical amplitudes related to the AGS amplitudes, Z the Born terms ( or driving terms), and R the two-body propagators in three--body Hilbert space. The index d refers to the π(NN) three-body channels, which include not only the π-d, but all channels with the N-N interacting and a spectator pion; Δ includes the $P_{11}$ nonpole part corresponding to channels N(πN) with (πN) interacting pairs and a spectator pion; and N refers to the N(N) channel where (N) is the (πN) $P_{11}$ pole part.

### 2.2.3 Numerical Result

In order to solve Eq. (2.4) one needs to specify as input separable NN and πN interactions in all included partial waves, as well as the form factor for the πNN vertex. A most important aspect of the assumed input is the construction of the $P_{11}$ interaction. Using a semirelativistic calculation (relativistic pion, non-relativistic nucleon), Blankleider and Afnan[5] solved the full set of πNN equations (2.4) by taking two-term separable potentials

$$V_{P_{11}} = |U_1\rangle\lambda_1\langle U_1| + |U_2\rangle\lambda_2\langle U_2| \,, \tag{2.6}$$

where the form factors $U_i(k)$ are of the usual Yamaguchi type

$$U_i(k) = \frac{C_i k^{n_i}}{\left(k^2+\beta_i^2\right)^{m_i}} \tag{2.7}$$

and $\lambda_i$, $C_i$, $\beta_i$, $n_i$, $m_i$ are chosen by fitting to the $P_{11}$ phase shifts and scattering length, and by requiring a pole in the corresponding $P_{11}$ t-matrix at the nucleon mass.

Typical results of such a three-body study are shown in Fig. 2.3. In Fig. 2.3a, total cross sections for $\pi^+d \rightarrow pp$ are compared with the corresponding experimental data from Richard-Serre *et al.*[35]. The agreement between theory and experiments is, in general, very good, except at high energies, where the three-body model gives a slightly large total cross section. In Fig. 2.3c the results of theory and experiment for the differential cross section for $pp \rightarrow \pi^+d$ at various proton laboratory energies are shown. Up to the resonance region ($T_p$ = 567.4 MeV), the calculated differential cross section is in very good agreement with experiment and shows very little deviation from a straight line.

The polarization observables can also be calculated by the three-body model. In Fig. 2.3b the analyzing power $A_y$ predicted by Blankleider and Afnan[5] compared with experiment is shown. It was found that $A_y$ is too large across the whole energy range. $A_y(90°)$ is dominated by interference terms between the large amplitudes of $J^\pi = 2^+$ and $3^-$ and the small ones of $0^+$ and $1^-$, so that any mechanism which affects only these smaller amplitudes would change $A_y(90°)$ without affecting the cross section greatly. Such a mechanism is provided, for example, by the deuteron D-state components and their effect on $A_y$ is displayed in Fig. 2.3b. Afnan and Mcleod[36] calculated polarization observables with some improvements on two-body input potentials. Their results are shown in Fig. 2.4.

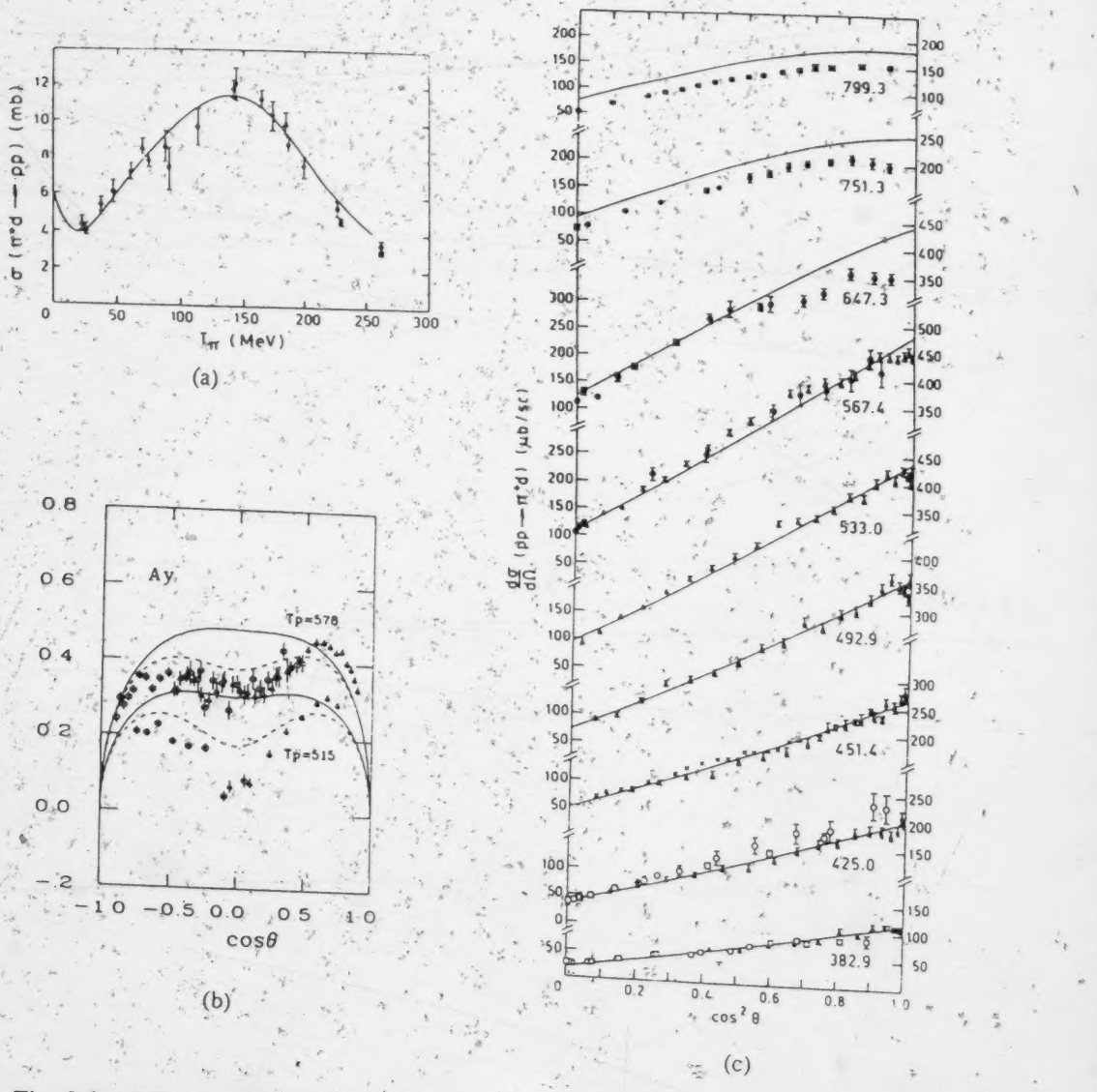


Fig. 2.3 (a) Total cross section for $\pi^+d \rightarrow pp$.

(b) The analyzing power $A_y$ for $pp \rightarrow \pi^+d$. Solid and dashed curves correspond to the results using the Reid soft core ($P_d$=6.56%) and Bryan-Scott ($P_d$=5.36%) potentials, respectively. Experimental points are from Ref. 33.

(c) Differential cross sections for $pp \rightarrow \pi^+d$ at the laboratory incoming proton energies shown.

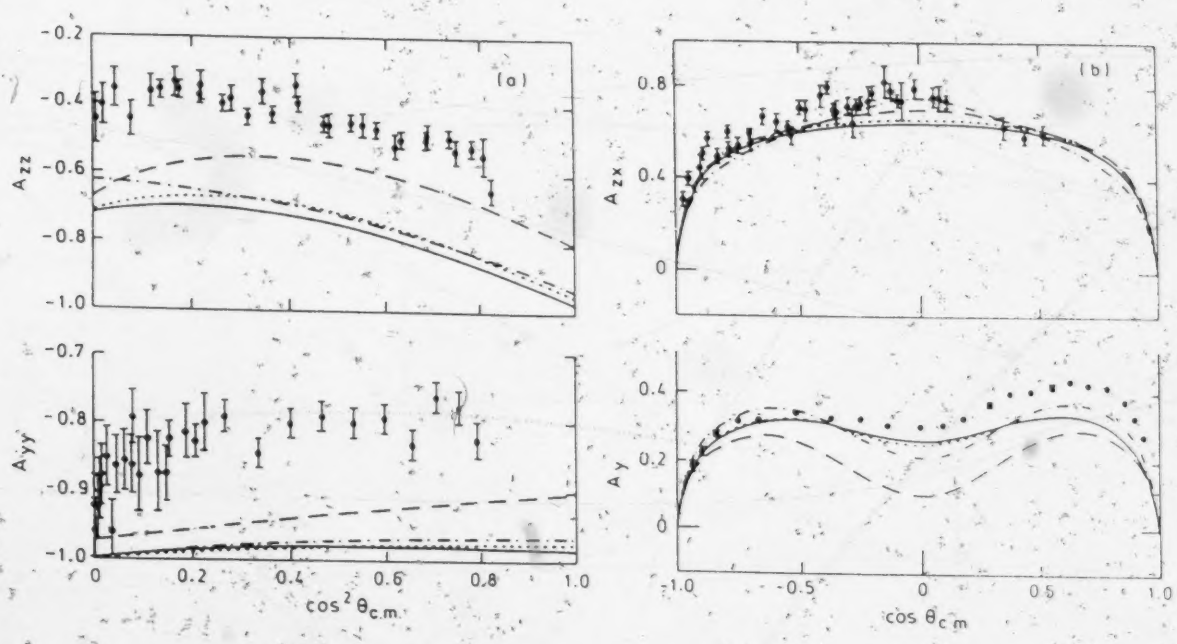


Fig. 2.4 A comparison of $pp \rightarrow \pi^+ d$ observables at $T_p = 567$ MeV for different $P_{11}$ interactions.

Overall, the NN-πNN calculations give a reasonable description of the experimental results, and the agreement between theory and experiment would improve if the input amplitudes particularly in the $P_{11}$ channel could be constrained. It is also clear that the F-wave N-N and π-N amplitudes need to be included.

## 2.3 Perturbation-theory model[20,24,25,37]

The perturbation theory is a simpler model based on the three T-matrix contributions depicted in Fig. 2.1: the impulse approximation, a p-wave rescattering mechanism involving the excitation of an intermediate $\Delta_{33}$ resonance followed by pion and ρ-meson exchange, and an s-wave rescattering mechanism based upon the phenomenological, zero-range Lagrangian of Koltun and Reitan[38]. The rescattering contributions are necessitated by the kinematics of the reaction which require a large momentum transfer between the two nucleons in order to conserve both energy and momentum. This is difficult to achieve with the impulse approximation alone, and in fact, the impulse approximation does not even yield the right order of magnitude for the cross section. Inclusion of the p-wave rescattering mechanism not only yields the right order of magnitude but also reproduces the observed resonance structure, which is clearly associated with the intermediate $\Delta_{33}$ resonance. The s-wave rescattering mechanism is necessary to obtain the low-momentum part of the cross section correctly.

Vogelzang, Bakker and Boersma (VBB)[20] calculated the total and differential cross section with the influence of the πN T-matrix, the $P_{11}$ form factor, choice of subsystem energies, inclusion of the backward-going pion, and modification of the $S_{31}$ rescattering for the absorption of positive pions on deuterons. Almost all of these factors could cause changes of order 20% to 100% in the cross section. Their results are illustrated in figures 1.1 and 2.5. The standard-1 calculation uses the Paris deuteron wave function and a monopole form factor with a cutoff of 510 MeV/c at the absorption vertex, includes a relativistic T-matrix transformation, takes the Faddeev choice for the subsystem energies, and omits the backward-moving pion. The standard-2 calculation decreases the cutoff of

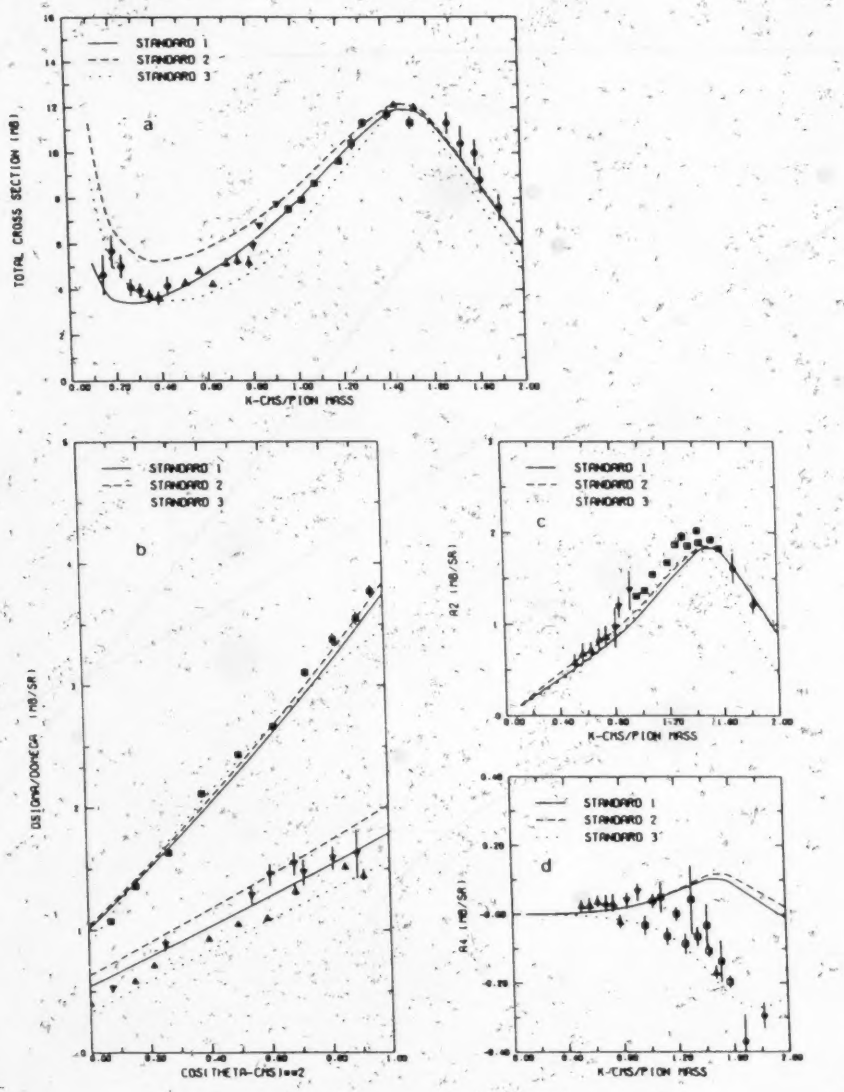


Fig. 2.5 (a) Total cross section for $\pi d \rightarrow NN$;

(b) Differential cross sections for $\pi d \rightarrow NN$ at two energies: $\eta$=0.79 ($T_\pi^{lab}$= 45 MeV, lower curves) and $\eta$=1.42 ($T_\pi^{lab}$=125 MeV, upper curves);

(c) $A_2$; (d) $A_4$.

Note: (1) K-CMS/PION MASS means $\eta$.

(2) $A_2$ and $A_4$ are the coefficients of $d\sigma/d\Omega = A_0 + A_2P_2(\cos\theta) + A_4P_4(\cos\theta) + \cdots$.

(3) The curves are explained in the text.

the monopole absorption form factor to 380 MeV/c, and includes the backward-moving pion. The standard-3 calculation includes the backward-moving pion and uses the Blankenbecler-Sugar subsystem energies and a monopole form factor with a cutoff at 470 MeV/c.

## 2.4 Model-independent Partial Wave Analysis

Partial wave analyses of the existing data base of the reaction $pp \rightarrow \pi^+ d$ were carried out by several groups. Hiroshige *et al.*[8] provided two basic choices of amplitudes, each of which fits the data. They obtained their solutions by performing an energy-dependent analysis of data, one in which the amplitudes are required to be continuous functions of energy. In addition, a threshold momentum dependence expected on the basis of centrifugal penetrability was imposed. They provided two basic fits, one having a dominant $a_2$ amplitude (called solution D), and the other a dominant $a_0$ amplitude (called solution S) (see table 1.1 for a definition of these amplitudes). Kravtsov *et al.*[39] did a similar energy-dependent partial wave analysis. The energy range covered in the latter analysis is rather higher than for the others, extending from 400 MeV to 1235 MeV.

An extensive amplitude fit was also performed by D. Bugg[22,40]. He considered only those amplitudes corresponding to channels containing S- and P-wave $N\Delta$ intermediate states. As well , the $a_0$ amplitude (expected to be small) was arbitrarily set equal to zero. In his analysis, Blankleider's calculations[5] are used (a) to fix high partial waves with $L_\pi \geq 3$ in both initial and final states (and also the small amplitude $a_3$), (b) to constrain loosely phases of most low partial waves. The latter is motivated by the Watson theorem, which states that if NN, $\pi d$ and $NN\pi$ channels are weakly coupled, then partial-wave amplitudes for the $NN \rightarrow \pi d$ reaction are given by

$$a = |a| e^{i\varphi} = |a| e^{(\delta_{NN} + \delta_{\pi d})}, \qquad (2.12)$$

where $\delta_{NN}$ and $\delta_{\pi d}$ are the phase shifts for NN and $\pi d$ elastic scattering respectively for the same partial wave. This is true only close to the inelastic threshold and the relation breaks down at energies where the three-body final state has significant K-matrix elements.

Bugg's analysis respects Watson's theorem for all amplitudes below 450 MeV.

Typical results[22,40] are shown in figure 2.6 in comparison with predictions of Blankleider[5] and of Niskanen[27]. The amplitudes $a_2$, $a_5$ and $a_6$ agree well with both theoretical predictions. However, the amplitudes $a_1$ and $a_4$ differ significantly from both predictions. This may be due to the exclusion of $\rho$ exchange in Blankleider's calculation since it is known that both amplitudes are sensitive to $\rho$ exchange.

The agreement of the different partial wave solutions with the existing data is shown in figure 2.7.

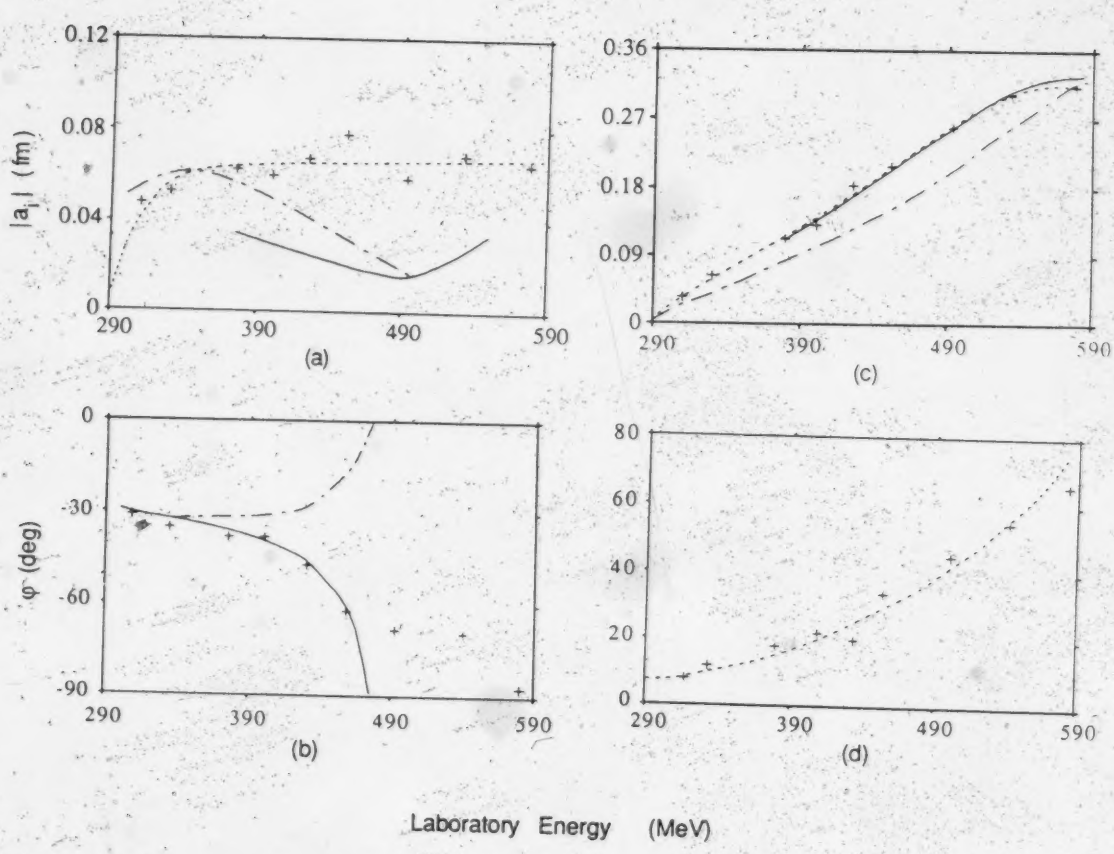


Figure 2.6 Results of the analysis of Bugg *et al.*(Refs. 22 and 40) for (a) $|a_1|$ (b) $\varphi(a_1)$ (c) $|a_2|$ (d) $\varphi(a_2)$. The dashed curves are drawn to guide the eye. The full and dot-dashed curves are predictions of Blankleider (Ref. 5) and Niskanen (Ref. 27), respectively.

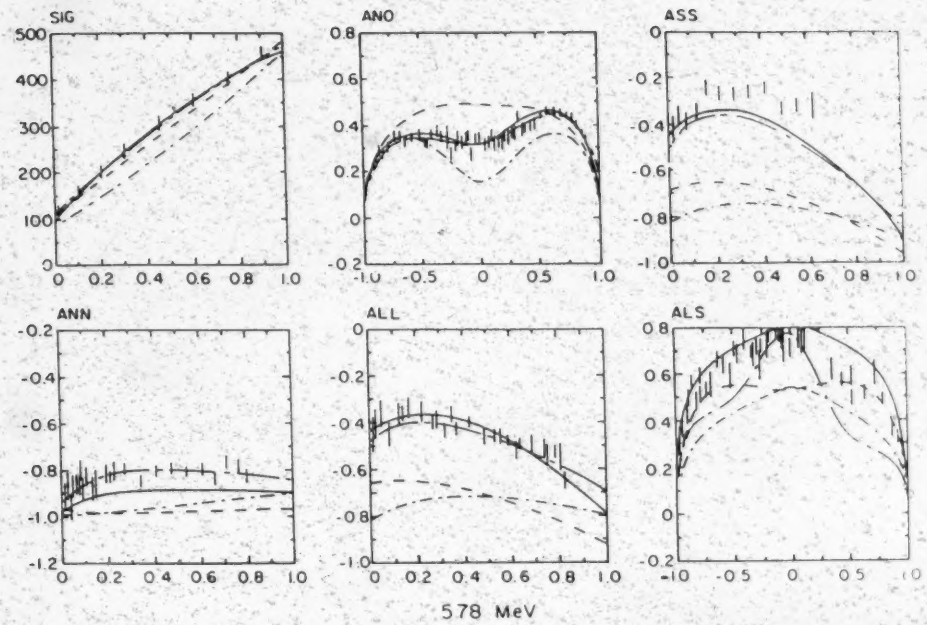


Fig. 2.7 Angular dependences of spin-dependent observables for the $\vec{p}\vec{p} \rightarrow d\pi^+$ reaction at $T_p$ = 578 MeV. Vertical bars indicate the experimental data in ref. 33.

( ——— — ———) Hiroshige *et al.* "D" amplitudes (Ref. 8)

( ——————— ) Bugg amplitudes (Ref. 22)

( – – – – – – – – – – – ) Blankleider amplitudes (Ref. 5)

( —— — —— — —— —) Rinat amplitudes (Ref. 41)

For X coordinates labelled $0 \rightarrow 1$, the relevant variable is $\cos^2 \theta$.

For X coordinates labelled $-1 \rightarrow +1$ the relevant variable is $\cos \theta$.

SIG indicates differential cross section. The remaining observables are analyzing power or spin correlation functions labelled for a proton beam and target polarized in normal (N) to the reaction plane, sideways (S), longitudinally (L).

# Chapter 3 Experimental Details

## 3.1 The TRIUMF Cyclotron

TRIUMF (TRI-University Meson Facility ) is Canada's national meson facility, and is jointly managed by four universities: the University of Alberta, Simon Fraser University, the University of British Columbia and the University of Victoria.

The TRIUMF cyclotron is a six-sector isochronous cyclotron accelerating $H^-$ ions to 520 MeV. Beam extraction is achieved by passing part or all of the $H^-$ circulating beam through a carbon stripping foil, creating $H^+$ ions which bend out of the cyclotron into the beam lines. The radial position of the stripper (R) can be adjusted to provide continuously variable energies from 180 up to 520 MeV. The stripper height can be varied to change the beam intensity up to 1 μA and 100 μA for polarized or unpolarized beam respectively. The unpolarized ion source is of the Ehlers type, giving 1-2 mA at 12 keV. The Lamb Shift polarized ion source is capable of giving 1 μA of 75-80% polarized beam at injection. The beam is bunched in packets 1 to 4 ns wide separated by 43 ns. The general layout of the TRIUMF facility is presented in figure 3.1.

## 3.2 The Beamline

### 3.2.1 The Beamline for E466

The neutrons were produced by a momentum-dispersed beam of protons in beam line 4B incident on a $^7$Li strip target of thickness 220 or 110 mg/cm$^2$ using the CHARGEX neutron-beam facility[42] at TRIUMF illustrated in Fig. 3.2. The energy spread of the neutron beam depended upon the proton-beam energy spread, energy loss by the protons in the $^7$Li target, and the separation of the ground and first excited state of the residual $^7$Be nucleus. Data were collected with $LH_2$ target cells either 1.5 or 6 cm thick. The deuterons from $np \rightarrow d\pi^0$ and the protons from $np \rightarrow pn$ were detected in the medium resolution spectrometer (MRS).

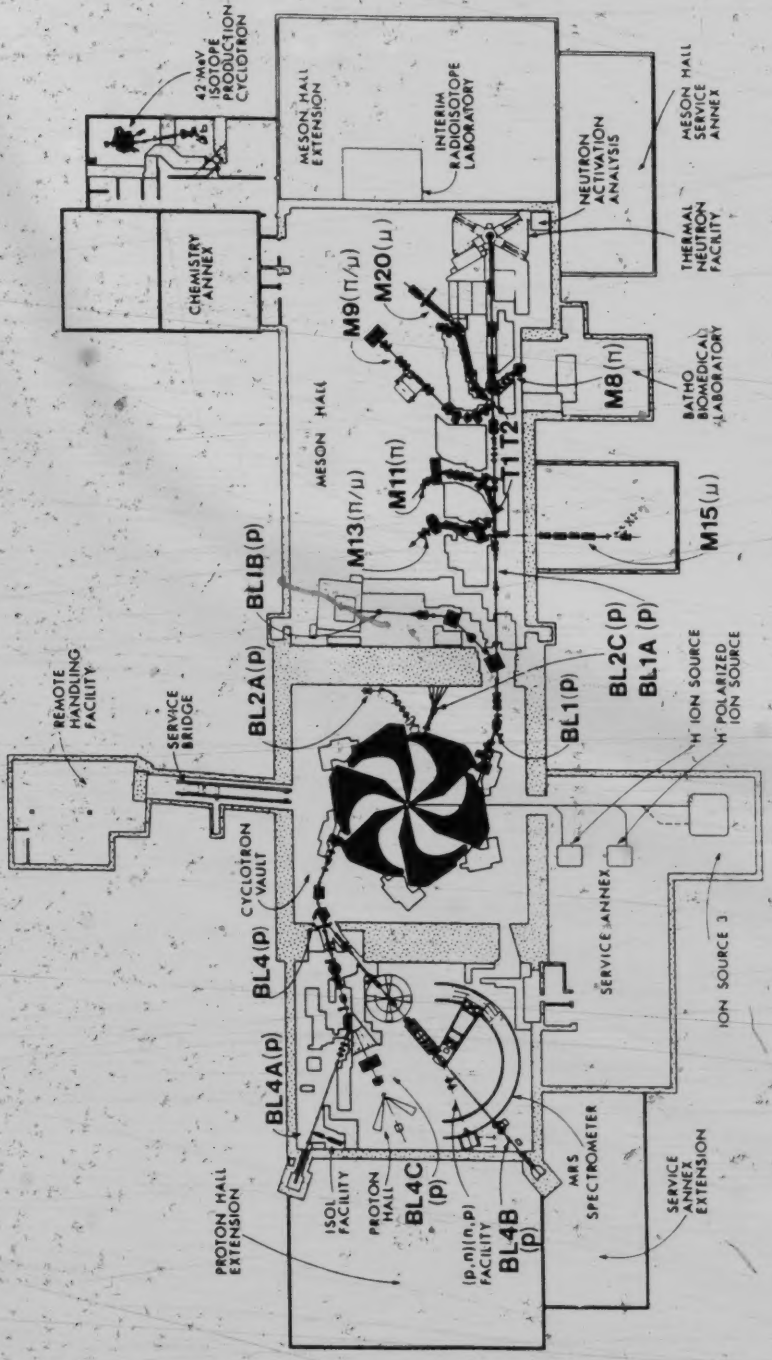


Figure 3.1 General layout of the TRIUMF facility.

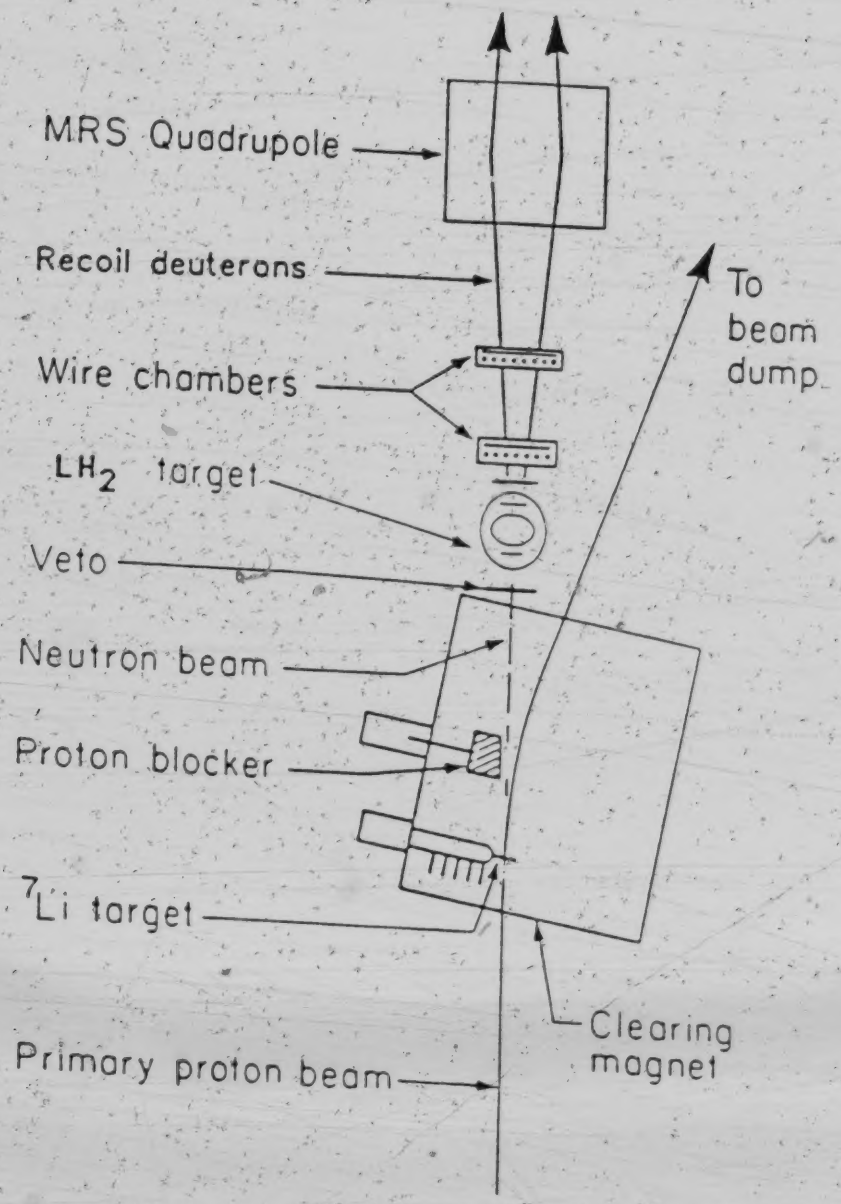


Fig. 3.2 Schematic view of the CHARGEX neutron-beam facility, liquid-hydrogen ($LH_2$) target.

### 3.2.2 The Beamline for E552

The proton beam transport system for E552, near the MRS, is shown in Fig. 3.3. A primary polarized proton beam on beamline 4B of about 1 nA was collimated in collimator #1 which had a 6 mm internal diameter (ID). About 50 pA of beam could reach the In-Beam polarimeter (IBP), enough to get a good measurement of beam polarization. The polarized beam was reduced a further factor of 300 (to ~ 160 fA intensity or $10^6$ Hz) by collimator #2 of 6 mm ID., so that protons incident on the target could be counted in scintillators. This was followed by an anti-scatter cleanup collimator A. Following the $LH_2$ target was a " micro-beamstop " of diameter 12 mm and length 63 mm intended to prevent the unscattered proton beam from entering the MRS.

The beam intensity was determined by scaling the coincidences between the upstream external trigger scintillator SETR (just in front of the $LH_2$ target ) and the internal trigger scintillator SITR of the $LH_2$ target (see Fig. 3.4).

The polarized proton beam, produced in a Lamb-shift ion source, emerged from the cyclotron polarized in the vertical direction with a polarization of about 75%. The polarization was reversed at the ion source, the usual cycle consisting of 3 minutes "spin up", 3 minutes "spin down" and 0.5 minute "spin off".

## 3.3 The $LH_2$ Target

A schematic diagram of the target and counter layout is shown in Fig. 3.4. Deuterons of the reaction $\vec{p}p \rightarrow d\pi^+$ were produced in the $LH_2$ target of thickness 1.5 cm along the beam direction. Two 0.25 mm thick plastic scintillators, SITR and SIRC, were added in the region of cold $H_2$ gas close to the $LH_2$ target cell itself. Timing and pulse height signals from these two scintillators were used to eliminate background events from the thicker external counters and the vacuum walls of the target. A signal from the front-end scintillator (FES) downstream of the target, SIRC, coupled with a signal from the upstream one SITR, allowed us to infer that any charged particles which originated inside

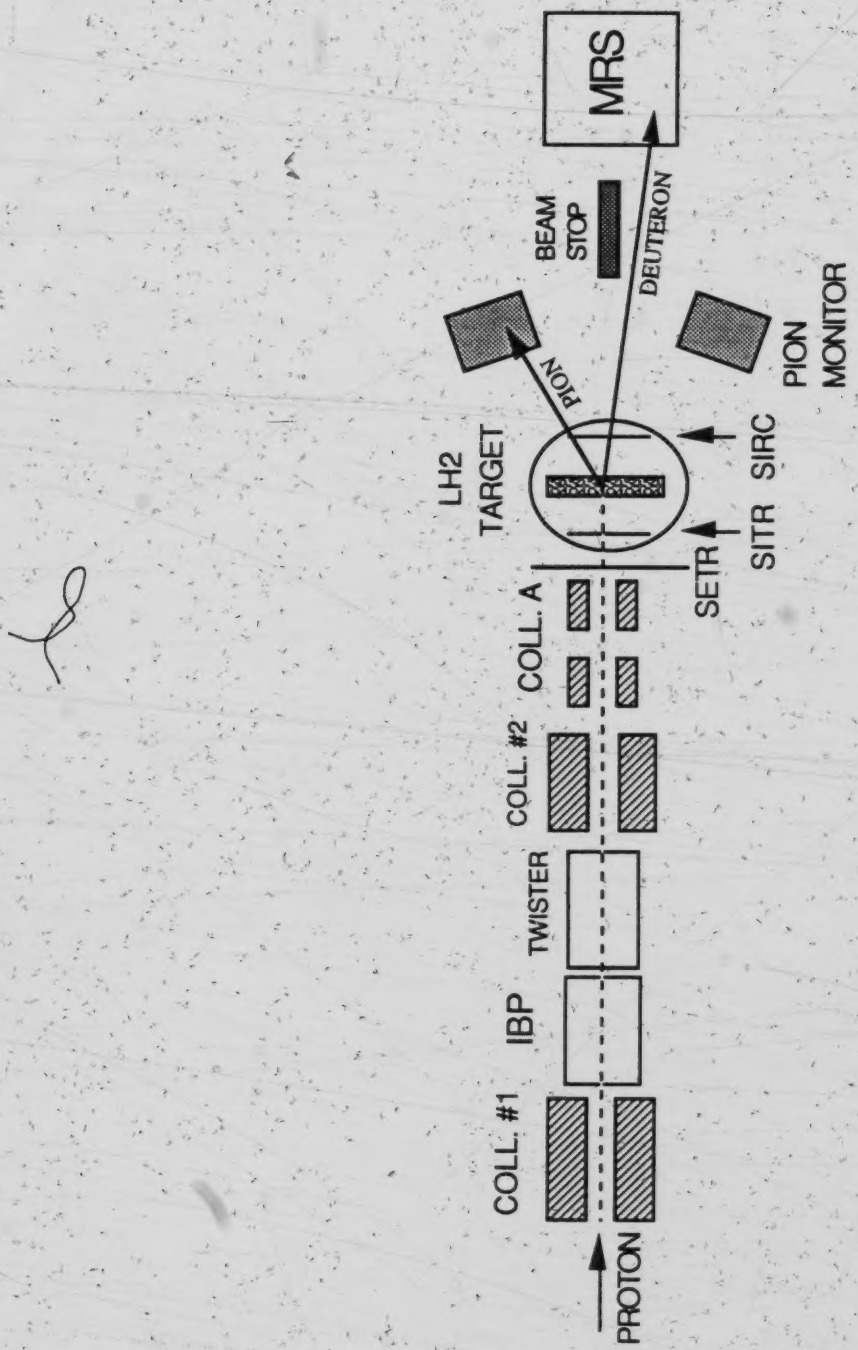


Figure 3.3 The proton beam transport system.

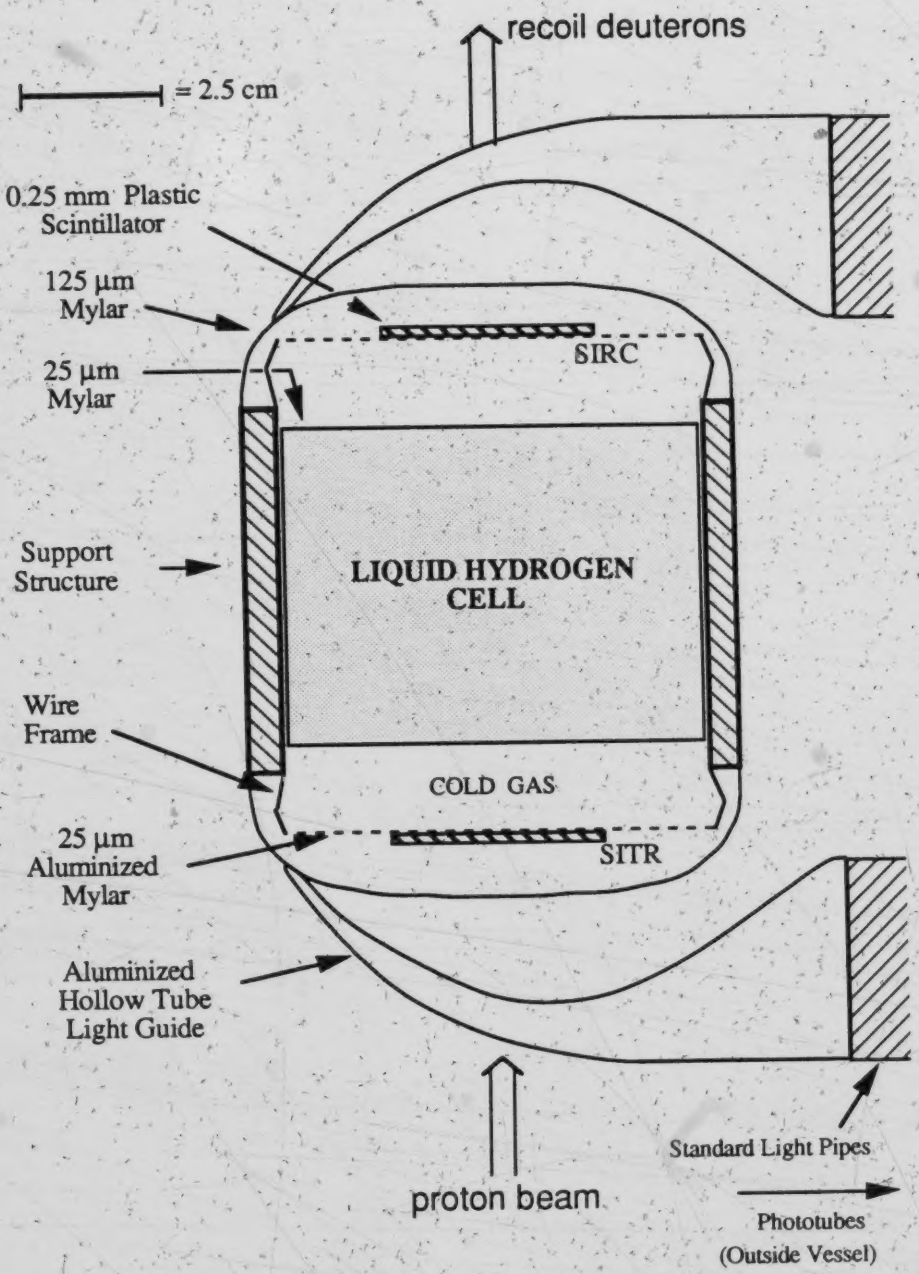


Figure 3.4 The liquid hydrogen target.

the $LH_2$ cell were from a proton induced reaction. Particles interacting with the support structure on either side were excluded by cuts placed on the particle trajectories as determined from two front end wire chambers FEC0 and FECM (see Fig. 3.5).

More details on the target can be found in Ref. 43.

## 3.4 Detection Apparatus

### 3.4.1 The Medium Resolution Spectrometer

A general layout of the MRS is presented in figure 3.5. This spectrometer is capable of momentum analyzing particles of up to 1.5 GeV/c with a resolution ($\Delta p/p$) of $2 \times 10^{-4}$. It consists of a quadrupole and a dipole magnet, with multiwire drift chambers to determine the angle and momentum of charged particles incident on the focal plane. The bend angle is 60° in the vertical plane. Solid angles depend upon running conditions, but are of order 0.5 to 2 msr. The momentum acceptance is about ±7%.

The front-end chambers (FECM and FEC0) provide good resolution in scattering angle ( $\leq$ 1 mr ), position ( $\leq$ 0.5 mm ), and redundancy in the target vertex reconstruction. They are standard 8 cm × 8 cm drift chambers, each consisting of four planes, two in each direction (horizontal (Y) and vertical (X)). Each plane contains sixteen wires of alternating anode and cathode wires. The FECs have operated with a flux of 2 MHz, and are limited only by the acceptable number of double tracks in the same beam burst.

The focal plane detection system consists of two vertical drift chambers (VDC) oriented at 45° to the beam direction in order to obtain a maximum resolution of 50 μm. Each 30 cm × 105 cm chamber contains two anode planes, the X and U planes, one to measure the bend plane coordinate and one slanted at 30° to measure the non-bend plane coordinate. The particle track reconstructed by the VDCs permits the computation of the focal plane crossing point, and hence of the momentum of the particle.

The Medium Resolution Spe ctrometer

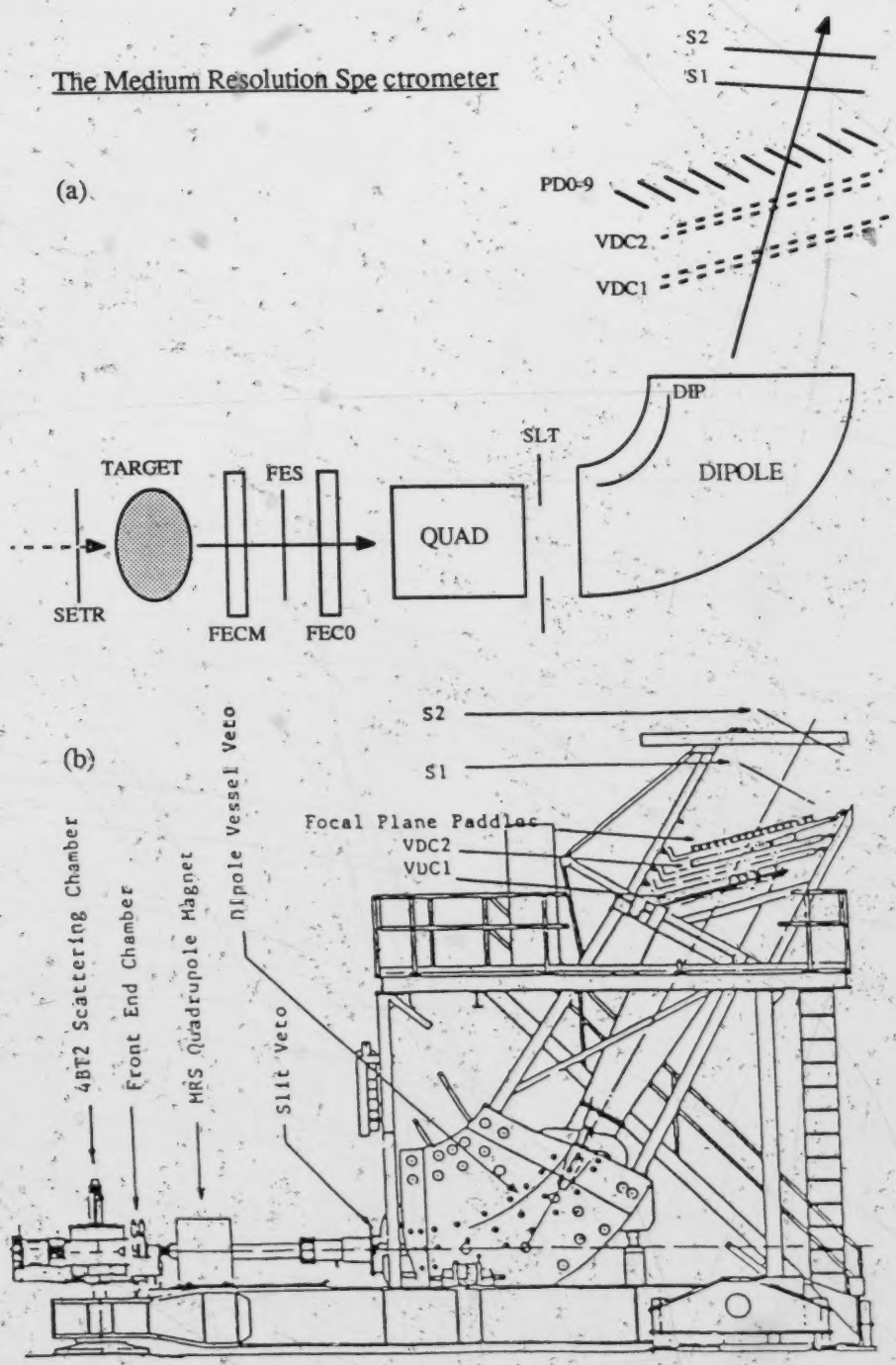


Figure 3.5 (a) Schematic diagram of the MRS.

(b) Scale picture of the MRS showing support structure.

A series of 10 segmented trigger plastic scintillators (paddles) located just above the VDC's are used in coincidence with the front end scintillator (FES) to provide a trigger condition. Any combination of the paddles may be used in the trigger thus limiting the amount of focal plane considered. More details on the MRS can be found in the MRS Operation Manual[44].

Near threshold the deuterons from the reaction $pp \rightarrow d\pi^+$ are confined to a small cone of angles in the laboratory forward direction. Fig. 3.6 illustrates the kinematic correlation between laboratory angle and deuteron momentum (the threshold energy of the reaction $pp \rightarrow d\pi^+$ is 287.51 MeV). Thus, close to threshold, we were able to measure a complete angular distribution at once by detecting the recoil deuterons with the MRS.

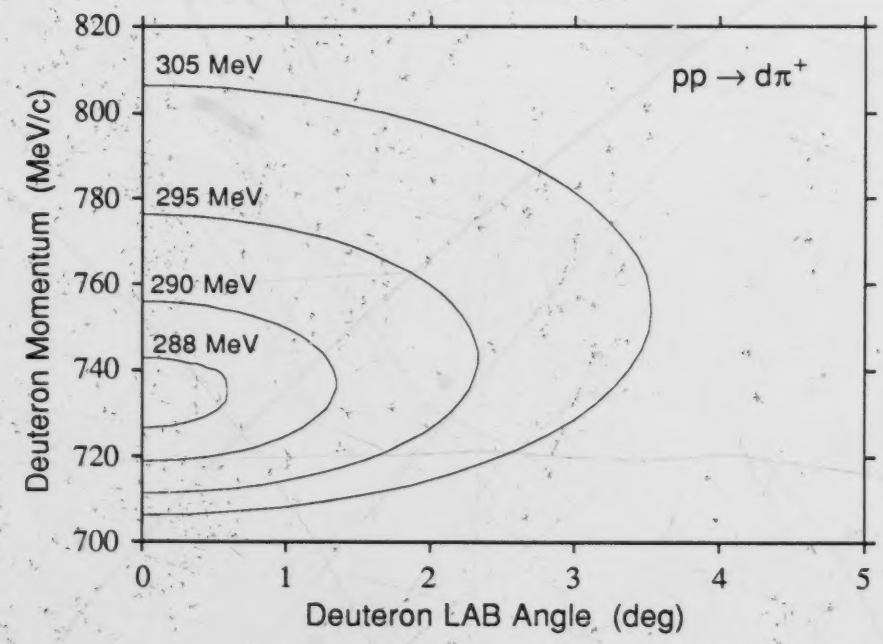


Figure 3.6 Correlation between laboratory reaction angle and deuteron momentum.

### 3.4.2 Pion Monitor

For any cross section measurement it is necessary to measure wire chamber efficiencies. Pion detectors of horizontal length 57 mm, vertical length 133 mm and thickness 32 mm were used to provider a sample of events in which a pion was definitely identified, and for which there must be a deuteron passing through the MRS. The dimensions of the detection apparatus is presented in Fig. 3.7.

## 3.5 In-Beam Polarimeter (IBP)

The IBP uses free p-p scattering from a polyethylene target to monitor both the beam polarization and beam current. The polarimeter layout is illustrated in Fig. 3.8. On either side of the beam line a pair of scintillators (L1.L2 or R1.R2) detect elastically scattered protons at 17°. Each of these telescopes is in coincidence with its recoil counter (L3 or R3, respectively). L3 and R3 are located at 70° on either side of the beam line, Triple prompt coincidences (L3.L2.L3 or R1.R2.R3) are counted. To measure the contribution of accidental events, coincidences between these same sets of detectors, but with L3 and R3 delayed by 43 nsec, are also counted. This delay ensures that the protons come from different beam bursts. The net number of events defined as

$$\text{net} = \text{L(real)} - \text{L(acc)} + \text{R(real)} - \text{R(acc)} \qquad (3.1)$$

should be proportional to the total integrated beam charge (beam flux). The polarization asymmetry is defined by

$$\varepsilon = \{[\text{L(real)} - \text{L(acc)}] - [\text{R(real)} - \text{R(acc)}]\} / \text{net} \; . \qquad (3.2)$$

The beam polarization is then given by

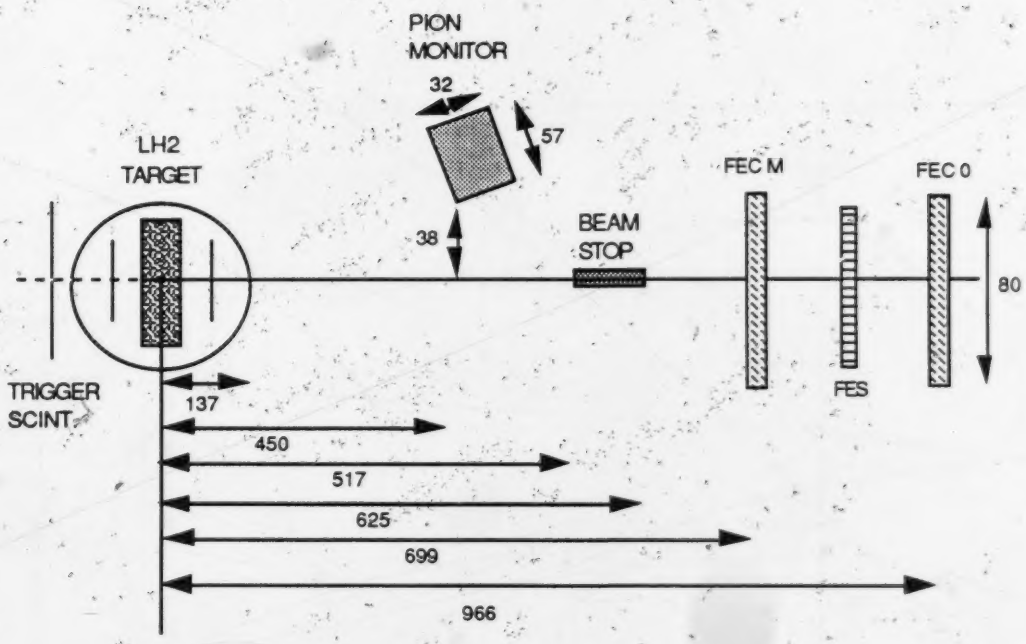


Figure 3.7 The layout of the detection apparatus. Distance units are in mm.

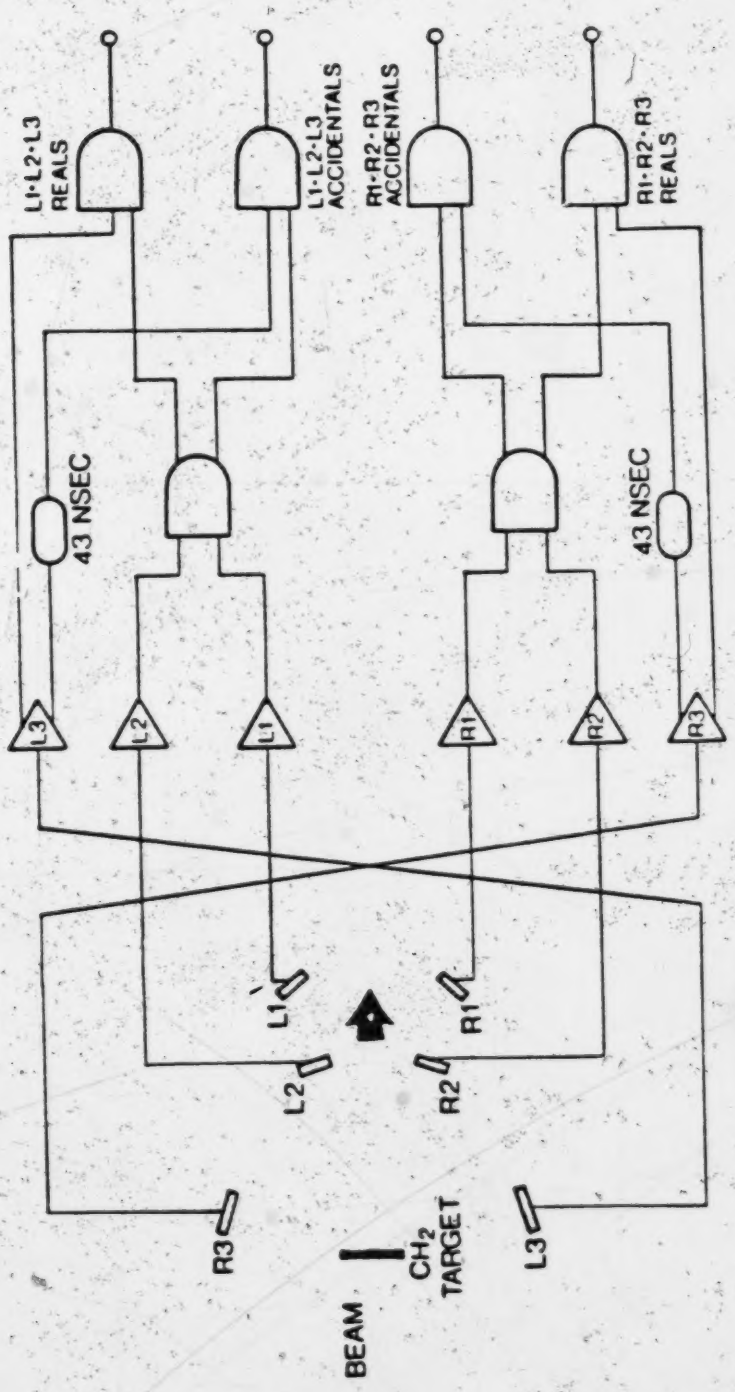


Figure 3.8 Schematic diagram of the In-Beam Polarimeter.

$$P_B = \frac{\varepsilon}{A_{CH_2}} \pm \frac{1}{A_{CH_2}} \sqrt{\frac{1 - \varepsilon^2}{net}} \qquad (3.3)$$

where $A_{CH_2}$ is the analyzing power observed using a polyethylene target. $A_{CH_2}$ depends on energy, and is determined empirically as a function of the analyzing power of H ($A_y(H)$) and beam energy

$$A_{CH_2} = A_y(H) [\ 1.0830 - (T_p/100)(0.07486 - (T_p/100)0.00823)\ ] \qquad (3.4)$$

where $T_p$ is the proton incident energy, and $A_y(H)$ is given by the phase shift analysis program SAID[45]. The corrections are due to prompt background from (p, 2p) reactions. The values of $A_{CH_2}$ are listed in table 3.1 for TRIUMF energies.

**Table** 3.1 Analyzing power of polyethylene.

| $T_p$ (MeV) | 200 | 250 | 300 | 350 | 400 | 450 | 500 |
|---|---|---|---|---|---|---|---|
| $A_{CH_2}$ | 0.283 | 0.327 | 0.370 | 0.414 | 0.433 | 0.449 | 0.466 |

We added a correction to Eq.(3.3) to account for the instrumental asymmetry of the IBP, which was monitored using an unpolarized beam. The beam polarization then became

$$P_B = [\ (P_B)_{polarized} - (P_B)_{unpolarized}\ ] \pm \sqrt{(\Delta P_B)^2_{polarized} + (\Delta P_B)^2_{unpolarized}} \qquad (3.5)$$

where $(P_B)_{unpolarized}$ was the false polarization of an unpolarized beam measured by the IPB. The beam polarization was measured for each run for both "spin up" and "spin down" states.

### 3.6 Data Collection

Data acquisition was handled by the CAMAC system and the TRIUMF VDACS

data acquisition system using a VAX 750 computer. A fast J-11 microprocessor controlled the transfer of data from the CAMAC modules to the VAX computer in a buffered mode which in turn recorded them on magnetic tape at 6250 bpi for further analysis. Using the data analysis program LISA program, a fraction of the events was analyzed on-line to monitor the quality of beam, data and scalers. More details can be found in the VDACS Data Acquisition and Analysis System[46].

The analyzing power for the reaction $pp \rightarrow d\pi^+$ was measured at 291 and 295 MeV. For each series of measurements the proton beam intensity was first reduced, the beam blocker taken out, and the MRS moved to 0° in order to determine the direction of the beam for each energy. The apparatus was then restored and the MRS was set to 0.73° (at 291 MeV) or 1.5° (at 295 MeV) for data collection. These angles matched the acceptance of the MRS to the size of the deuteron cone of angles. Following data collection, the MRS was moved to 3.5° to detect elastically scattered protons for calibration purposes.

### 3.7 Event Trigger and Data Stream

The electronics used with the MRS are mostly LeCroy CAMAC and NIM modules. The MRS trigger is illustrated in figure 3.9. A detailed description of the trigger and the meaning of the different variables indicated in the figure is given in the MRS manual[44]. Here a short description is given.

The main trigger may be 1-fold up to 6-fold depending on the values of the ECL (Emitter-Coupled Logical) variables: FETRIG, X1TR, PDMIN, PDMAX, FPP1, FPP2, and FPPOL. The values and meanings of these variables in this experiment are listed in table 3.2. Similarly, the Front End trigger may form up to a 4-fold coincidence and can be changed from a Boolean AND to an OR function. A typical signal might evoke the following path in the electronics system: 1) signals from the FEC X0 or Y0 planes produce an FETRIG signal which has a given delay and width specified by the TRMIN and TRMAX variables; 2) this FETRIG pulse is ANDed with signals from the trigger paddles,

VDC X1 plane, and S1 scintillator which then sets the latch (the latch blocks any other signals from altering the TDC's or ADC's): 3) the TDC's and ADC's are gated and started to digitize the signals; 4) the prescale counter allows only a subset of triggers through and these are ORed with a selectable combination of Slow Auxiliary triggers; 5) if the ORed signal is NOT present then a fast clear is generated, otherwise the computer reads the TDC's and ADC's; 6) the latch is cleared in any case.

The VAX 750 computer reads the data from the CAMAC ADC's and TDC's in the order specified by the TWOTRAN[47] file created by the user for VDACS. The data stream (event structure) in this experiment is described in table 3.3.

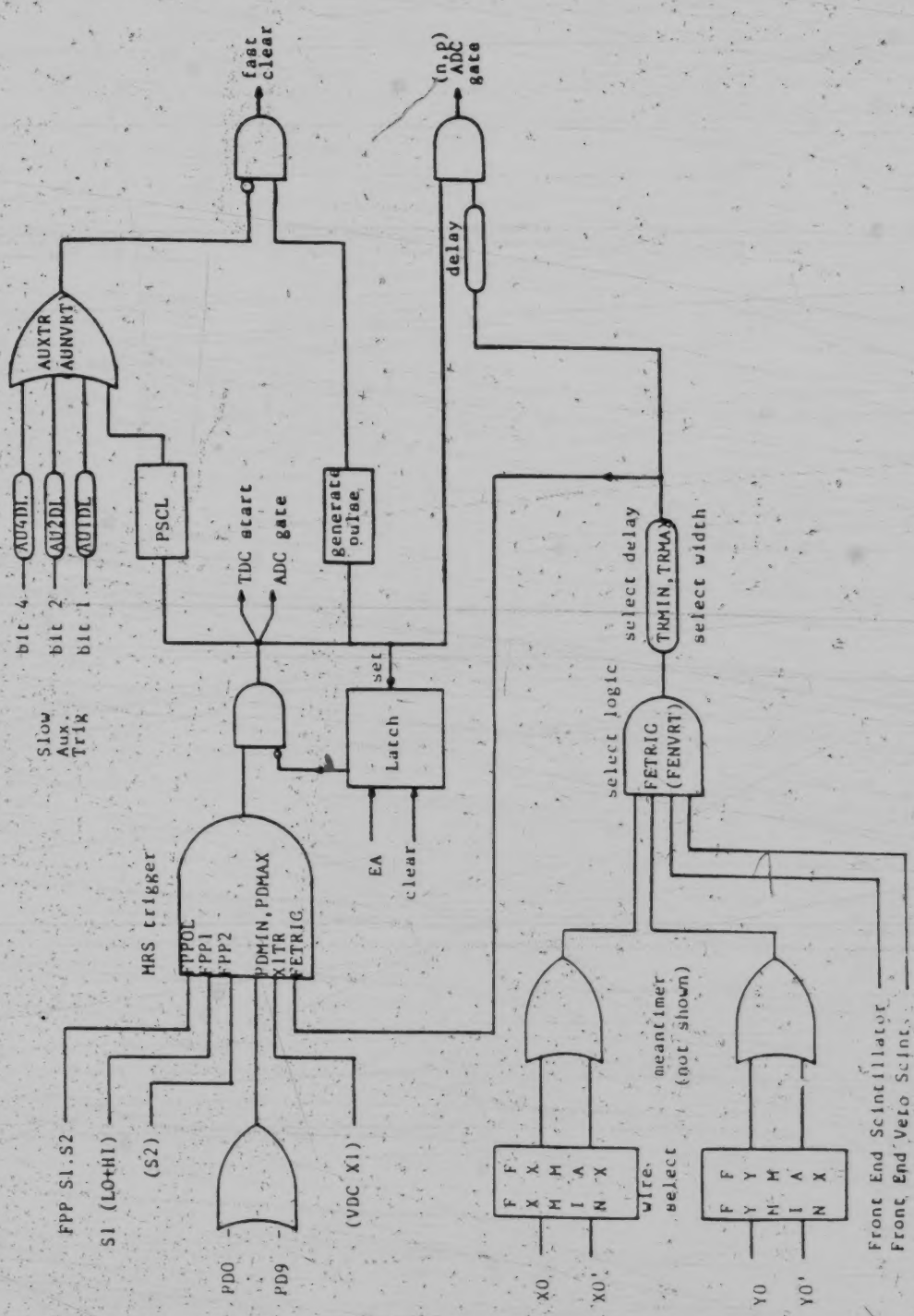


Figure 3.9 Schematic of the MRS Trigger.

**Table** 3.2 The Values of the ECL Parameters

| Variable | Value | Action |
|---|---|---|
| FXMIN | 0 | Define vertical acceptance of the Front |
| FXMAX | 1400 | End Chamber |
| FYMIN | 0 | Define horizontal acceptance of the |
| FYMAX | 1600 | Front End Chamber |
| PDMIN | 0 | Define Top End scintillators in the Trigger |
| PDMAX | 9 | can be affected by XFMIN, XFMAX |
| FPPOL | 0 | Non-zero to include Focal Plane Polarimeter |
| FPP1 | 1 | Non-zero to include S1 scintillator |
| FPP2 | 1 | Non-zero to include S2 scintillator |
| X1TR | 1 | Non-zero to include X1 plane |
| FETRIG | -6 | Control Front End Trigger |
| FENVRT | 0 | Invert Front End Signals |
| AUXTR | -6 | Slow Auxiliary trigger |
| AUNVRT | 6 | Invert Aux Trigger Signals |
| AU1DL | 0 | Delays in ns for Aux Trigger Signals |
| AU2DL | -86 | |
| AU4DL | -48 | |
| TRMIN | 99 | Top-bottom resolving time in ns |
| TRMAX | 124 | |
| TMAX | 12 | Max VDC time in ns |
| PSCL | 0 | Prescale value ( 0 - 4095 ) |
| THRSH | 30 | Discriminator threshold in mv |
| RFDEL | 0 | Delay for RF signal |
| XFMIN | 10000 | Select region of Focal Plane |
| XFMAX | 32767 | can affect PDMIN,PDMAX as well |

**Table** 3.3 The description of the event structure.

| Event Word No. | Description |
|---|---|
| 1 - 5 | Five header words describing the event type, length, and sequence number |
| 6 - 7 | Two signals from the Digital Coincidence Register (DCR) |
| 8 - 16 | Eight trigger scintillator timing signals (TTB, TRF, SPARE1, SPARE2, TS1, TS2, TFES, and TETR ) and a header word |
| 17 - 29 | 12 scintillator ADC signals (EDIF, ESLT, EPD0, ·····, EPD9 where SLT and DIP are the slit and dipole veto scintillators) and a header word |
| 30 - 33 | Three scintillator ADC signals (ES1H, ES1L, ES2) and a header word |
| 34 - 40 | 6 scintillator ADC signals (EFES, EETR, EITR, EIRC, EMNL (the left pion monitor), and EMNR (the right pion monitor)) and a header word |
| 41 - 45 | Four TDC signals (TITR, TIRC, TMNL, and TMNR) and a header word |
| 46 - ? | a VDC header word and a variable number of TDC values for all VDC wires which were struck |

# Chapter 4 Data Analysis

## 4.1 The LISA Data Analysis Program

Data analysis for this experiment was carried out on the VAX cluster at the University of Alberta. The LISA data analysis program was used to analyze the raw data supplied from magnetic tapes in the form of TDC, ADC, and scaler information.

The LISA program follows the path shown below for each event encountered

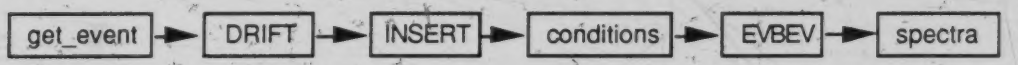


The subroutines labelled 'get_event', 'conditions', and 'spectra' are standard LISA routines, invisible to the user. The drift times for the delay wire chambers and ADC information is converted by the DRIFT routine (specific to the MRS experiments) into wire plane positions for each wire plane. The INSERT and EVBEV subroutines are written by the user. The INSERT routine uses the raw wire plane coordinates and calculates a set of secondary variables. Included in these are the traced-back positions on target (XI and YI), the scattering angle in the horizontal ($\theta_y$) and vertical planes ($\theta_x$), the azimuthal angle ($\phi$), and the focal plane position (XF) which is directly proportional to the momentum of the scattered particle. The EVBEV subroutine has access to the results of the conditions, and can do more calculations based on them. During the processing of each event, the spectra of the raw and calculated variables are histogrammed depending on the outcome of the conditions.

For further description of the LISA data analysis program the reader is referred to the LISA documentation manual[48,49].

## 4.2 Definition of Measured Observables

In general, the measured differential cross section is given by

$$\left(\frac{d\sigma}{d\Omega}\right)_0 = \frac{n}{LT \cdot \varepsilon_{MRS} \cdot d\Omega \cdot T_{tgt} \cdot F}, \qquad (4.1)$$

where n is the number of counts in the region of interest in the focal plane spectrum, LT is the computer live time during data taking which is calculated as the ratio of the number of pulser events recorded by the computer to the number presented to it, $\varepsilon_{MRS}$ is the overall MRS efficiency, $T_{tgt}$ is the target thickness in nuclei per unit area, and F is the incident beam flux which is determined from the IBP (see Eq. (3.1)).

When a polarized beam is used, the polarized differential cross section depends on the beam polarization P, the reaction analyzing power $A_y$, and the unpolarized differential cross section $(d\sigma/d\Omega)_0$

$$\left(\frac{d\sigma}{d\Omega}\right)(\theta,\phi) = \left(\frac{d\sigma}{d\Omega}\right)_0(\theta)\,(\,1 + \vec{P}\cdot\hat{n}\,A_y(\theta)\,), \qquad (4.2)$$

where $\theta$ is the scattering angle defined by $\cos\theta = \vec{k}_{in}\cdot\vec{k}_{out}$ and $\phi$ is the azimuthal angle between the polarization and the unit vector normal to the scattering plane, i.e. $\vec{P}\cdot\hat{n} = P\cos\phi$, provided that $\vec{P} = P\,\hat{X}_{MRS}$, $\hat{n} = \vec{k}_{in}\times\vec{k}_{out}/|\vec{k}_{in}\times\vec{k}_{out}|$, and $\hat{s} = \hat{n}\times\vec{k}_{in}/|\hat{n}\times\vec{k}_{in}|$, where $\vec{k}_{in}$ and $\vec{k}_{out}$ are unit vectors along the direction of the incident and outgoing particle momenta respectively (see fig. 4.1). Eq. (4.2) can then be rewritten as

$$\left(\frac{d\sigma}{d\Omega}\right)(\theta,\phi) = \left(\frac{d\sigma}{d\Omega}\right)_0(\theta)\,(\,1 + P\,A_y(\theta)\cos\phi\,). \qquad (4.3)$$

Actually, we did not measure the unpolarized cross section directly. Instead, we measured the polarized cross sections for both spin up and spin down polarization states. The spin up and down differential cross sections are given accordingly by

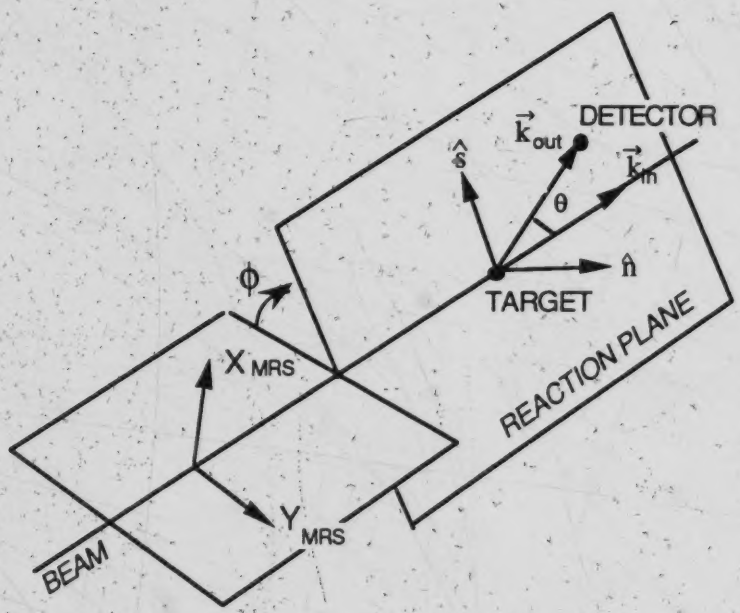


Figure 4.1 Definition of azimuthal angle.

$$\left(\frac{d\sigma}{d\Omega}\right)^{\uparrow}(\theta,\phi) = \left(\frac{d\sigma}{d\Omega}\right)_0(\theta)(\,1 + P^{\uparrow}\,A_y(\theta)\cos\phi\,) \tag{4.4}$$

$$\left(\frac{d\sigma}{d\Omega}\right)^{\downarrow}(\theta,\phi) = \left(\frac{d\sigma}{d\Omega}\right)_0(\theta)(\,1 - P^{\downarrow}\,A_y(\theta)\cos\phi\,) \tag{4.5}$$

where the superscript arrow represents the spin direction.

One can solve eqs (4.4) and (4.5), for the unpolarized differential cross section and analyzing power as follows

$$\left(\frac{d\sigma}{d\Omega}\right)_0 = \frac{P^{\downarrow}\left(\frac{d\sigma}{d\Omega}\right)^{\uparrow}(\theta,\phi) + P^{\uparrow}\left(\frac{d\sigma}{d\Omega}\right)^{\downarrow}(\theta,\phi)}{P^{\downarrow} + P^{\uparrow}} \tag{4.6}$$

$$A_y = \frac{\left(\frac{d\sigma}{d\Omega}\right)^{\uparrow}(\theta,\phi) - \left(\frac{d\sigma}{d\Omega}\right)^{\downarrow}(\theta,\phi)}{P^{\downarrow}\left(\frac{d\sigma}{d\Omega}\right)^{\uparrow}(\theta,\phi) + P^{\uparrow}\left(\frac{d\sigma}{d\Omega}\right)^{\downarrow}(\theta,\phi)} \frac{1}{\cos\phi} \tag{4.7}$$

## 4.3. Event Selection

In the off-line analysis the recorded events were required to meet the following conditions before further processing:

1) A 'good-hit' condition wherein whenever a 'multiple hit' or a 'missing hit' was identified in any of the wire-chamber planes X1, X2, X0, Y0, XM, or YM (see Sec. 3.4.1.), the event was rejected. Note that this rejection introduces an overall wire-chamber detection inefficiency, however, it does not affect our results of analyzing powers since it influences spin-up and spin-down data equally.

2) A cut on the energy spectrum of scintillator SETR just in front of the $LH_2$ target to reject events due to charged incident particles for $np \rightarrow d\pi^0$, or to select only events due to protons for $pp \rightarrow d\pi^+$.

3) Cuts on the energy spectra of scintillators SITR and SIRC inside the $LH_2$ target assembly in order to include only those particles which were created inside the $LH_2$ target.

4) ESUM is the maximum energy lost by the particle in any of the trigger paddles and TTB ( Time Top-Bottom) is the time of flight of the particle from the FES to the paddles. The pulse height of a scintillator signal is proportional to $(ZE/P)^2$, where Z, P and E are the charge, momentum and energy of the particle, respectively. On the other hand, the time of flight is proportional to $(E/P)^{-1}$. Therefore, a two-dimensional spectrum (usually called SPID) of ESUM vs TTB was used to identify particles with different masses and charges. Fig. 4.2 shows a typical SPID spectrum at $T_p$ = 295 MeV in E552. The peak on the right of that of deuterons from $p(p,d)\pi^+$ corresponds to protons from $p(p,\bar{p})p$. Note that most of the elastic-proton events were actually eliminated in hardware via TOF cuts (see TFMIN and TFMAX in Table 3.2). The peak below the deuteron peak corresponds to accidental events where the TOF TDC was started by a proton from one beam burst and stopped by another proton from the previous beam burst (43 ns earlier).

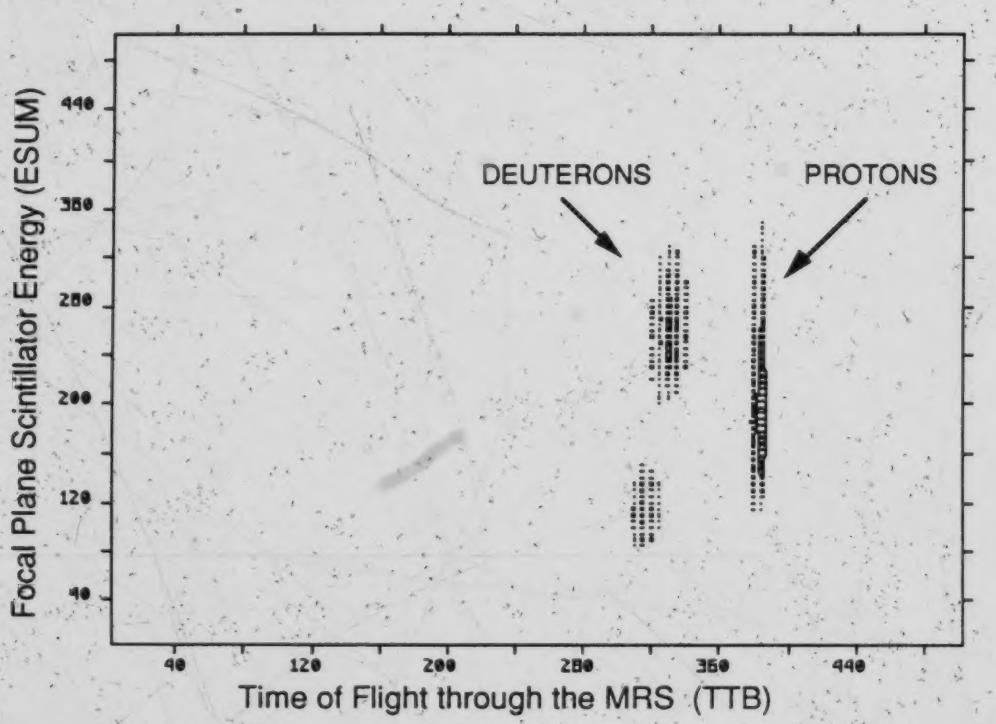


Fig. 4.2 The spectrum for particle identification.

## 4.4 Determination of the Particle Track

### 4.4.1 The Scattering Angle

Because of the limitation of the acceptance of the MRS, we had to move the MRS to a small non-zero angle ($\theta_{MRS}$) to cover as much of the cone of the deuteron angles as possible. Since the scattering angle $\theta$ was very small, we used (refer to Fig. 4.3)

$$\theta_x \equiv \tan\theta_x = \frac{X0 - XM}{FEC0 - FECM} \tag{4.8}$$

in the vertical plane and

$$\theta_y \equiv \tan\theta_y = \frac{Y0 - YM}{FEC0 - FECM} - \theta_{MRS} \tag{4.9}$$

in the horizontal plane. The MRS was always moved towards the negative direction in the horizontal plane. Although it is not conventional that the horizontal direction is defined as the Y axis for the MRS, it corresponds to the non-bend coordinate of the spectrometer.

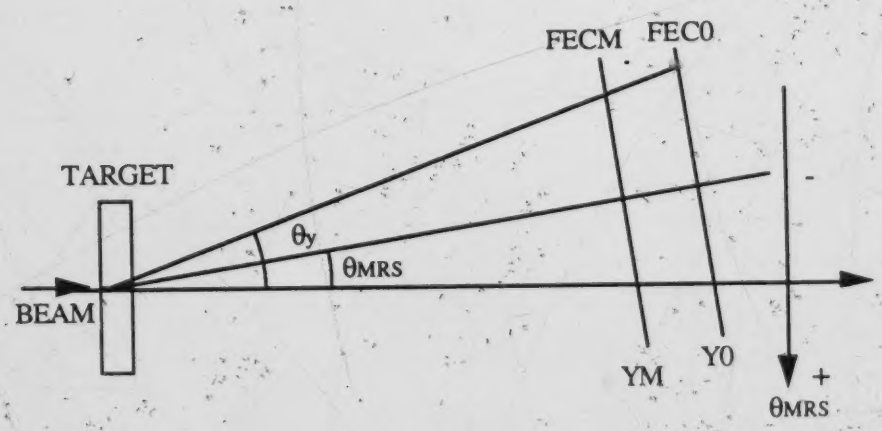


Figure 4.3 Calculation of the scattering angle.

The actual plane scattering angles were then given by

$$\theta_{xc} = \theta_x - \theta_{x0} \tag{4.10}$$

$$\theta_{yc} = \theta_y - \theta_{y0} \tag{4.11}$$

where $\theta_{x0}$ and $\theta_{y0}$ define the direction of the incident beam as determined by the "zero-degree" runs (see sec.3.2 and 3.6). Therefore the scattering angle became

$$\theta = \sqrt{\theta_{xc}^{\,2} + \theta_{yc}^{\,2}} \tag{4.12}$$

### 4.4.2 The Azimuthal angle

The azimuthal angle $\phi$ is given by

$$\tan\phi = -\frac{\theta_x}{\theta_y} \tag{4.13}$$

where the minus sign comes from the definition of the azimuthal angle $\phi$ as shown in figures 4.4 and 4.1.

## 4.5 Determination of Momentum

The position of the scattered particle on the focal plane was calculated with the VDC information (see figure 4.5)

$$XF = \frac{G\,(X1 + H) - F\,(X1 + H - X2)}{G - (X1 + H - X2)\tan\delta} \tag{4.14}$$

where $\delta$ is quite small and may be neglected. $\theta_{pc} \equiv (X1 + H - X2) / G$ for small deviation from 45°. F is a constant which defines the MRS focal plane position relative to the wire planes in the two VDCs. Errors in F show up as a variation in the calculated position XF with $\theta_{pc}$ via the relation $\Delta XF = \Delta F \cdot \theta_{pc}$.

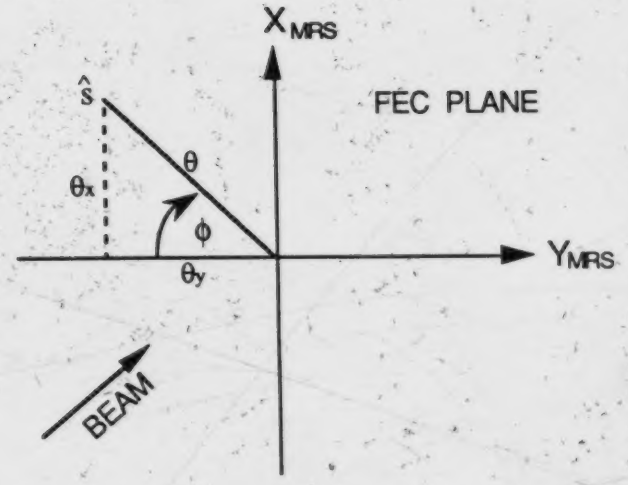


Figure 4.4 Calculation of azimuthal angle.

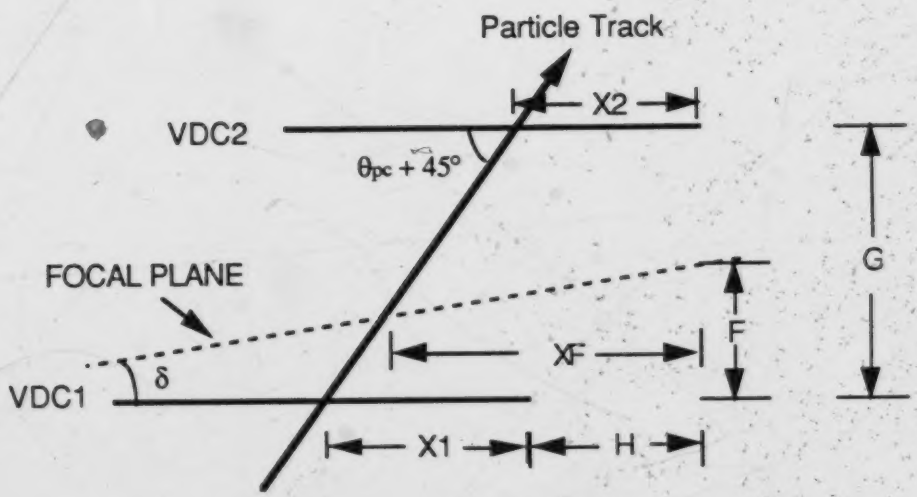


Figure 4.5 The geometry of the MRS focal plane.

The optical properties of the MRS dipole/quadrupole combination give rise to the second source of the variation of focal plane position for particles of equal momenta. The MRS quadrupole acts only to focus the rays diverging in the non-bend plane into the dipole magnet gap (while actually causing the bend plane rays to diverge), but the dipole focuses in the bend plane by means of a technique known as 'edge focusing'. Edge focusing is achieved by angling the exit and exit edges of the dipole magnets to create different path lengths, and therefore different degrees of bending, for particles entering the dipole at different points . This lens action of the dipole gives the system an overall magnification, or variation of XF with XI (bend plane offset at the $LH_2$ target), of 0.5.

Both effects were corrected empirically by plotting 2D histograms, $\theta_{pc}$ vs. XF and XI vs. XF, and adjusting the observed focal plane position in such a way that the corrected XF (called XFK) was independent of $\theta_{pc}$ and XI. Linear and quadratic corrections were made, although the quadratic corrections were relatively small.

No significant variation of focal plane position with the non-bend coordinate, YI, was observed when YI was plotted versus XFK.

A quadratic relation between focal plane position (XF) and momentum (P) had been found empirically,

$$P = 81.50 \times B \times \left[ 1 - \frac{XF - 15000}{111430} \times \left( 1 - \frac{XF - 15000}{376289} \right) \right] \qquad (4.15)$$

where B is the magnetic field strength of the MRS dipole in units of KG, and P is in units of MeV/c, and XF is the channel number in the XF spectrum.

Figure 4.6 illustrates the correlations between laboratory angle and momentum of the deuterons for 290.7 and 294.9 MeV proton beams. The deuterons underwent multiple scattering and differential energy loss in the $LH_2$ target, causing the locus of $pp \rightarrow d\pi^+$ events to be broadened and shifted compared to the ideal case of a "thin" target. Figure 4.7 illustrates the correlation between laboratory angle and momenta of the deuterons from $p(n,d)\pi^0$ and protons from p(n,p)p for a 278 MeV neutron beam in E466. Momentum is shown as a fractional difference from the central momentum p = 735 MeV/c.

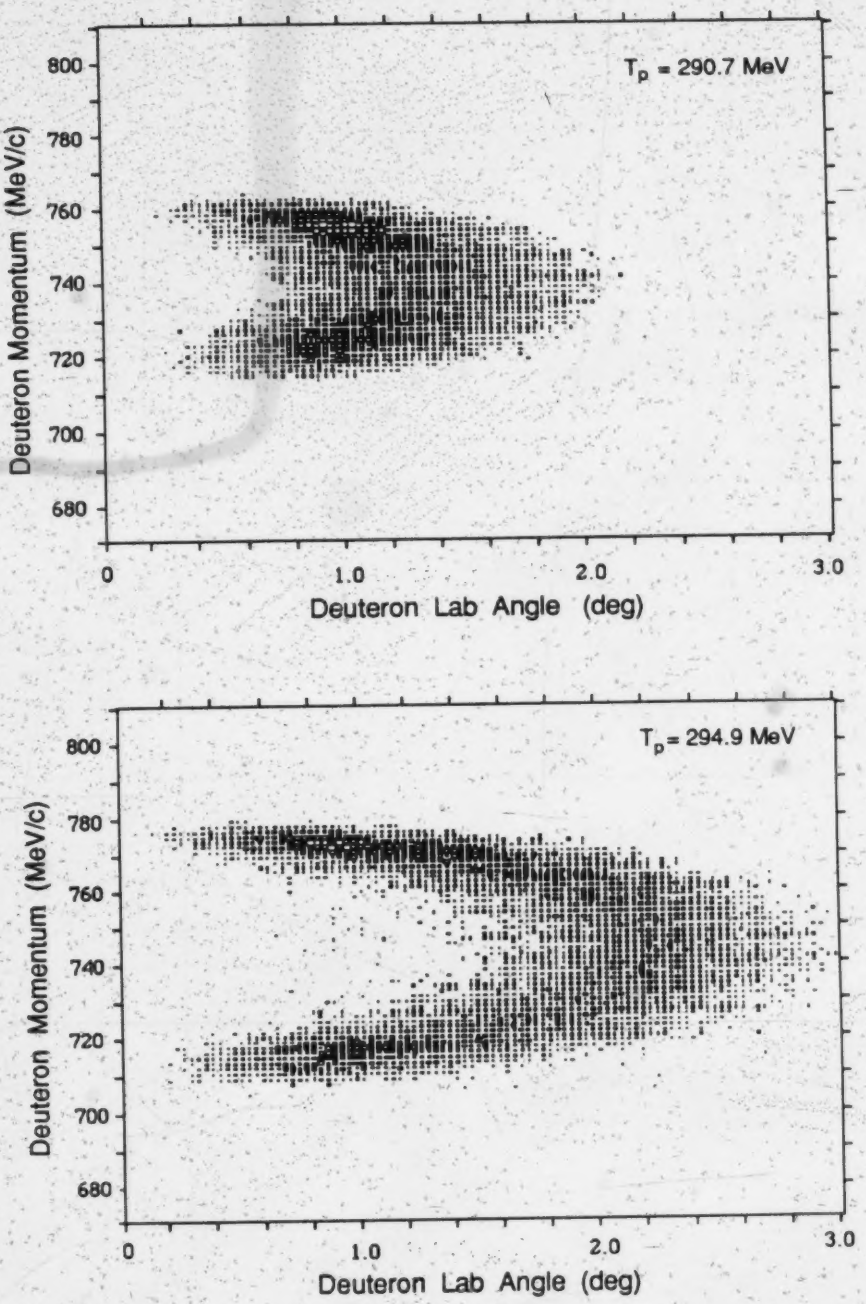


Fig. 4.6 Correlation between the lab reaction angle and momentum for deuteron at nominal proton-beam energies of 290.7 and 294.9 MeV. The plotted momenta have been corrected for energy losses through the system.

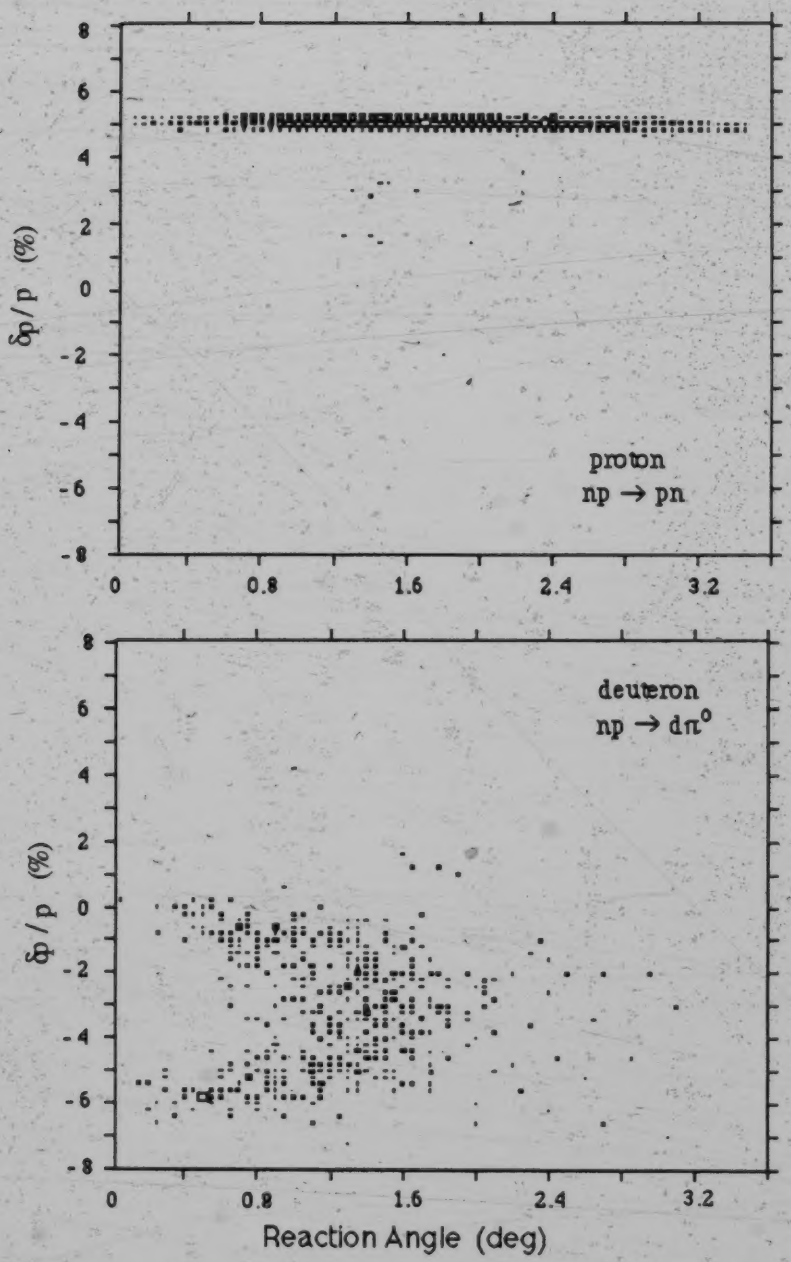


Fig. 4.7 Correlation between lab reaction angle and momenta for the protons and deuterons in E466.

## 4.6 The Determination of Beam Energies

The momentum of a deuteron entering the MRS quadrupole was determined using Eq. (4.15). This was then corrected for average momentum loss from the center of target to the quadrupole to determine the deuteron momentum at the center of target. With the momentum and scattering angle determined the beam energy was calculated by using the two-body kinematic relation of the reaction $pp \rightarrow d\pi^+$ on an event-by-event basis.

Figures 4.8 and 4.9 illustrate the beam energy distributions for the "290.7" and "295.9 MeV" runs. Using a Gaussian distribution fit, we have determined that the energies were 290.7 ± 1.2 Mev and 294.9 ± 1.3 MeV (centroid ± σ) respectively. The Gaussian fit is not very good at energies below the main peak for the 294.9 MeV beam distribution because the deuteron energy loss follows Vavilov distribution, not a Gaussian distribution (see appendix I). In Fig. 4.8, the 290.7 MeV beam distribution looks like Gaussian distribution because the beam energy calculated cannot go down below threshold (287.5 MeV) due to the two-body kinematics.

## 4.7 General Formalism of Data Analysis

### 4.7.1 Formalism of Data Analysis for E466

The $NN \rightarrow d\pi$ angular distributions near threshold follow the expectations from s- and p-wave dominance. The s-wave cross-section is isotropic, while the summed s- and p-wave cross-section has a characteristic $A + B\cos^2\theta$ behavior. It is convenient to expand $d\sigma/d\Omega$ in Legendre polynomials

$$4\pi \frac{d\sigma}{d\Omega}(np \rightarrow d\pi^0) = A_0 P_0(\cos\theta) + A_2 P_2(\cos\theta) \qquad (4.16)$$

The total cross section is then

$$\sigma_T(np \rightarrow d\pi^0) = \int d\Omega \frac{d\sigma}{d\Omega}(np \rightarrow d\pi^0) = A_0, \qquad (4.17)$$

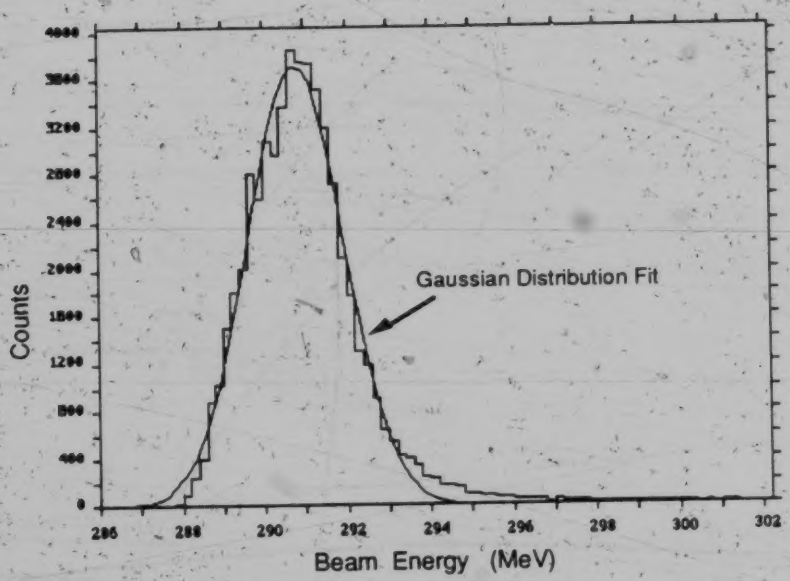


Figure 4.8 Beam energy distribution for the 290.7 MeV.

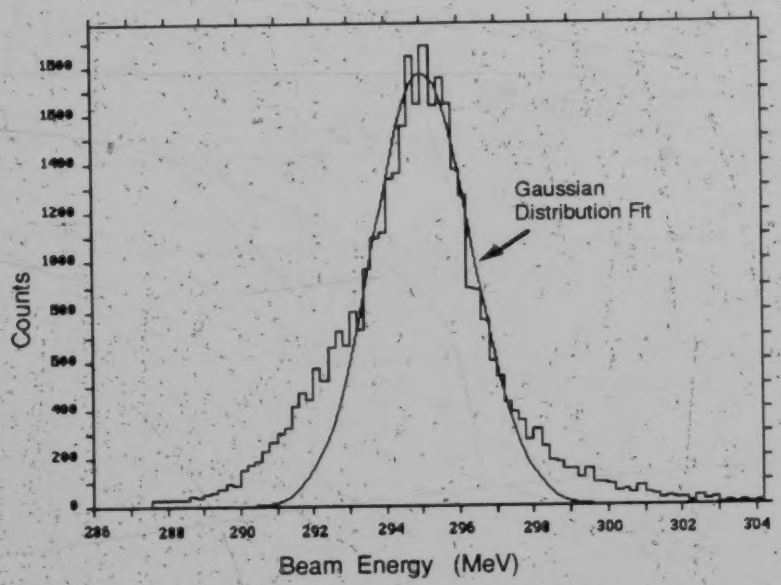


Figure 4.9. Beam Energy Distribution for the 294.9 MeV.

where θ is the angle between an outgoing deuteron and the incoming neutron in the center-of-mass system. The cross section normalization was provided by protons from the $np \rightarrow pn$ reaction, which were accumulated at the same time as the deuterons. For the $np \rightarrow pn$ cross section normalization the predictions of Arndt's SP88 phase shift analysis[45] were used. It was parametrized as

$$\frac{d\sigma}{d\Omega_{cm}} = [11.55 + (295 - T_n)/40] \times \left[1 - T_n\theta_p^2 / 118000\right] \text{ mb/sr} \qquad (4.18)$$

where $T_n$ is the beam energy in MeV and $\theta_p$ the c.m. proton angle in degrees. The $np \rightarrow pn$ proton momenta were several percent higher than for any of the deuterons (see Fig. 4.7), and one of the chief concerns of the experiment was to map the MRS acceptance as a function of momentum in order to relate the ratio of counts (deuteron / protons) to the ration of cross sections [$(np \rightarrow d\pi^0)$ / $(np \rightarrow pn)$]. Using a $\chi^2$ method, the proton and deuteron data were fitted simultaneously. More details about the fitting method are given in Ref. 9.

### 4.7.2 Formalism of Data Analysis for E552

After the scattering of spin 1/2 particle with polarization $\vec{P} = P\,\hat{X}_{MRS}$ from a target, the observed angular distribution is given by[50]

$$I(\theta,\phi) = C\left(\frac{d\sigma}{d\Omega}\right)_0(\theta)\left[1 + \varepsilon(\theta)\cos\phi\right]\Phi(\theta,\phi) \qquad (4.19)$$

where θ and φ are the polar scattering angle and azimuthal angle, and $\Phi(\theta,\phi)$ is the differential acceptance of the apparatus, and C an overall normalization constant, and ε is the left-right asymmetry to be determined.

We are interested in the statistical estimator for the asymmetry for a given scattering

angle. The observed azimuthal distribution for a given scattering angle is

$$f(\phi) = \frac{1}{2\pi}(1 + \varepsilon \cos\phi)\,\Phi(\phi)\,. \tag{4.20}$$

If the effective acceptance has a symmetry period of 180° in $\phi$

$$\Phi(\phi) = \Phi(\phi + \pi)\,, \tag{4.21}$$

it can be be shown that

$$\int_0^{2\pi} f(\phi)\cos\phi\, d\phi = \varepsilon \int_0^{2\pi} f(\phi)\cos^2\phi\, d\phi\,, \tag{4.22}$$

since for n+m odd

$$\int_0^{2\pi} \Phi(\phi)\sin^m\phi\cos^n\phi\, d\phi = 0\,. \tag{4.23}$$

If we estimate the integrals in Eq. (4.22) by sums over the observed events, we have

$$\varepsilon = \sum_{ev}\cos\phi \Big/ \sum_{ev}\cos^2\phi\,. \tag{4.24}$$

In order to satisfy the condition $\Phi(\phi) = \Phi(\phi + \pi)$ we can reverse the beam polarization. The azimuthal distributions are

$$f^{\uparrow}(\phi) = \frac{1}{2\pi}(1 + \varepsilon\cos\phi)\,\Phi(\phi) \tag{4.25}$$

for spin up and

$$f^{\downarrow}(\phi) = \frac{1}{2\pi}(1 - \varepsilon \cos\phi)\,\Phi(\phi) \tag{4.26}$$

for spin down.

For the symmetric azimuthal angle $\phi' = \phi + \pi$, the distribution for spin down becomes

$$f^{\downarrow}(\phi + \pi) = \frac{1}{2\pi}(1 + \varepsilon \cos\phi)\,\Phi(\phi + \pi)\,. \tag{4.27}$$

Now, let

$$f'(\phi) = f^{\uparrow}(\phi) + f^{\downarrow}(\phi + \pi) \tag{4.28}$$

$$\Phi'(\phi) = \Phi(\phi) + \Phi(\phi + \pi)\,. \tag{4.29}$$

Then

$$f'(\phi) = \frac{1}{2\pi}(1 + \varepsilon \cos\phi)\,\Phi'(\phi) \tag{4.30}$$

where $\Phi'(\phi)$ now satisfies the condition (4.21). Using Eq. (4.24), we have

$$\begin{aligned}
\varepsilon(\theta_{cm}) &= \sum_{event} \cos\phi \,/\, \sum_{event} \cos^2\phi \\
&= \frac{\sum_{event}^{\uparrow} \cos\phi + \sum_{event}^{\downarrow} \cos(\phi + \pi)}{\sum_{event}^{\uparrow} \cos^2\phi + \sum_{event}^{\downarrow} \cos^2(\phi + \pi)} \\
&= \frac{\sum_{bin}^{\uparrow} n_i \cos\phi_i + \sum_{bin}^{\downarrow} n_j \cos(\phi_j + \pi)}{\sum_{bin}^{\uparrow} n_i \cos^2\phi_i + \sum_{bin}^{\downarrow} n_j \cos^2(\phi_j + \pi)} \\
&= \frac{\sum_{bin} (n_i^{\uparrow} - n_i^{\downarrow}) \cos\phi_i}{\sum_{bin} (n_i^{\uparrow} + n_i^{\downarrow}) \cos^2\phi_i}
\end{aligned} \tag{4.31}$$

where $\sum_{bin}$ means the sum of all $\phi$ bins and $n_i = n(\phi_i)$ the number of events in $\phi_i$ bin for a certain c.m. scattering angle $\theta_{cm}$. In this way, the estimator is independent of the acceptance of the MRS because of the reversal of the beam polarization. However, we took the small differences in beam flux and the computer live time between spin up and down runs into account, and introduced a correction factor to $n_i^{\downarrow}$. The factor is given by

$$\gamma = \frac{(LT \cdot F)^{\uparrow}}{(LT \cdot F)^{\downarrow}} \qquad (4.32)$$

The values of $\gamma$ in experiment 552 are listed in table 4.1.

**Table** 4.1 The values of the correction factor in E552

| Beam Energy (MeV) | 290.7 | 294.9 |
|---|---|---|
| $\gamma$ | 0.973 | 1.013 |

The small difference in beam polarizations between spin up and down runs was also taken into consideration. Suppose for example that the beam polarizations are written as

$$P^{\uparrow} = P_b(1 + \delta) \qquad (4.33)$$

for spin up state and

$$P^{\downarrow} = P_b(1 - \delta) \qquad (4.34)$$

for spin down state, where

$$P_b = \frac{1}{2}(P^{\uparrow} + P^{\downarrow}) . \qquad (4.35)$$

The expressions (4.25) and (4.26) become

$$f^{\uparrow}(\phi) = \frac{1}{2\pi}(1 + \varepsilon \cos\phi + \delta\,\varepsilon \cos\phi)\,\Phi(\phi) \qquad (4.36)$$

for the spin up state and

$$f^{\downarrow}(\phi + \pi) = \frac{1}{2\pi}\,( 1 + \varepsilon \cos\phi - \delta\,\varepsilon \cos\phi )\,\Phi(\phi + \pi) \qquad (4.37)$$

for the spin down state.

Therefore, equation (4.30) becomes

$$f^{\uparrow}(\phi) = \frac{1}{2\pi}\left\{( 1 + \varepsilon \cos\phi )\left[\Phi(\phi) + \Phi(\phi + \pi)\right] + \delta\,\varepsilon \cos\phi \left[\Phi(\phi) - \Phi(\phi + \pi)\right]\right\}$$

$$= f_0(\phi) + \Delta f_0(\phi) \qquad (4.38)$$

where

$$f_0(\phi) = \frac{1}{2\pi}\,( 1 + \varepsilon \cos\phi )\left[\Phi(\phi) + \Phi(\phi + \pi)\right] \qquad (4.39)$$

$$\Delta f_0(\phi) = \frac{1}{2\pi}\,\delta\,\varepsilon \cos\phi \left[\Phi(\phi) - \Phi(\phi + \pi)\right] . \qquad (4.40)$$

Then

$$\int_0^{2\pi} f^{\uparrow}(\phi)\, \cos\phi\, d\phi = \int_0^{2\pi} f_0(\phi)\, \cos\phi\, d\phi + \int_0^{2\pi} \Delta f_0(\phi)\, \cos\phi\, d\phi$$

$$= \int_0^{2\pi} f_0(\phi)\, \cos\phi\, d\phi = \varepsilon \int_0^{2\pi} f_0(\phi)\, \cos^2\phi\, d\phi \qquad (4.41)$$

because it can be shown that

$$\int_0^{2\pi} \Delta f_0(\phi)\, \cos^m\phi\, d\phi = 0 \qquad ( m = \text{odd} ) . \qquad (4.42)$$

The statistical error of the asymmetry $\varepsilon$ is given by

$$( \delta\varepsilon )^2 = \sum_{bin} \left(\frac{\partial \varepsilon}{\partial n_i^{\uparrow}}\right)^2 n_i^{\uparrow} + \sum_{bin} \left(\frac{\partial \varepsilon}{\partial n_i^{\downarrow}}\right)^2 n_i^{\downarrow} + \sum_{bin} \left(\frac{\partial \varepsilon}{\partial \phi_i}\right)^2 (\Delta\phi_i)^2 , \qquad (4.43)$$

where $\sum_{bin}$ means the sum of all $\phi$ bins and $n_i = n(\phi_i)$ the number of events in $\phi_i$ bin for a certain c.m. scattering angle $\theta_{cm}$. In this way, the estimator is independent of the acceptance of the MRS because of the reversal of the beam polarization. However, we took the small differences in beam flux and the computer live time between spin up and down runs into account, and introduced a correction factor to $n_i^{\downarrow}$. The factor is given by

$$\gamma = \frac{(LT \cdot F)^{\uparrow}}{(LT \cdot F)^{\downarrow}} . \qquad (4.32)$$

The values of $\gamma$ in experiment 552 are listed in table 4.1.

**Table** 4.1 The values of the correction factor in E552

| Beam Energy (MeV) | 290.7 | 294.9 |
|---|---|---|
| $\gamma$ | 0.973 | 1.013 |

The small difference in beam polarizations between spin up and down runs was also taken into consideration. Suppose for example that the beam polarizations are written as

$$P^{\uparrow} = P_b(1 + \delta) \qquad (4.33)$$

for spin up state and

$$P^{\downarrow} = P_b(1 - \delta) \qquad (4.34)$$

for spin down state, where

$$P_b = \frac{1}{2}(P^{\uparrow} + P^{\downarrow}) . \qquad (4.35)$$

The expressions (4.25) and (4.26) become

$$f^{\uparrow}(\phi) = \frac{1}{2\pi}(1 + \varepsilon \cos\phi + \delta\, \varepsilon \cos\phi)\, \Phi(\phi) \qquad (4.36)$$

for the spin up state and

$$f^{\downarrow}(\phi + \pi) = \frac{1}{2\pi}\,( 1 + \varepsilon \cos\phi - \delta\,\varepsilon \cos\phi\,)\,\Phi(\phi + \pi) \qquad (4.37)$$

for the spin down state.

Therefore, equation (4.30) becomes

$$f^{\uparrow}(\phi) = \frac{1}{2\pi}\left\{( 1 + \varepsilon \cos\phi\,)\left[\Phi(\phi) + \Phi(\phi + \pi)\right] + \delta\,\varepsilon \cos\phi\left[\Phi(\phi) - \Phi(\phi + \pi)\right]\right\}$$

$$= f_0(\phi) + \Delta f_0(\phi) \qquad (4.38)$$

where

$$f_0(\phi) = \frac{1}{2\pi}\,( 1 + \varepsilon \cos\phi\,)\left[\Phi(\phi) + \Phi(\phi + \pi)\right] \qquad (4.39)$$

$$\Delta f_0(\phi) = \frac{1}{2\pi}\,\delta\,\varepsilon \cos\phi\,\left[\Phi(\phi) - \Phi(\phi + \pi)\right] \quad . \qquad (4.40)$$

Then

$$\int_0^{2\pi} f^{\uparrow}(\phi)\,\cos\phi\,d\phi = \int_0^{2\pi} f_0(\phi)\,\cos\phi\,d\phi + \int_0^{2\pi} \Delta f_0(\phi)\,\cos\phi\,d\phi$$

$$= \int_0^{2\pi} f_0(\phi)\,\cos\phi\,d\phi = \varepsilon \int_0^{2\pi} f_0(\phi)\,\cos^2\phi\,d\phi \qquad (4.41)$$

because it can be shown that

$$\int_0^{2\pi} \Delta f_0(\phi)\,\cos^m\phi\,d\phi = 0 \qquad (\,m = \text{odd}\,)\,. \qquad (4.42)$$

The statistical error of the asymmetry $\varepsilon$ is given by

$$(\,\delta\varepsilon\,)^2 = \sum_{\text{bin}} \left(\frac{\partial\varepsilon}{\partial n_i^{\uparrow}}\right)^2 n_i^{\uparrow} + \sum_{\text{bin}} \left(\frac{\partial\varepsilon}{\partial n_i^{\downarrow}}\right)^2 n_i^{\downarrow} + \sum_{\text{bin}} \left(\frac{\partial\varepsilon}{\partial\phi_i}\right)^2 (\Delta\phi_i)^2\,, \qquad (4.43)$$

where

$$\frac{\partial \varepsilon}{\partial n_i^{\uparrow}} = \frac{1}{\sum_{bin} \left(n_i^{\uparrow} + n_i^{\downarrow}\right) \cos^2 \phi_i} \left[ \cos \phi_i + \varepsilon \cos^2 \phi_i \right] \tag{4.44}$$

$$\frac{\partial \varepsilon}{\partial n_i^{\downarrow}} = \frac{-1}{\sum_{bin} \left(n_i^{\uparrow} + n_i^{\downarrow}\right) \cos^2 \phi_i} \left[ \cos \phi_i + \varepsilon \cos^2 \phi_i \right] \tag{4.45}$$

$$\frac{\partial \varepsilon}{\partial \phi_i} = \frac{-\left(n_i^{\uparrow} - n_i^{\downarrow}\right) \sin \phi_i}{\sum_{bin} \left(n_i^{\uparrow} + n_i^{\downarrow}\right) \cos^2 \phi_i} + \frac{\varepsilon \left(n_i^{\uparrow} + n_i^{\downarrow}\right) 2 \cos \phi_i \sin \phi_i}{\sum_{bin} \left(n_i^{\uparrow} + n_i^{\downarrow}\right) \cos^2 \phi_i} \tag{4.46}$$

Since

$$A_y = \varepsilon / P_b \tag{4.47}$$

we obtain

$$\left(\frac{\Delta A_y}{A_y}\right)^2 = \left(\frac{\Delta \varepsilon}{\varepsilon}\right)^2 + \left(\frac{\Delta P_b}{P_b}\right)^2$$

$$= \left(\frac{\Delta \varepsilon}{\varepsilon}\right)^2 + \frac{\left(\Delta P^{\uparrow}\right)^2 + \left(\Delta P^{\downarrow}\right)^2}{\left(P^{\uparrow} + P^{\downarrow}\right)^2} \tag{4.48}$$

where $P_b$ is the the beam polarization averaged over the two spin states,

$$P_b = \frac{P^{\uparrow} + P^{\downarrow}}{2} \tag{4.49}$$

The beam polarization and its statistical error is given by Eq.(3.5).

## 4.8 Results

### 4.8.1 Results of Experiment 466

The results of total cross sections for $np \rightarrow d\pi^0$ reaction are presented in Fig. 4.10

and table 4.2. Gell-mann and Watson and Rosenfeld[51] have expressed the total cross section in terms of an s-wave part ($\alpha$) and a p-wave part ($\beta$) as

$$\sigma_{total}\,(\,np \rightarrow d\pi^0\,) = \frac{1}{2}\,(\alpha\eta + \beta\eta^3)\,. \tag{4.50}$$

Table 4.3 lists the values of $\alpha$ and $\beta$ fitted in the experiment. Also shown in this table are the results of Rose[10] and Crawford and Stevenson[15]. Note, however, that Rose's values were obtained using different Coulomb correction factors from Reitan's[52].

The differential cross section can be obtained with $A_2 / A_0$ by Eq. (4.16)

$$\frac{d\sigma}{d\Omega}(\theta) = \frac{A_0}{4\pi}\left[1 + \frac{A_2}{A_0}\,P_2(\cos\theta)\right]. \tag{4.51}$$

Fig. 4.11 shows the results of the ratio of Legendre-polynomials coefficients, $A_2 / A_0$, along with those obtained in a previous $np \rightarrow d\pi^0$ study at higher energies reported in ref. 7.

The values of $A_0$ and $A_2$ can now be used to shed some light on the partial-wave amplitudes involved. From equation (1.6), we obtain

$$A_0 = \frac{1}{4}\left[\,|\,a_0\,|^2 + |\,a_1\,|^2 + |\,a_2\,|^2\right] \tag{4.52}$$

$$A_2 = \frac{1}{4}|\,a_2\,|^2 - \frac{1}{\sqrt{2}}\,\mathrm{Re}\,(\,a_0 a_2^*\,)\,. \tag{4.53}$$

To the extent that $a_0$ is negligible, we have

$$|\,a_2\,|^2 = 4\,A_2 \tag{4.54}$$

$$|\,a_1\,|^2 = 4\,(A_0 - A_2)\,, \tag{4.55}$$

that is,

$$r = \frac{|a_2|^2}{|a_1|^2} = \frac{A_2 / A_0}{1 - A_2 / A_0} \qquad (4.56)$$

where r is the ratio of p-wave to s-wave strength. The r values from E466 are also listed in table 4.1. It is clear that the p-wave strength becomes strong even at only a few MeV above threshold.

In Fig. 4.11, two of the the lines are based on the ratios r obtained in Blankleider's calculation[5] (solid line) and the Watson-Bruechner picture[53] (dotted line). The Standard-3 calculation of VBB[20] predicts $A_2 / A_0$ as shown by the dash-dotted curve. The results of E466 clearly rule out the simple Watson-Bruechner model, but are consistent with both of the other calculations.

### 4.8.2 Results of Experiment 552

From the distributions of events in terms of the deuteron c.m. scattering angle ($\theta^d_{cm}$) and azimuthal angle ($\phi$), the analyzing power of the deuteron at a given $\theta_{cm}$ was then determined by summing over weighted contributions from the available azimuthal angles using Eq. (4.31). In the center-of-mass system

$$A_y^{\pi}(\theta^{\pi}_{cm}) = - A_y^{d}(\pi - \theta^{d}_{cm}) . \qquad (4.57)$$

Figure 4.12 shows typical two-dimension spectra of the c.m. scattering angle versus azimuthal angle of the deuteron for both spin up and spin down states at beam energy $T_p$ = 290.7 MeV. Table 4.4 gives the analyzing powers as a function of pion c.m. reaction angle. These analyzing powers are plotted in figure 4.13 for 290.7 and 294.9 MeV incident proton energies.

**Table** 4.2 Measured values of $np \rightarrow d\pi^0$ total cross sections, ratios of Legendre coefficients and p-wave to s-wave strength as a function of mean beam energy. $\eta$ is the pion c.m. momentum in units of pion mass.

| Neutron beam energy (MeV) | $\eta$ | $\sigma_{total}$ $np \rightarrow d\pi^0$ ($\mu$b) | $A_2 / A_0$ | $r = \frlabel{\|a_2\|^2}{\|a_1\|^2}$ |
|---|---|---|---|---|
| 275.09 | 0.015 | 1.77 ± 0.26 | | |
| 275.50 | 0.054 | 4.61 ± 0.99 | | |
| 276.14 | 0.084 | 7.89 ± 0.39 | 0.04 ± 0.06 | 0.04 ± 0.06 |
| 276.98 | 0.112 | 10.71 ± 0.57 | 0.13 ± 0.06 | 0.15 ± 0.06 |
| 277.25 | 0.119 | 10.93 ± 1.07 | | |
| 278.25 | 0.144 | 14.48 ± 0.47 | 0.15 ± 0.07 | 0.18 ± 0.07 |
| 278.99 | 0.160 | 16.84 ± 1.20 | | |
| 280.64 | 0.191 | 19.98 ± 0.67 | 0.21 ± 0.08 | 0.27 ± 0.07 |
| 282.82 | 0.225 | 25.29 ± 0.60 | 0.34 ± 0.06 | 0.51 ± 0.04 |
| 287.11 | 0.281 | 34.23 ± 0.56 | 0.39 ± 0.08 | 0.64 ± 0.05 |
| 290.61 | 0.320 | 43.08 ± 1.30 | 0.55 ± 0.07 | 1.22 ± 0.04 |

**Table** 4.3 Experimental values of $\alpha$ and $\beta$ in the expression (4.50).

| Group | $\alpha$ ($\mu$b) | $\beta$ ($\mu$b) | Measurement |
|---|---|---|---|
| Rose | 240 ± 20 | 520 ± 200 | $\pi^+ d \rightarrow pp$ |
| Crawford & Stevenson | 138 ± 15 | 1010 ± 80 | $pp \rightarrow \pi^+ d$ |
| E466 | 184 ± 5 | 781 ± 79 | $np \rightarrow \pi^0 d$ |

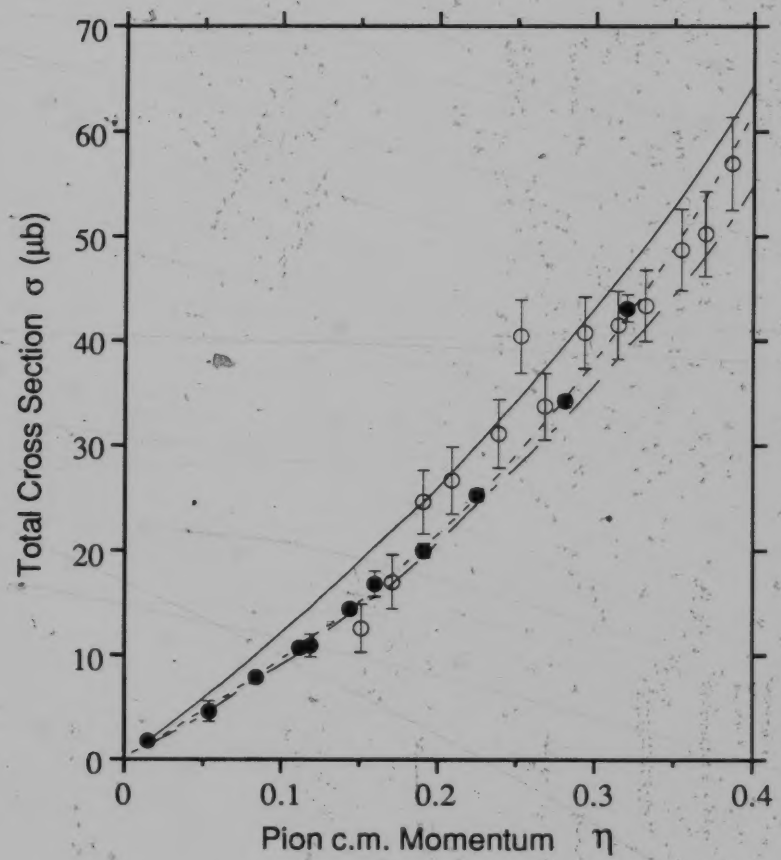


Fig. 4.10 Total $np \rightarrow d\pi^0$ cross sections as a function of pion c.m. momentum $\eta$. The solid circles are the data from E466, the open circles Rose's data (Ref. 10). The dashed and solid lines are fits to the data from E466 and Rose's data respectively, using the expression (4.50). The dashed-dotted curve is the Standard-3 calculation of VBB (Ref. 20).

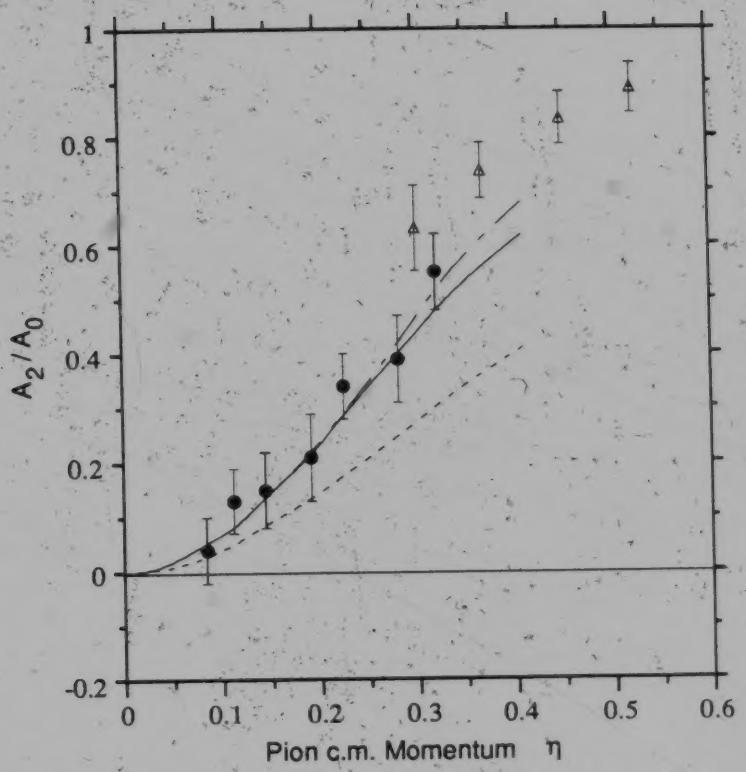


Fig. 4.11 Ratios of Legendre-polynomial coefficients, $A_2 / A_0$, as a function of pion c.m. momentum. The solid circles are the results from E466 and the triangles are those of the Freiburg group, reported in Ref. 7. The dotted line is the prediction of the Watson-Brueckner model (Ref. 53), the solid line that of Blankleider (Ref. 5), and the dash-dotted line the Standard-3 prediction of VBB (Ref. 20).

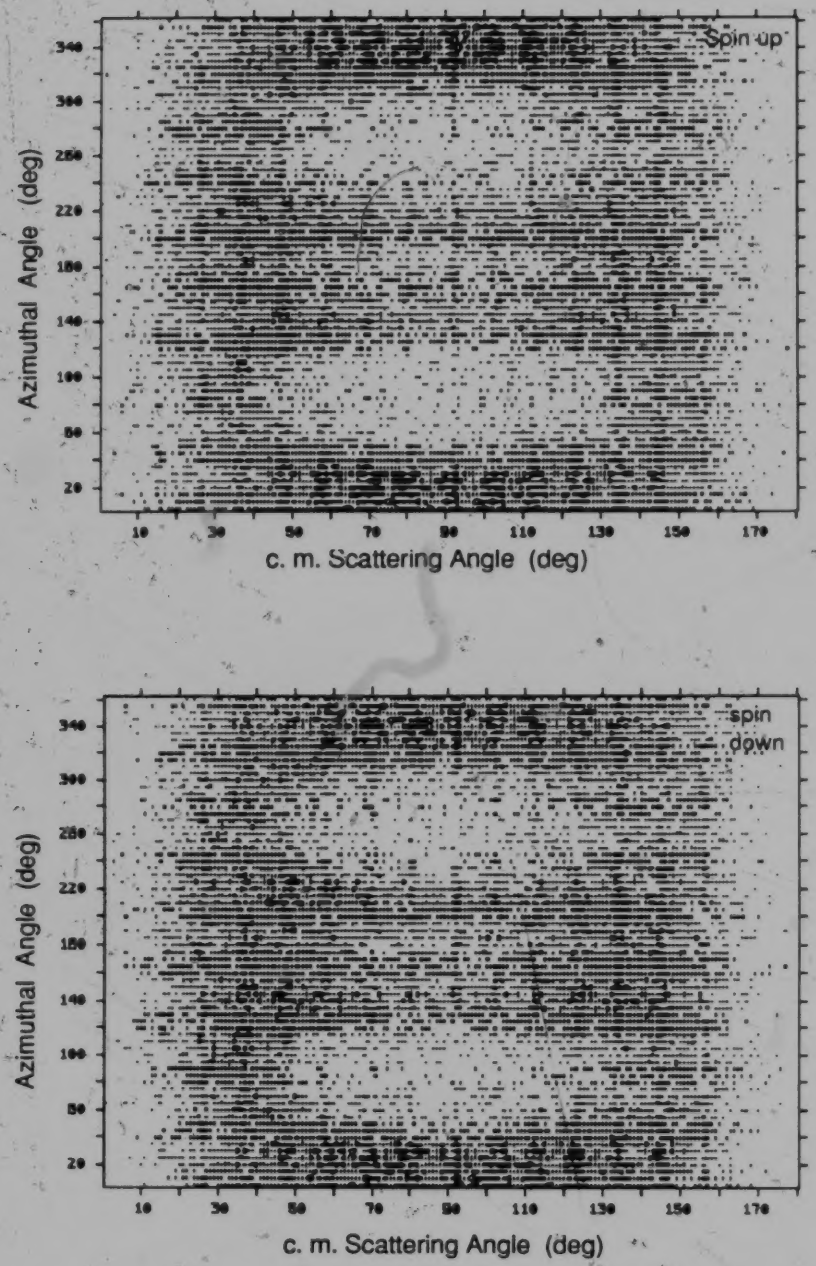


Fig.4.12 Distribution of events as a function of the c.m. scattering angle and the azimuthal angle of the deuteron for the spin up state (top) and the spin down state (bottom).

**Table 4.4** $\vec{p}p \rightarrow d\pi^+$ analyzing power angular distributions

| Pion c.m. Angle | $T_p$ = 290.7 MeV | $T_p$ = 294.9 MeV |
|---|---|---|
| | $A_y$ | $A_y$ |
| 7.5 | - 0.069 ± 0.083 | - 0.023 ± 0.094 |
| 22.5 | - 0.127 ± 0.041 | - 0.044 ± 0.035 |
| 37.5 | - 0.062 ± 0.024 | - 0.084 ± 0.028 |
| 52.5 | - 0.120 ± 0.022 | - 0.206 ± 0.026 |
| 67.5 | - 0.172 ± 0.023 | - 0.229 ± 0.026 |
| 82.5 | - 0.185 ± 0.022 | - 0.282 ± 0.024 |
| 97.5 | - 0.164 ± 0.023 | - 0.293 ± 0.025 |
| 112.5 | - 0.191 ± 0.022 | - 0.252 ± 0.024 |
| 127.5 | - 0.153 ± 0.022 | - 0.208 ± 0.024 |
| 142.5 | - 0.065 ± 0.023 | - 0.145 ± 0.025 |
| 157.5 | - 0.078 ± 0.037 | - 0.053 ± 0.034 |
| 172.5 | - 0.127 ± 0.106 | - 0.074 ± 0.082 |

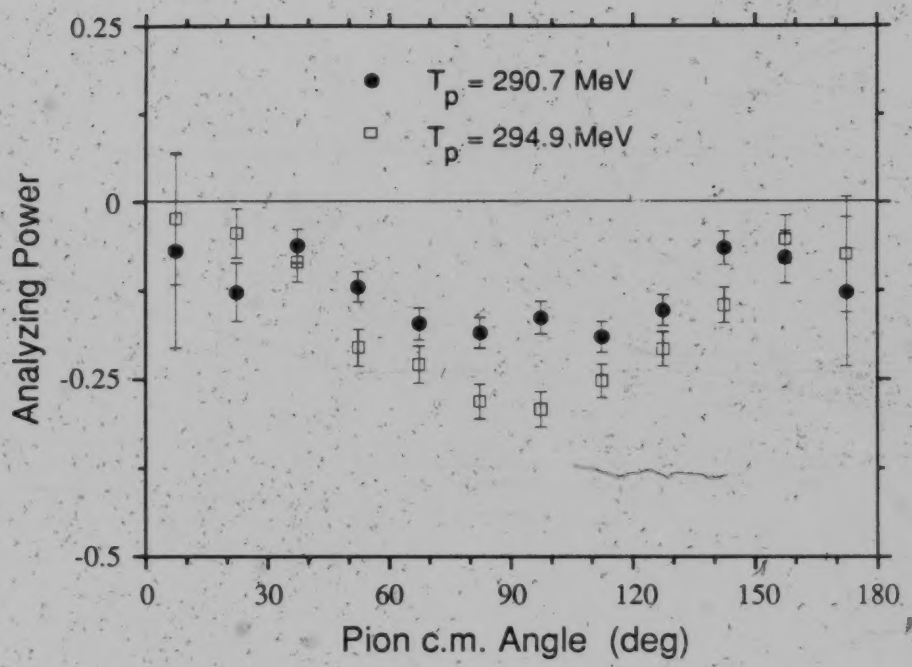


Figure 4.13 Analyzing powers for the reaction $\vec{p}p \rightarrow d\pi^+$ as a function of pion c.m. angle for 290.7 and 294.9 MeV proton beams.

# Chapter 5 Discussion and Conclusion

## 5.1 Partial Wave Amplitude Analysis

### 5.1.1 Partial Wave Phase Shift

The phase of a partial wave amplitude in $NN \rightarrow d\pi$ is the sum of phase shifts for the same partial wave in NN and in $\pi d$ elastic scattering at the energies near threshold according to Watson's theorem[22]

$$\delta(NN \rightarrow d\pi) = \delta(NN) + \delta(\pi d) \qquad (5.1)$$

For our experiment, only amplitudes $a_0$, $a_1$, and $a_2$ are considered (see sec. 1.4). The corresponding phase shifts are expressed as (see table 1.1)

$$\delta_0 = \delta_{NN}({}^1S_0) + \delta_{\pi d}(\text{p-wave}) \qquad (5.2)$$

$$\delta_1 = \delta_{NN}({}^3P_1) + \delta_{\pi d}(\text{s-wave}) \qquad (5.3)$$

$$\delta_2 = \delta_{NN}({}^1D_2) + \delta_{\pi d}(\text{p-wave}) \qquad (5.4)$$

The NN elastic phase shifts are determined from the solution C300 in SAID[45] and listed in table 5.1. At very low energy, the p-wave phase shift in $\pi d$ elastic scattering can be neglected[45,54]. The $\delta_{\pi d}$(s-wave) can be determined by virtue of the expression[37]

$$a_{\pi d} = \frac{1}{\eta} \tan \delta_{\pi d}(\text{s-wave}) \; , \qquad (5.5)$$

where $a_{\pi d}$ is the scattering length whose experimental values are[55,56]

$$\text{Re } a_{\pi d} = -(5.6 \pm 0.9) \times 10^{-2} m_\pi^{-1} \qquad (5.6a)$$

$$\text{Im } a_{\pi d} = -(4.8 \pm 0.7) \times 10^{-3} m_\pi^{-1} . \qquad (5.6b)$$

The resulting values of $\delta_0$, $\delta_1$, and $\delta_2$ are listed in table 5.1.

**Table** 5.1 The partial-wave phase shifts for NN and πd scattering near the pion production threshold.

| $T_p$ (MeV) | 290.7 | 294.9 |
|---|---|---|
| η | 0.14 | 0.22 |
| $\delta_{NN}(^1S_0)$ (deg) | - 5.66 ± 0.29 | - 6.14 ± 0.29 |
| $\delta_{NN}(^3P_1)$ (deg) | - 26.78 ± 0.19 | - 27.10 ± 0.19 |
| $\delta_{NN}(^1D_2)$ (deg) | 9.12 ± 0.10 | 9.21 ± 0.10 |
| δ (s-wave) (deg) | 0.45 ± 0.07 | 0.71 ± 0.11 |
| $\delta_0$ (deg) | - 5.66 ± 0.29 | - 6.14 ± 0.29 |
| $\delta_1$ (deg) | - 26.33 ± 0.20 | - 26.39 ± 0.22 |
| $\delta_2$ (deg) | 9.12 ± 0.10 | 9.21 ± 0.10 |

**Table** 5.2 The Legendre-polynomial coefficients $A_0$ and $A_2$, and constant C in Eq. (5.9) for reaction $pp \rightarrow d\pi^+$.

| η | $A_0$ | $A_2$ | C |
|---|---|---|---|
| 0.14 | 27.90 ± 0.73 | 4.19 ± 0.85 | - 4.75 ± 0.07 |
| 0.22 | 48.80 ± 1.33 | 13.81 ± 1.51 | - 12.02 ± 0.25 |

**5.1.2** $pp \rightarrow d\pi^+$ cross sections extracted from E466

The $np \rightarrow d\pi^0$ total and differential cross sections have been measured in experiment 466 as a function of $\eta$. Using the expression

$$\sigma_{tot}(pp \rightarrow d\pi^+) = 2\,\sigma_{tot}(np \rightarrow d\pi^0) = \alpha\eta + \beta\eta^3 \qquad (5.7)$$

and the fitted values of $\alpha$ and $\beta$ in table 4.3, we obtain the total cross section for $pp \rightarrow d\pi^+$, that is, Legendre-polynomial coefficient $A_0$, at the two energies of interest. The values of the other Legendre- polynomial coefficient $A_2$ in Eq. (4.51) are likewise obtained using a polynomial fitting[57] to the results of E466 in fig. 4.11. These $A_0$ and $A_2$ values are shown in table 5.2.

**5.1.3** Partial wave amplitudes

Let

$$C(\theta) = \frac{4\pi\,(d\sigma/d\Omega)_0\,A_y}{\sin\theta} = \frac{\left[A_0 + A_2\,P_2(\cos\theta)\right]A_y(\theta)}{\sin\theta} \qquad (5.8)$$

From Eq. (1.8), we have

$$C(\theta) = \frac{1}{4}|a_1||a_2|\sin(\delta_1 - \delta_2) - \frac{1}{2\sqrt{2}}|a_0||a_1|\sin(\delta_0 - \delta_1) \qquad (5.9)$$

Since C is apparently independent of pion c.m. scattering angle $\theta$ in Eq. (5.9), we fit $C(\theta)$ in Eq. (5.8) calculated from the values in table 4.4 and table 5.2 to a constant, i.e., $C(\theta) = C$. The values of C thus obtained are listed in table 5.2.

The magnitudes of $a_0$, $a_1$, and $a_2$ are determined by solving the Eqs. (5.9), (4.52), and (4.53) simultaneously. The values of the amplitudes $a_0$, $a_1$, and $a_2$ are listed in table 5.3 and plotted in fig. 5.1, along with Bugg's results at higher energies[22,40]. Note that

Bugg's results which are shown in fig. 5.1 have been converted from the amplitudes definition of Kamo and Watari[58] to the amplitudes definition of Blankleider[5] (which we are using) by the expression[22]

$$a\,(\text{Blankleider}) = 2208.4\,\frac{\sqrt{2\mathfrak{L}+1}}{P_{cm}}\,a\,(\text{Watari}) \qquad (5.10)$$

where $P_{cm}$ is the nucleon c.m. momentum in units of MeV/c, and $\mathfrak{L}$ is the pp partial-wave orbital angular momentum (see table 1.1).

**Table** 5.3 The magnitudes of the partial-wave amplitudes in units of $10^{-2}$ fm.

| $T_p$ (MeV) | $\eta$ | $\lvert a_0 \rvert$ | $\lvert a_1 \rvert$ | $\lvert a_2 \rvert$ |
|---|---|---|---|---|
| 290.7 | 0.14 | - 0.36 ± 0.36 | 9.91 ± 1.18 | 3.62 ± 0.15 |
| 294.9 | 0.22 | - 0.23 ± 0.34 | 12.05 ± 0.74 | 7.08 ± 0.18 |

The values in table 5.3 are the magnitudes of the amplitudes; a negative value is unphysical. Considering the error, however, $a_0$ can be regarded essentially as a negligible quantity or zero for both $\eta$=0.14 and $\eta$=0.22. Nevertheless, the apparent tendency of $|a_0|$ towards the unphysical negative values at both energies might be a reflection of potential very small inaccuracies related to the two underlying assumptions: Watson's theorem, and the comparison of $np \rightarrow d\pi^0$ an $pp \rightarrow d\pi^+$ cross sections at the same $\eta$.

Setting $a_0$=0, we estimated the $pp \rightarrow d\pi^+$ analyzing powers at $\theta_{cm}$=90°, $A_y(90°)$, using only the results of E466 by virtue of eqs. (4.52), (4.53) and (5.9). We then compared these values with the fitted experimental results from E552. The comparison, shown in fig. 5.2, appears to basically indicate that the $np \rightarrow d\pi^0$ and $pp \rightarrow d\pi^+$ results are consistent and that application of Watson's theorem is, to a large extent, justified.

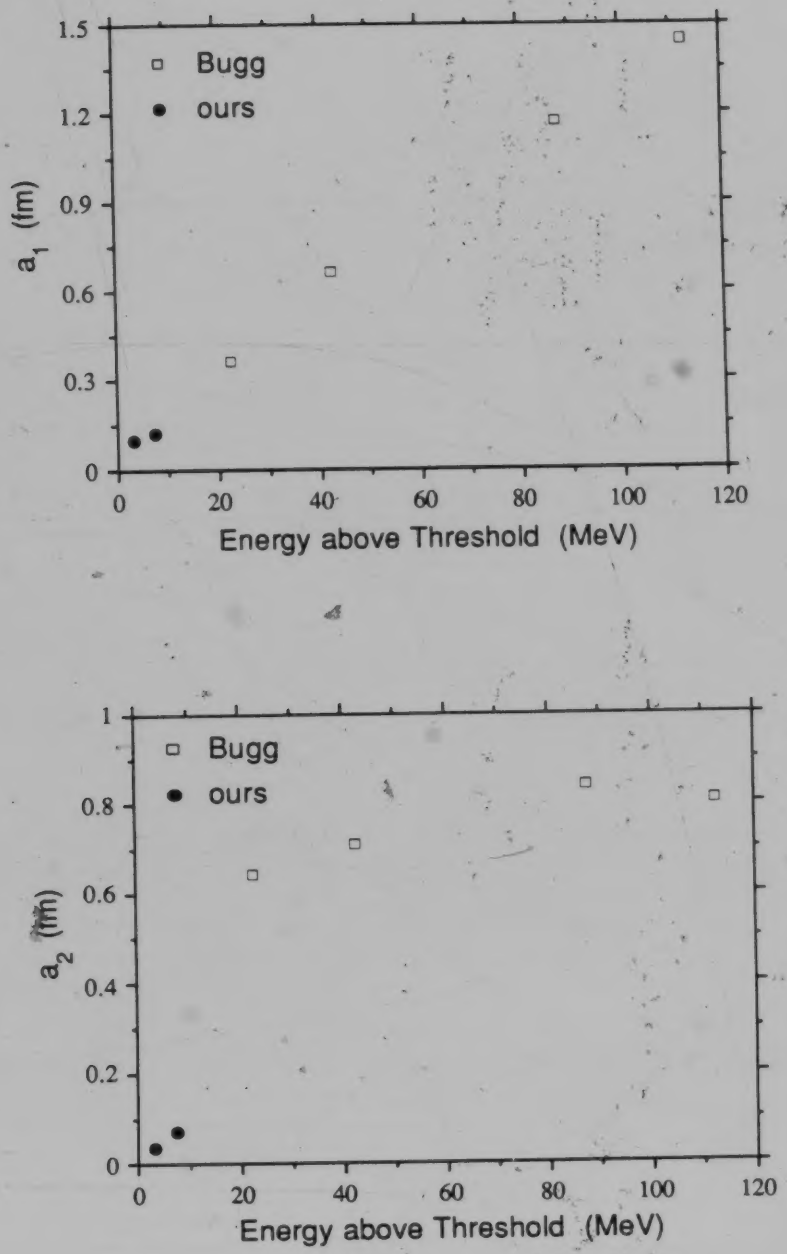


Fig. 5.1 The amplitudes $a_1$ and $a_2$ as a function of proton beam energy in the reaction $pp \rightarrow d\pi^+$. The error bar of each our data point is smaller than the corresponding symbol.

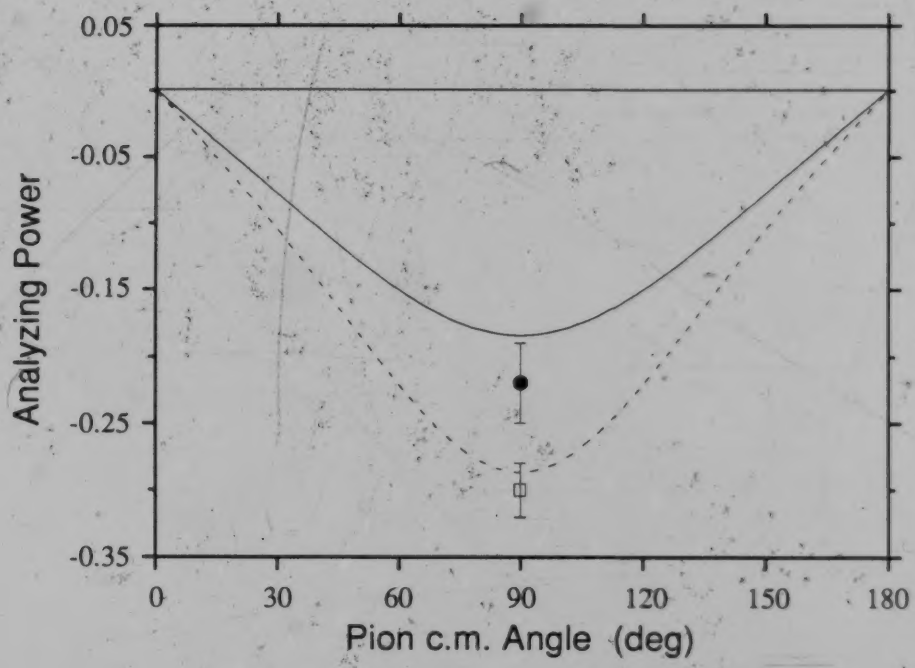


Figure 5.2 Comparison of analyzing powers from E552 and E466. The solid and dashed lines represent the fitted results with $\sigma$=0.01 from E552 at 290.7 MeV ($\eta$=0.14) and 294.9 MeV ($\eta$=0.22) beam energy, respectively. The solid circle and open square represent the values predicted from the results from E466 only (assuming $a_0$=0) for $\eta$=0.14 and $\eta$=0.22 respectively.

## 5.2 Conclusion

Experimentally, a better understanding of basic pion production process will of course be possible when enough experimental information is available to allow the extraction of a certain number of partial-wave amplitudes independently of any theoretical input. With current results of the $\vec{p}p \rightarrow d\pi^+$ analyzing powers at 3 and 7 MeV above threshold and combination of the results of cross sections from previous measurements of $np \rightarrow d\pi^0$, we have determined the partial-wave amplitudes dominating pion production near threshold in the reaction $NN \rightarrow d\pi$. As expected, it is found that s-wave pion production ($a_1$ amplitude) dominates the reaction very close to threshold. But, it is also clear that p-wave pion production becomes strong even at only a few MeV above threshold. We found that the $a_2$ amplitude dominates p-wave pion production, and the $a_0$ amplitude is negligible.

The analyzing power for the reaction $\vec{p}p \rightarrow d\pi^+$ from threshold to 600 MeV is now known. Fig. 5.3 illustrates the $\vec{p}p \rightarrow d\pi^+$ analyzing power at 90° as a function of beam energy. It is clear that the results of experiment 552 are consistent with the tendency of the previous analyzing power measurements.

The newly determined analyzing powers (E552) and previous cross sections measurements (E466) should encourage a more rigorous theoretical treatment of the $NN \rightarrow d\pi$ reaction mechanism at the long neglected energy region[23] very near threshold.

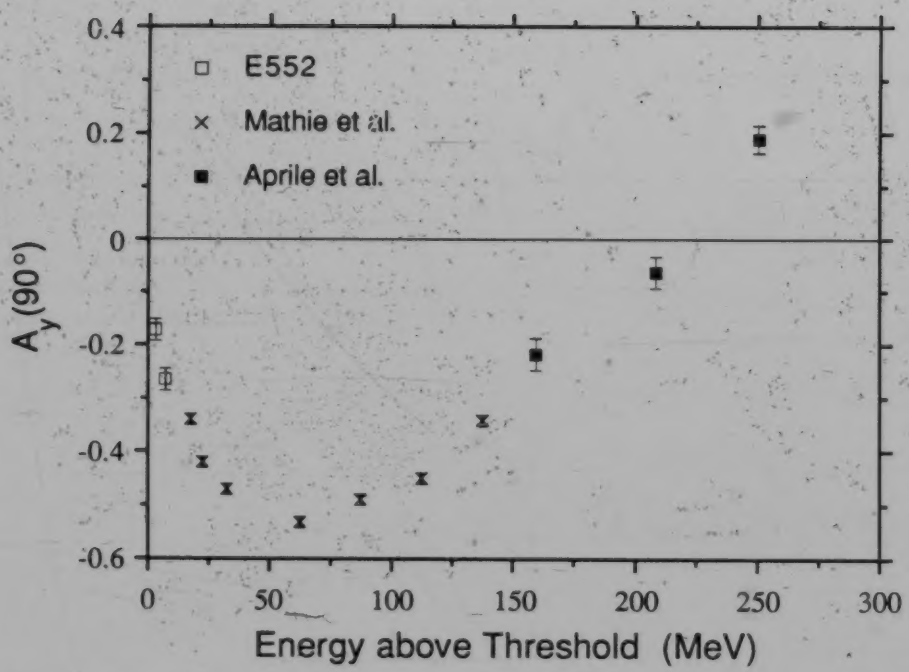


Figure 5.3 The reaction $\vec{p}p \rightarrow d\pi^+$ analyzing power at pion c.m. reaction angle equal to 90° as a function of beam energy.

# References


1. T. Sloan, G. Smadja and R. Voss, Phys. Rep. **162**, 45 (1988).
2. G. S. Kyle, " Pion-Nucleus Physics ", ed. R.J.Peterson & D. D. Strottman, AIP Conference Proceedings No. **163**, 289(1988).
3. H. Dijk and B.L.G. Bakker, Nucl. Phys. **A494**, 438 (1989).
4. F. Mandl and T. Regge, Phys. Rev. **99**, 1478 (1955).
5. B. Blankleider and I.R. Afnan, Phys. Rev. **C24**, 1572 (1981).
6. G. Jones, Nucl. Phys. **A416**, 157 (1984).
7. G. Jones, " Pion Production and Absorption - 1981", ed. R.D. Bent, AIP Conference Proceedings No. **79**, 15 (1982).
8. N. Hiroshige, W. Watari and M. Yonezawa, Prog. Theor. Phys. **72**, 1146 (1984).
9. D. Hutcheon *et al.*, Phys. Rev. Lett. **64**, 176 (1990).
10. C. M. Rose, Phys. Rev. **154**, 1305 (1967).
11. E. Mathie *et al.*, Nucl. Phys. **A397**, 469 (1983).
12. F. Schimizu *et al.*, Nucl. Phys. **A386**, 571 (1982).
13. B.G. Ritchie *et al.*, Phys. Rev. **C24**, 552 (1983).
14. G. Giles *et al.*, "Few Body Problems in Physics", ed. B. Zeitnitz, Few Body X, 1983, p515.
15. F.S. Crawford and M. L Stevenson, Phys. Rev. **97**, 1305 (1955).
16. S.S. Wilson *et al.*, Nucl. Phys. **B33**, 253 (1971).
17. D. Axen *et al.*, Nucl. Phys. **A256**, 387 (1967).
18. A.M. Sachs *et al.*, Phys. Rev. **109**, 1733 (1958).
19. J.A. Niskanen, Private Communication, 1988.
20. J. Vogelzang, B.L.G. Bakker, and H.J. Boersma, Nucl. Phys. **A452**, 644 (1986).
21. B. Blankleider and I.R. Afnan, Phys. Rev. **C31**, 469 (1985).
22. D.V. Bugg, J. Phys. **G10**, 47 (1984).
23. M. Betz, B. Blankleider, J.A. Niskanen and A. W. Thomas, " Pion Production and Absorption - 1981", ed. R.D. Bent, AIP Conference Proceedings No. **79**, 65 (1982).

24. O.V. Maxwell, W. Weise and M. Brack, Nucl. Phys. A**348**, 388 (1980).

25. J. Chai and D.O. Riska, Nucl. Phys. A**338**, 349 (1980).

26. A.M. Green, J. A. Niskanen and M.E. Sanio, J. Phys. G**4**, 1055 (1978).

27. J.A. Niskanen, Nucl. Phys. A**298**, 417 (1978).

28. I.R. Afnan and A.W. Thomas, Phys. Rev. C**10**, 109(1974).

29. Y. Avishai and T. Mizutani, Nucl. Phys. A**326**, 352 (1979); A**338**, 377 (1980); A**352**, 399 (1981); Phys. Rev. C**27**, 312 (1983).

30. G.H. Lamot, J.L. Perrot, C. Fayard, and T. Mizutani, Phys. Rev. C**35**, 239 (1987).

31. W. Grein, A. Konig, P. Kroll, M.P. Locher and A. Svarc, Ann. of Phys. **153**, 301 (1984).

32. B. Blankleider, Nucl. Phys. A**463**, 77 (1987).

33. E. Aprile *et al.*, Nucl. Phys. A**415**, 365 (1984).

34. E.O. Alt, P. Grassberger, and W. Sandhas, Nucl. Phys. B**2**, 167 (1967).

35. C. Richard-Serre *et al.*, Nucl. Phys. B**20**, 413 (1970).

36. I.R. Afnan and R.J. Mcleod, Phys. Rev. C**31**, 1821(1985).

37. T. Ericson and W. Weise, Pions and Nuclei, Clarendon Press, Oxford, 1988.

38. D.S. Koltun and A. Reitan, Phys. Rev. **141**, 1413 (1966).

39. A.V. Kravtsov, M.G. Ryskin, and I.I. Strakovsky, J. Phys. G**9**, L187 (1983).

40. D. Bugg *et al.*, Nucl. Phys. A**477**, 546 (1988).

41. A.S. Rinat and Y. Starkand, Nucl. Phys. A**397**, 381 (1983).

42. R. Helmer, Can. J. Phys. **65**, 588 (1987).

43. G.W.R. Edwards *et al*, Nucl. Instr. Meth. ( to be published).

44. The TRIUMF Medium Resolution Spectrometer Manual TRIUMF (unpublished).

45. R. Arndt *et al.*, Scattering Analysis Interactive Dial-in (SAID) program; R. Arndt *et al.*, Phys. Rev. D**28**, 97 (1983).

46. G.A. Ludgate, The VDACS Data Acquisition and Analysis System Primer TRIUMF (unpublished).

47. TWOTRAN reference manual, (TRIUMF,1988).

48. D. Frekers, LISA Documentation Manual TRIUMF (unpublished).

49. K. Hicks, A LISA-VDACS Interface Primer TRIUMF (unpublished).

50. D. Besset *et al.*, Nucl. Instr. and Meth. **166**, 5 (1979).

51. M. Gell-Mann and K. M. Watson, Ann. Rev. Nucl. Sci. **4**, 219 (1954).
A.H. Rosenfeld, Phys. Rev. **96**, 139 (1954).
52. A. Reitan, Nucl. Phys. **B11**, 170 (1969).
53. K. Watson and K. Brueckner, Phys. Rev. **83**, 1 (1951).
54. G. Rowe and M. Salomon, Phys. Rev. **C18**, 584 (1978).
55. E. Bovet *et al.*, Phys. Lett. **153**B, 231 (1985).
56. J. Spuller and D.F. Measday, Phys. Rev. **D12**, 3550 (1975).
57. W.T. Eaddie, D. Drijard, F.E.James, M. Roos and B. Sadoulet, Statistical Methods in Experimental Physics, North-Holland, Amsterdam, p164, (1971).
58. H. Kamo, W. Watari and M. Yonezawa, Prog. Theor. Phys. **62**, 1035 (1979).

# Appendix I Vavilov Distribution

## I.1 Energy Loss Calculations for Heavy Charged Particles

A heavy charged particle of mass $M >> m_e$, charge $Z_e$ and speed $\beta c$ passing through a medium loses energy primarily through its interaction with the atomic electrons of the medium. The Bethe-Bloch[I1] equation gives the mean rate of energy loss per unit path length

$$\frac{dE}{dx} = \frac{4\pi N_A r_e^2 c^2 Z_{med} \rho_{med}}{A_{med}} \frac{Z^2}{\beta^2} \left\{ \frac{1}{2} \ln \frac{2m_e \gamma^2 \beta^2 c^2 T_{max}}{I_{adj}^2} - \beta^2 - \frac{\delta}{2} - \frac{C}{Z_{med}} \right\}, \qquad (I.1)$$

where $Z_{med}$ is the charge of the medium, $\rho_{med}$ is the density, $A_{med}$ is the atomic mass, $I_{adj}$ is the adjusted ionization potential, $\delta$ is a density correction applicable at high energy, and C represents Shell corrections. The maximum energy transferred to an electron is

$$T_{max} = \frac{2 m_e c^2 \gamma^2 \beta^2}{1 + 2\gamma \frac{m_e}{M} + \left[\frac{m_e}{M}\right]^2} \qquad (I.2)$$

and the constant

$$4\pi N_A r_e^2 m_e^2 = 0.3070 \text{ MeV cm}^2/\text{g} \qquad (I.3)$$

is used.

The quantity $(dE/dx)\cdot\delta x$ is the mean energy loss in a thickness $\delta x$. The actual loss fluctuates due to statistical variations in the number of collisions and in the energy transferred to the individual electrons. For thicknesses such that $(dE/dx)\cdot\delta x >> 2 m_e c^2 \gamma^2 \beta^2$, the distribution of energy losses becomes a Gaussian. For smaller

thicknesses the Landau or Vavilov distributions apply. The thickness limit above is better understood when compared to the expression (I.2) for $T_{max}$.

When using the Vavilov distribution the following parameter is used

$$\kappa = 0.3070 \frac{m_e c^2}{\beta^2} \frac{Z_{med}}{A_{med}} \frac{s}{T_{max}} = \frac{\xi}{T_{max}} \qquad (I.4)$$

where s is the target thickness. It has been shown that the value $\kappa=0$ corresponds to a Landau distribution, and $\kappa >> 1$ corresponds to a Gaussian distribution, and others correspond to a Vavilov distribution[I2,I3].

**I.2** Vavilov Distribution

The Vavilov distribution is often used to describe the energy loss of charged particles traversing a thin layer of matter.

Using the notations $\Delta$ and $\bar{\Delta}$ to represent energy loss and mean energy loss, respectively, and $f(\Delta, s)d\Delta$ to denote the probability that a heavy particle, in traversing a thickness s in the target, will suffer an energy loss between $\Delta$ and $\Delta+d\Delta$ as the result of many successive collisions with atomic electrons, the Vavilov distribution is then given by

$$f(\Delta, s)d\Delta = \frac{1}{\xi} \varphi_v(\lambda_v, \kappa, \beta^2)\, d\lambda_v \,, \qquad (I.5)$$

where

$$\varphi_v(\lambda_v, \kappa, \beta^2) = \frac{\kappa}{\pi} e^{\kappa(1+\beta^2\gamma)} \int_0^\infty e^{\kappa f_1} \cos(y\lambda_v + \kappa f_2)\, dy$$

$$\lambda_v = \frac{\Delta - \bar{\Delta}}{T_{max}} - \kappa(1 + \beta^2 - \gamma)$$

$\gamma = 0.577216$ . (Euler's constant)

$$f_1 = \beta^2[\ln y + Ci(y)] - \cos y - y\, Si(y)$$

$$f_2 = y\,[\ln y + Ci(y)] + \sin y + \beta^2\, Si(y) \qquad (I.6)$$

$$Si(y) = \int_0^y \frac{\sin u}{u}\, du \quad \text{(sine integral)}$$

$$Ci(y) = \int_{-}^{y} \frac{\cos u}{u}\, du \quad \text{(cosine integral)} .$$

Introducing the Landau parameter

$$\lambda = \lambda_{\sqrt{}}/\kappa - \ln \kappa = \frac{\Delta - \bar{\Delta}}{\xi} - 1 - \beta^2 + \gamma - \ln \kappa , \qquad (I.7)$$

setting $y = x/\kappa$, and noting that $Ci(y) \rightarrow \frac{\sin y}{y}$ and $Si(y) \rightarrow \frac{\pi}{2}$ for large y, one obtains the result that

$$\lim_{\kappa \rightarrow 0} f(\Delta, s) = \frac{1}{\pi\xi} \int_0^{\infty} e^{-\frac{\pi x}{2}} \cos\left[x(\ln x + \lambda)\right] dx . \qquad (I.8)$$

(Landau distribution)

Therefore in the limit $\kappa \rightarrow 0$, the Vavilov distribution goes over to the Landau distribution.

For $\kappa >> 1$, the distribution becomes approximately Gaussian:

$$f(\Delta,s) \rightarrow \frac{1}{\xi\sqrt{\frac{2\pi}{\kappa}(1 - \beta^2/2)}} \exp\left\{ - \frac{(\Delta - \bar{\Delta})^2 \kappa}{2\xi^2(1 - \beta^2/2)} \right\} . \qquad (I.9)$$

## I.3 Application of Vavilov distribution to experiment 552

The probability density function of the Vavilov distribution is given in Ref.I4 in terms of the parameter $\lambda$ as DISVAV($\lambda$,0). The energy loss $\Delta$ in terms of $\lambda$ is given by

$$\Delta = \overline{\Delta} + \xi [\lambda + 1 + \beta^2 - \gamma + \ln \kappa] , \qquad (I.10)$$

where mean energy loss $\overline{\Delta}$ is calculated by the code LOSSPROG[15].

In experiment 552, Vavilov distribution of 140 MeV deuterons traversing a liquid hydrogen target of thickness 0.75 cm was calculated in the following program. The energy loss distribution is plotted in Fig. I1.

Therefore, the low energy region in fig. 4.9 which differs from a Gaussian distribution is really due to the contribution of Vavilov energy loss distribution.

```
CC  THE PROGRAM CALCULATES THE ENERGY LOSS OF DEUTERONS TRAVERSING
CC   A THIN LAYER OF MATTER OF THICKNESS S USING THE PROBABILITY DENSITY
CC   FUNCTION DISVAV(LAMDA,0) OF VAVILOV DISTRIBUTION
CC      XF = DE/DX
        DIMENSION DEN(120),DIS(120),LAMDA(120),XF(120),DE(120)
        REAL LAMDA
        S = 0.75     ! CM
        T = 140.0
        W = 1875.63
        P = SQRT((T+W)**2 - W**2)
        BETA = P/(T+W)
        BE2=BETA*BETA
        GA = 1./SQRT(1.-BE2)
        TMAX = 2.0*0.511*GA*GA*BE2/(1 + 2*GA*0.511/W + (0.511/W)**2)
        RK = 0.3070*0.511*S/BE2*TMAX
        TYPE*,'RK=',RK
CC  CALCULATE THE PROBABILITY DENSITY FUNCTION 'DEN '
        CALL COEDIS(RK,BE2,0,10)
        DO I=1,120
                LAMDA(I) = 0.12*FLOAT(I) - 3.6
                DEN(I) = DISVAV(LAMDA(I),0)
                WRITE(20,100)LAMDA(I),DEN(I)
        ENDDO
        CALL COEDIS(RK,BE2,1,10)
CC  CALCULATE THE CONTIONAL DISTRIBUTION 'DIS'
        DO I=1,100
                LAMDA(I) = 0.12*FLOAT(I) - 3.6
                DIS(I) = DISVAV(LAMDA(I),1)
                WRITE(30,100)LAMDA(I),DIS(I)
        ENDDO
CC  CALCULATE THE energy loss
cc  MEAN ENERGY LOSS EXI IS GOTTEN FROM CODE "LOSSPROG" AT A CERTAIN ENERGY.
        EXI = 1.050     ! IN MEV
        DO I=1,120
                XF(I)=EXI+(LAMDA(I)+LOG(RK)+1.+BE2-0.577216)*TMAX*RK
                WRITE(40,100)XF(I),DEN(I)
                WRITE(41,100)XF(I),DIS(I)
        ENDDO
100     FORMAT(2X,F10.5,5X,F10.5)
        STOP
        END
```

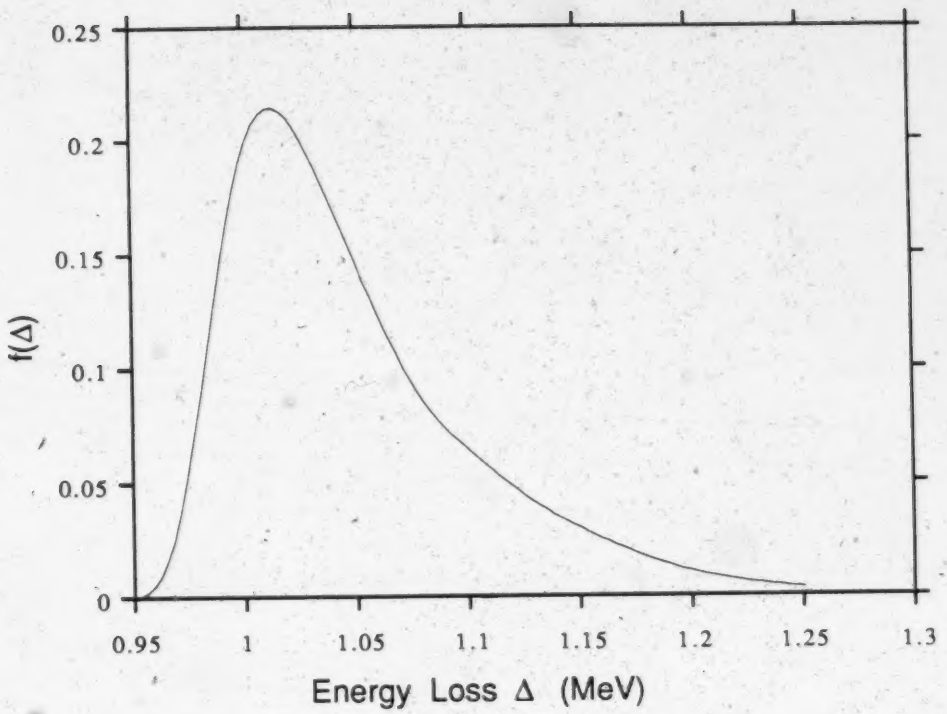


Fig. f1 The energy loss distribution of 140 MeV deuterons traversing a $LH_2$ target of thickness 0.75 cm in E552.

References:

I1. U. Fano. Ann. Rev. Nucl. Rev. **13**, 1 (1963).

I2. P.V. Vavilov, JETP **5**, 749 (1957).

I3. S.M. Seltzer and M.J. Berger, Studies in penetration of charged particles in matter, Nucl. Sci. Series Rep. No. 39, Nat. Acad. Scs. Washington, D.C. (1964) 187p .

I4. B. Schorr, Program for the Vavilov Distribution and the Corresponding Random Numbers, CERN Computer Center, Program Library, Long Write-up, G111.

I5. L.G. Greeniaus, computer code LOSSPROG, (University of Alberta, Edmonton, Canada, 1987), unpublished.

# Appendix II CSB Effect in the E466

## II.1 Charge Symmetry and Charge Symmetry Breaking

Isospin was the first internal symmetry postulated for the N-N force[II.1]. Neutrons and protons were viewed as two states of a single particle defined by the direction of a vector in isospin space. By analogy with ordinary spin and angular momentum it was natural to postulate that the strong interaction Hamiltonian $H_{str}$ might be invariant under arbitrary rotations in this abstract isospin space, i.e.

$$[\, H_{str} , \mathbf{T} \,] = 0, \tag{II.1}$$

where **T** is the isospin operator with components(1,2,3). The third component of isospin is related to the charge; conventionally the proton has $T_3 = +1/2$ and the neutron has $T_3 = -1/2$. Eq.(II.1) is the mathematical statement of charge independence.

Since electromagnetic interactions break charge independence (CIB), violations on the order of the fine structure constant are to be expected. Charge symmetry is a less restrictive constraint than isospin invariance. It only requires that $H_{str}$ be the invariant for 180° rotations about the 2-axis in isospin space,

$$[\, H_{str} , P_{cs} \,] = 0, \qquad P_{cs} = e^{i\pi T_2} . \tag{II.2}$$

A charge independent interaction must also be charge symmetric, but the converse is not necessarily true. The charge symmetry operator reverses the "3-axis" of the isospin space, for example changing neutrons into protons, or $\pi^+$ into $\pi^-$ and vice versa. In the special case of two nucleons (N-N system) it implies that the n-n and p-p forces should be identical, but it does not relate them to the n-p force. In the case where $P_{cs}$ acts on the an eigenstate of $\mathbf{T}^2$ and $T_3$ labelled $|t, t_3\rangle$ we find

$$P_{cs} |t, t_3\rangle = (-1)^{t+t_3} |t, -t_3\rangle , \tag{II.3}$$

which amounts to reflecting the system in the (1-2)-plane.

At the hadronic level the reasons for isospin symmetry breaking can be traced to mass differences between different charge states of mesons and baryons, to electromagnetic interaction effects and to the fact that mesons of different isospins mix ($\pi^0$ and $\eta$ or $\rho$ and $\omega$)[II.2]. Earlier also the mass differences and meson mixings could have been argued to be of electromagnetic origin. However, in the quark model the u and d quark mass difference can be fundamentally independent of the electromagnetic interaction, so isospin symmetry breaking may well occur even in the pure strong interaction. At the quark level an obvious reason for isospin symmetry breaking is just this u and d quark mass difference as well as the Coulomb interaction between quarks[II.2,II.3].

Henley and Miller[II.4] have given a convenient classification of the possible components of the NN force according to their isospin behavior. In their system class I forces are charge independent (isoscalar forces). Class II forces are charge symmetric but charge dependent (isotensor forces). Class III forces breaks charge symmetry but do not mix states of different isospin. They depend on $[\tau_3(1) + \tau_3(2)]$ and affect the nn and pp systems but not the np system. Class IV forces affect only the np system and also cause transitions between states of different isospin. Both class III and class IV forces are isovector in nature Since the generalized Pauli principle applies to the NN system, this implies that there is a simultaneous transition between spin singlet and spin triplet states for class IV forces.

Tests of charge symmetry breaking (CSB) in the free NN system are attractive for several reasons. Firstly, the strong interaction amplitudes are well understood. Secondly, the many-body complications that arise in even the simplest nuclei are avoided. For the free np system in particular, the magnitude of electromagnetic (EM) effects is minimized thereby making observable CSB effects easier to interpret. For example, the EM corrections to pp scattering length are at least ten times the size of any CSB effect in $a_{nn} - a_{pp}$. In addition, the np system is the only one sensitive to the class IV forces. Therefore np measurements

test new aspects of meson exchange forces ($\Delta T = 1$ terms), and allow us to probe "indirect" EM effects, e.g. photon exchanges between quarks, or simultaneous photon-meson exchanges between nucleons. They may even provide us with a tool to probe QCD effects and the SU(2) symmetry breaking in the strong interaction arising from the u-d quark mass difference.

## II.2 CSB Effect in the $np \rightarrow d\pi^0$ reaction

Since a deuteron has isospin equal to zero and a pion has isospin equal to one, the reaction can go only in the T = 1 channel. Therefore, the reaction mechanism must be identical to the $pp \rightarrow d\pi^+$ reaction where the identical particles in the incident channel require that the reaction be symmetric about 90° in the center-of-mass system. The ramifications of charge symmetry on the $np \rightarrow d\pi^0$ reaction is clearly evident in figure 4.1.

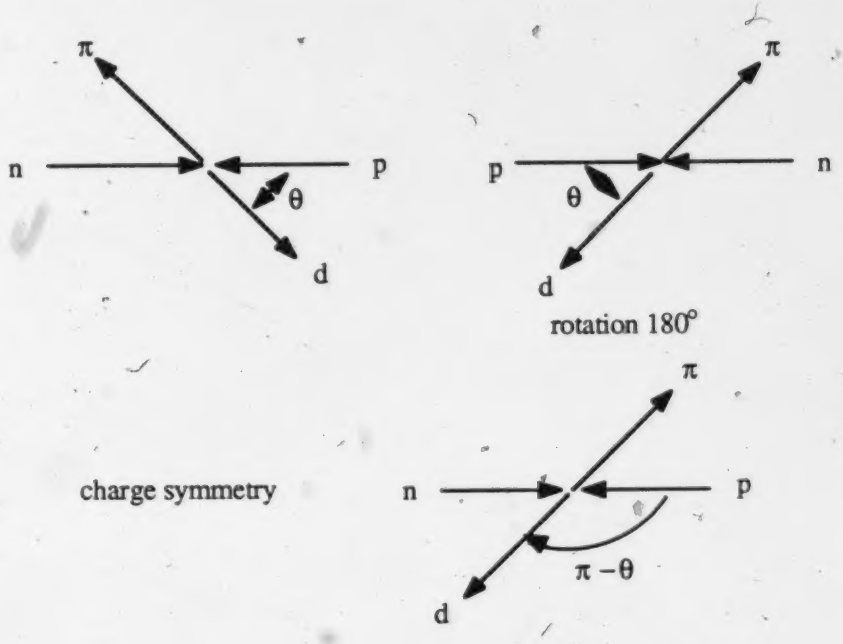


Fig. II.1 Illustration of charge symmetry constraints on $np \rightarrow d\pi^0$ reaction in c.m.s.

If charge symmetry holds, we have

$$\frac{d\sigma}{d\Omega}(\theta) = \frac{d\sigma}{d\Omega}(\pi - \theta) \qquad \text{(II.4)}$$

Therefore, the forward-backward asymmetry in the cm system defined by

$$A_{fb} = \frac{\frac{d\sigma}{d\Omega}(\theta) - \frac{d\sigma}{d\Omega}(\pi - \theta)}{\frac{1}{2}\left[\frac{d\sigma}{d\Omega}(\theta) + \frac{d\sigma}{d\Omega}(\pi - \theta)\right]} \qquad \text{(II.5)}$$

must identically be zero. In the $np \rightarrow d\pi^0$ reaction, the significance of an experimental result is not as heavily dependent on uninteresting coulomb effects. Recent theoretical predictions[II.5] have shown that the asymmetry may be as large as 1%. The energy dependence as predicted at three c.m. angles is shown in Fig.II.2. In these calculations the two dominant CSB mechanisms are found to be (1) the n-p mass difference in one pion exchange and (2) $\pi$-$\eta$ mixing. The best measurement of the $np \rightarrow d\pi^0$ forward-backward asymmetry is the LAMPF experiment by Hollas *et al.*[II.6] at 795 MeV. The angle-averaged value of $A_{fb}$ they obtain is $-(0.3 \pm 1.0)\%$ and is consistent with the prediction of Niskanen *et al.*[II.5] More experimental and theoretical reviews for $np \rightarrow d\pi^0$ one can be found in refs. II.3 and II.7.

For the charge symmetry breaking effect in experiment 466, one more term is added in expression (3.1)

$$\frac{d\sigma}{d\Omega}(\theta) = \frac{1}{4\pi}\left[A_0 + A_1 P_1(\cos\theta) + A_2 P_2(\cos\theta)\right] \qquad \text{(II.6)}$$

and the angle-averaged asymmetry is given by

$$\langle A_{fb}\rangle = \frac{2}{\pi}\int_0^{\pi/2} A_{fb}\, d\theta = \frac{8 A_1}{\pi}\int_0^{\pi/2} \frac{d\sin\theta}{2A_0 + A_2(2 - \sin^2\theta)}. \qquad \text{(II.7)}$$

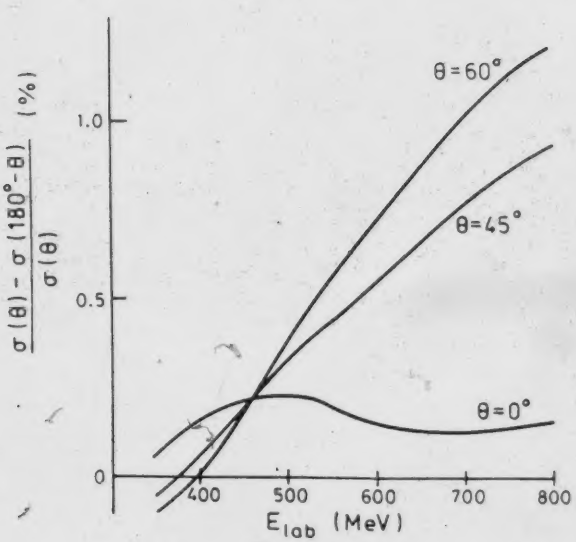


Fig. II.2 The forward-backward asymmetry in $d\sigma/d\Omega$ for $np \rightarrow d\pi^+$ as a percentage of $d\sigma/d\Omega$ at three c.m. angles (0°, 45° and 60°) as a function of neutron laboratory energy (from Ref. II.5)

Using expression (II.6) to analyze the data of E466, we obtain the usual $A_0$ and $A_2$ coefficients, as well as the other coefficient $A_1$. The resulting asymmetries are listed in table II.1 by virtue of Eq. (II.7).

**Table** II.1 The value of the angle-average asymmetry in E466

| Beam Energy | $<A_{fb}>$ |
|---|---|
| 277 MeV | ( - 0.7 ± 7.0 ) % |
| 278 MeV | ( - 1.5 ± 6.0 ) % |

In a word, the $A_{fb}$ agrees with the results of Niskanen *et al.* and Hollas *et al.*, but the statistical precision is not very interesting. Actually, experiment 466 was not supposed to do CSB measurement because of limitation of the statistical uncertainty of the data and the systematic error, for example, the energy width in neutron beam and multiple scattering deuteron underwent in $LH_2$ target, etc.

There is a proposal at TRIUMF to determine $A_{fb}$ at 0° for an energy of 477 MeV with a precision of 0.1%[II.8].

## References


II.1. W. Heisenberg, Zeit. F. Physik **77**, 1 (1932).

II.2. J.A. Niskanen, Proceeding of the Symposium/workshop on Spin and Symmetries, p.205, (TRIUMF,1989).

II.3. A. Gersten *et al.*, Few Body System **3**, 171 (1988).

II.4. E.M. Henley and G.A. Miller, in Mesons in Nuclei, edited by M. Rho and D. Wilkinson, (North Holland, Amsterdam, 1979) Vol. I, p416.

II.5. J.A. Niskanen, M. Sebestyen, and A. W. Thomas, Phys. Rev. C**38**, 838 (1988).

II.6. C.L. Hollas *et al.*, Phys. Rev. C**24**, 1561 (1982).

II.7. L.G. Greeniaus, Nucl. Phys. A**478**, 745 (1988).

II.8. L.G. Greeniaus *et al.*, TRIUMF Experimental Proposal #368.